Characterization of shallow landslides, based on field observations and remote sensing

Developing and testing a field work form at four sites in Western and Eastern Norway

Simon Anfinnsen

Master Thesis in Geosciences
Discipline: Geohazards
Department of Geosciences
Faculty of Mathematics and Natural Sciences

UNIVERSITY OF OSLO

June 2017

Characterization of shallow landslides, based on field observations and remote sensing

Developing and testing a field work form at four sites in Western and Eastern Norway

Simon Anfinnsen

Master Thesis in Geosciences
Discipline: Geohazards
Department of Geosciences
Faculty of Mathematics and Natural Sciences

UNIVERSITY OF OSLO

June 2017

Abstract

Shallow landslides in soils, such as debris flows and debris avalanches, are expected to increase in frequency and intensity in large parts of Norway. The simulation, characterization and statistical analysis of such events require extensive data, and the statistical analysis requires numerous events to do statistics on. A standard field work form is believed to be useful in the collection of such data, and improve the comparative analysis in future studies. The objectives of this thesis are the development and testing of a field work form, and the detailed characterization of four selected landslides.

The field work form is based on literature studies, expert feedback, and field testing done as part of the characterization of each landslide. Three debris flows and one debris avalanche were selected and surveyed using the field work form. Soil samples were collected at all sites and weather data extracted for two sites with known date of occurrence. Furthermore, geophysical methods were used at one site. Runout simulations, using DAN3D, were carried out for three sites, and the collected data was used for setting up the models.

Simulation results agree with the field observations and the field work form is considered to suite its purpose, the most significant uncertainty being velocity estimations, due to the lack of field observations. A terrain model interpolated from GPS data gathered in the field was shown to improve simulation results. The sites were thoroughly characterized, and all triggering conditions seem to be the result of extreme groundwater and runoff conditions. Explanations to what affected the initiation of each landslide are discussed. Surface and subsurface structures favoring water infiltration are common for all the sites. In addition, thin soil cover, weathered bedrock and sliding planes are recurrent factors of importance to the landslide initiation at the four selected sites. The thesis is part of the KLIMA2050 research effort.

VI

Acknowledgements

First and foremost, I would like to thank my two supervisors, Anders Solheim and José Mauricio Cepeda for sharing their time and knowledge. Your guidance and feedback have been crucial and I have learned a lot from the two of you during the past year.

This time has also allowed me to work with, and learn from, a number of competent people, for which I am very grateful. From NGI, Frode Sandersen has provided valuable feedback through the development of the field work form, and Asgeir Olaf Kydland Lysdahl and Helga Anschütz have provided the geophysical expertise and helped me process the data. Many people at UiO have been very helpful, in particular Trond Eiken, in providing equipment, software, datasets, and instructions on their use, and Mufak Said Naoroz who instructed me on how to use the lab equipment. Harald Norem and Arnold Hustad from Statens Vegvesen, and Petter Fornes from NTNU, took part in the field survey and shared some valuable insights. Without the input and expertise of these people much of the work done in this thesis would not have been possible.

Thank you to my fellow students for interesting discussions and much needed distractions, in particular all the students at room 219.

I would also like to thank my parents. My father for great professional input and discussions, and my mother for much needed logistical help. Lastly, I would like to thank my significant other, Lisa, for her love and support, for getting me out to get fresh air when staring too long at the screen and for proofreading my thesis.

Simon Anfinnsen
Oslo, 30.05.2017

Table of contents

X

Appendix 2-7 are available on request. Contact sanfinnsen@gmail.com or follow link:

https://www.dropbox.com/s/gew36qe77ctzb88/Appendices%202-7.pdf?dl=0

1   Introduction

Natural hazards caused 3.3 million fatalities between 1970 and 2010 (The World Bank, 2010), and more than 100 casualties are attributed to landslides in soils in Norway alone since 1900 (Olje- og energidepartementet, 2012). An increase in the number of days with, and magnitude of, extreme precipitation is expected throughout large parts of Norway, and subsequently, precipitation related landslides are expected to increase in frequency (Aaheim et al., 2008). However, due to climatic differences between the east and west of Norway (Sandersen et al., 1996), the change is not expected to affect the country uniformly (Sorteberg and Kvamstø, 2008). With high velocities and destructive energy, debris flows and debris avalanches are particularly challenging landslides, the characterization and parametrization of which are the focus of this thesis.

Glaciations and deglaciations have been potent agents in shaping the terrain and, by that, facilitating for landslides. The majority of the soil cover is comprised of till (Schanche, 2014), and the selective glacial erosion has shaped deep valleys and high reliefs (Olsen et al., 2013). Melting of the ice, and subsequent crustal rebound, is causing the land to rise, areas previously covered by the ocean to emerge and the system to move towards a new state of equilibrium (Lambeck et al., 1991). Thus landslides are currently very active agents in shaping the terrain of Norway, and landslide hazards pose dangers to people, and in particular infrastructure.

This thesis is a contribution to the Centre for Research-based innovation (SFI) Klima 2050. The aim of Klima 2050 is to "reduce the societal risks associated with climate changes and enhanced precipitation and flood water exposure within the built environment " (Klima 2050, 2017). The project, spanning eight years, involves partners from the public and private sector, in addition to research and education institutions, and has a budget of 220 million Norwegian Kroner (NOK).

The objective of this thesis is twofold:

1: Develop a field work form to be used in the investigation of debris flows and debris avalanches, both in this thesis and future similar work on landslide evaluations.

The form should be intuitive and easy to use, while containing sufficient parameters to do runout simulations and back calculations. It should also contain sufficient parameters to do

statistical analysis on debris flows and debris avalanches in Norway, if used on numerous sites. It therefore needs to be applicable on a wide range of sites.

2: Characterize and describe specific debris flows and debris avalanches.

The characterization and description must provide likely conditioning and triggering factors and provide sufficient data for runout simulations. Events with different characteristics and mechanisms involved should be covered.

The characterization and description will also aid in the testing and verification of the field work form, and provide feedback for the iterations following each survey.

In order to achieve the objectives, four sites were selected according to the framework outlined above, and numerous field methods were combined, in accordance with the field work form. These include collection of soil samples, GPS measurements and geophysical methods, in addition to the actual observations from the field. In tandem with this, aerial photographs were analyzed.

The results from these methods will have two purposes:
a: The detailed characterization and description of each site as outlined in objective 2.

b: Provide the input parameters for runout simulations.

The degree of success to achieve a and b will be used as a measure of the degree to which objective 1 has been fulfilled. Runout simulations are included as benchmark, and method, because of its increasing usefulness and precision in predicting runout length, inundated area and destructive force. Thus, runout simulations are often used to estimate the areas at risk, and the required properties of active mitigation measured, elaborated on in section 2.7.

Also, the feedback from landslide experts has been crucial to the development of the field work form, which has evolved in an iterative process.

2 Theory

2.1 Landslides

The general term landslide is used to describe the downslope movement of soil, rock and organic materials under the effect of gravity and also the landform that results from such movement (Highland and Bobrowsky, 2008). The term indicates a sliding motion, which for some landslides is not the correct mechanism of motion. Therefore, Varnes (1974) uses the term slope movement in his classification. In this thesis, the term landslide will be used because of its widespread use, in spite of the lack of precision in the wording itself. The reader should keep this in mind.

Both definitions above include slow processes, such as creep, though some definitions have a velocity requirement as well. In a handbook issued by the Norwegian Public Roads Administration, a slide (*skred*) is defined as "a rapid mass movement of snow, rocks or soil, where the masses often hold abundant water" (Norem et al., 2012).

A variety of attributes have been used in the identification and classification of landslides, including type of movement, type of material, rate of movement, geometry of the area of failure and the resulting deposit, age, causes, degree of disruption of the displaced masses, relation or lack of relation of slide geometry to geologic structure, degree of development, geographic location of type example and state of activity (Varnes, 1974). In 'The Varnes classification of landslide types, an update' (Hungr et al., 2013), type of movement and type of material is the primary criteria used in the classification. This system (Table 1) provides 32 different landslide-types including debris flow and debris avalanche, both being studied in this thesis. It also covers the range of previously mentioned velocities. This classification system will be used throughout the thesis.

Table 1: Landslide terminology basen on material and type of movement. [a] Movement types that usually reach extremely rapid velocities as defined by Cruden and Varnes (1996). (Hungr et al., 2013)

Type of movement	Rock	Soil
Fall	1. *Rock/ice* fall[a]	2. *Boulder/debris/silt* fall[a]
Topple	3. Rock block topple[a]	5. *Gravel/sand/silt* topple[a]
	4. Rock flexural topple	
Slide	6. Rock rotational slide	11. *Clay/silt* rotational slide
	7. Rock planar slide[a]	12. *Clay/silt* planar slide
	8. Rock wedge slide[a]	13. *Gravel/sand/debris* slide[a]
	9. Rock compound slide	14. *Clay/silt* compound slide
	10. Rock irregular slide[a]	
Spread	15. Rock slope spread	16. *Sand/silt* liquefaction spread[a]
		17. Sensitive clay spread[a]
Flow	18. *Rock/ice* avalanche[a]	19. *Sand/silt/debris* dry flow
		20. *Sand/silt/debris* flowslide[a]
		21. Sensitive clay flowslide[a]
		22. Debris flow[a]
		23. Mud flow[a]
		24. Debris flood
		25. Debris avalanche[a]
		26. Earthflow
		27. Peat flow
Slope deformation	28. Mountain slope deformation	30. Soil slope deformation
	29. Rock slope deformation	31. Soil creep
		32. Solifluction

2.2 Debris flow and debris avalanche

As one of the first, the Austrian geologist Josef Stini distinguished between debris flows and torrents. He described how a mountain torrent through increased watercontent and flow velocity incorporates masses that at a certain limit changes it into a viscous mass, consisting of water, soil, sand, gravel, rocks and wood (Stini, 1910).

This early classification introduced elements of viscosity and flow mechanisms, and bears a remarkable resemblance to the definition set by the Norwegian Natural Hazards, Infrastructure, Floods and Landslides (NIFS) project: "A rapid floodlike slide, in water saturated sediments. Occurs along steep river and stream beds, also where there usually is no permanent runoff" (Devoli et al., 2015a). Jakob and Hungr (2005b) emphasize the same factors, though adding that "Plasticity index is less than 5 % in sand and finer fractions".

Similarly to Stini (1910) and Varnes (1974), Jakob and Hungr (2005b) describe debris as sand, gravel, cobbles and boulders with varying proportions of silt and a trace of clay, which might also contain a significant proportion of organic material, such as logs, tree stumps and organic mulch. This will be the general definition of debris, as a material, used throughout this thesis.

Hungr et al. (2013) outlined an update to the Varnes landslide classification, emphasizing the importance of entrainment and surging through the flow path, in their definition of debris flow: "Very rapid surging flow of saturated debris in a steep channel. Strong entrainment of material and water from the flow path". This is the definition used throughout this thesis, and is the equivalent of the Norwegian term *flomskred* (Devoli et al., 2015a).

The emphasis on entrainment and surging are important because, like Stini (1910) correctly observed, the entrainment of material greatly increases the mass. Because of the high level of debris in the flow material and turbulence, periodic damming may occur. This causes individual surges, once dammed material is released, increasing the peak discharge and speed of the individual surges, compared to a steady flow. The additional mass and velocity enhances the destructive forces of the debris flows.

All these definitions emphasize the channelized nature of debris flows. Thus a clear distinction between landslides in the same material types is made, depending on whether the slope movement progresses through a well-defined channel, or an open slope. In Table 1, debris flow is listed in accordance with material and type of motion.

In the case of an open slope, the term debris avalanche is used: "Very rapid to extremely rapid shallow flow of partially or fully saturated debris on a steep slope, without confinement in an established channel. Occurs at all scales" (Hungr et al., 2013). This is equivalent to the Norwegian term *jordskred* (Devoli et al., 2015a).

Debris avalanches typically initiate from a smaller failure in water saturated material, gaining mass as it progresses downslope, loading and mobilizing the masses downslope (Hungr et al., 2013). Geometrically, debris avalanches have much in common with point release loose snow avalanches, in that they develop a triangular shape, accumulating masses and expanding its width greatly.

Also worth noting from Table 1 is gravel/sand/debris slide. It is defined as a sliding of a mass of granular material on a shallow planar surface parallel with the ground (Hungr et al., 2013). While these slides are usually dryer and lack the geometry of debris avalanches and debris flows, they might trigger debris flows or debris avalanches. They might also evolve into either of the two, through increased water content or channelization. Though not being the focus of this thesis, the reader should be aware of debris slides as an actor in initiating debris flows and debris avalanches. The Norwegian term is *jordskred* (Devoli et al., 2015a).

As seen above, the Norwegian terms used do not distinguish between debris avalanches and debris slides.

In summary, debris flows and debris avalanches are both defined by their high flow velocity, high level of water saturation and the material being classified as debris. The main factor separating the two lies in debris flows following a defined channel, while debris avalanches occur in open slopes. The Norwegian terminology for debris flow is *flomskred*, while the debris avalanche equivalent is *jordskred*. These definitions are based on Hungr et al. (2013) and the Norwegian translations are based on Devoli et al. (2015a).

2.3 Impact of debris flows and debris avalanches

A hazard can be defined as the probability that a particular danger (threat) occurs within a given period of time. The risk on the other hand can be seen as a measure of the probability and severity of an adverse effect to life, health property or the environment. This is often quantified as Risk = Hazard * Potential (worth of) loss (International society for soil mechanics and geotechnical engineering, 2004)

Thus, for a hazard to be hazardous, something needs to be at risk (Crozier and Glade, 2005), and the risk can be defined as the intersection between the two (Figure 1).
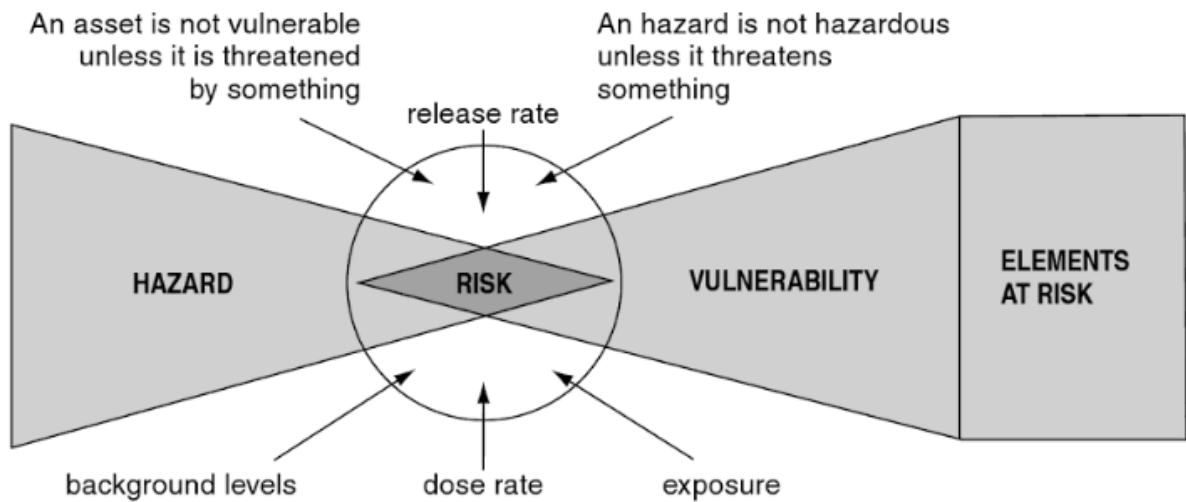
Figure 1: The relationship between hazard, vulnerability and risk (Crozier and Glade, 2005).

Landslides affect both the natural and built environment (Highland and Bobrowsky, 2008). They shape significant areas of the earth's surface through their erosive force and transport large masses with significant destructive potential. They also threaten to impose secondary hazards, as the masses can dam rivers and watercourses (Costa and Schuster, 1988), cause tsunamis (Ward, 2001) and trigger new landslides (Hungr et al., 2013). There is also the risk of cascading disasters (Pescaroli, 2015).

Fast moving landslides, like debris flows and debris avalanches, are among the most destructive types of landslides. They often occur without warning, move too quickly for warnings or measures to be taken, and have a huge damage potential due to material properties and velocity (Highland and Bobrowsky, 2008). People have been known to settle in and around alluvial fans, and debris flows are recognized as one of the most important factors in building alluvial fans (Costa, 1984), introducing vulnerable elements to the hazard. Also, people are dependent on roads and rail crossing such areas for vital supplies, both commonly vulnerable to landslides.

Between 1970 and 2010, natural hazards killed approximately 3.3 million people, mostly in developing countries (The World Bank, 2010). In the United States, landslides alone account for 25-50 fatalities and damages exceeding $2 billion each year (NOAA-USGS Debris Flow Task Force., 2005). The exact costs and fatalities caused by landslides worldwide will depend largely on the reporting. A common source of error is that consequences of landslides

triggered by earthquakes or storms are most often categorized as consequences of the latter two.

In Norway, more than 150 000 people live permanently in areas threatened by flooding and landslides (Olje- og energidepartementet, 2012), and landslides and snow avalanches are the most common forms of natural hazards. Landslides and snow avalanches have killed approximately 3000 people the last 200 years (Slettan and Smits, 2013) and caused 1.4 billion NOK in damages between 1980 and 2010 (Olje- og energidepartementet, 2012). For landslides in soils, more than 100 fatalities have been registered since 1900 (Figure 2) and the frequency of slides is expected to increase (Aaheim et al., 2010).
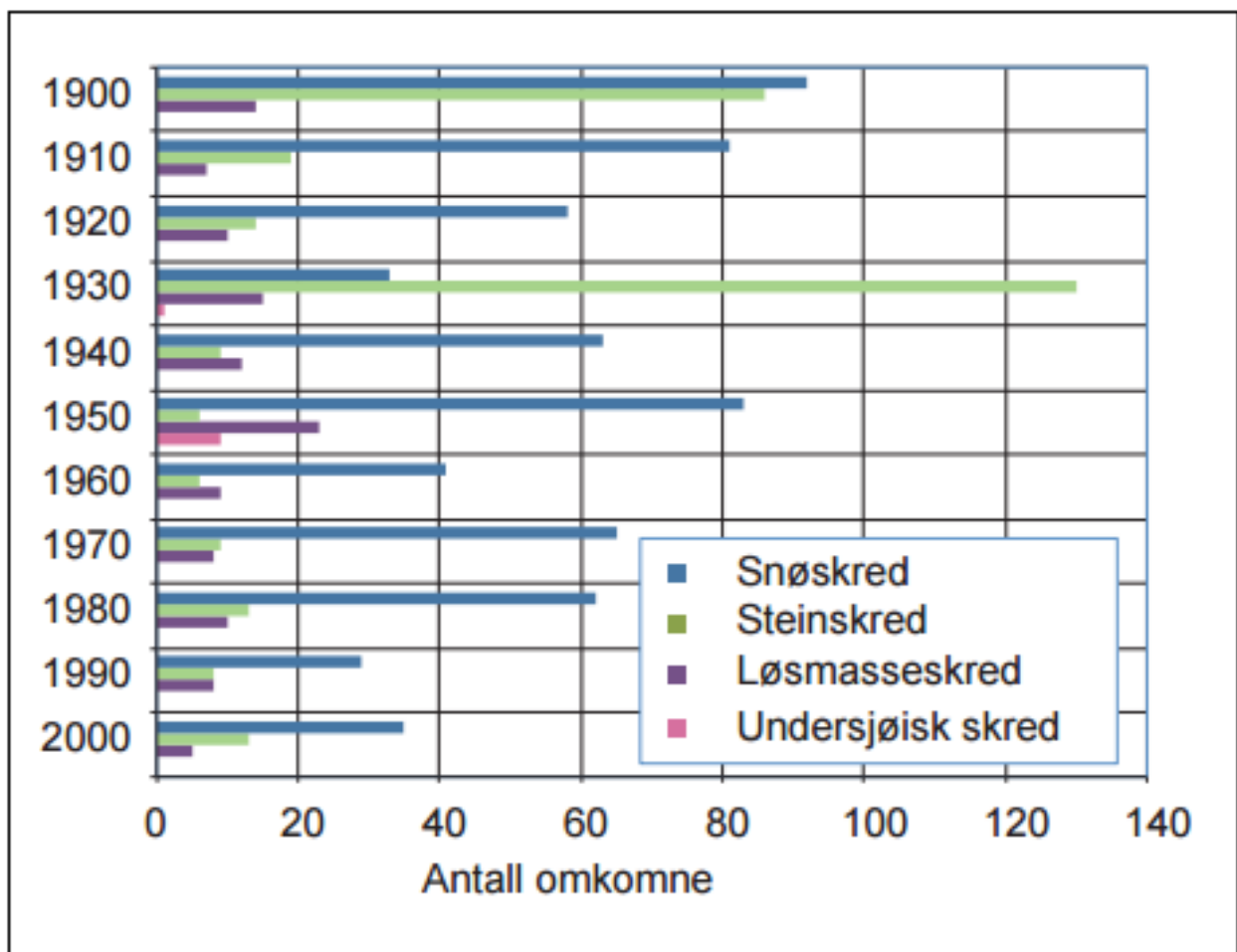
Figure 2: Number of fatalities between 1900 and 2000. Blue, snow avalanches; green, rockfall; purple, landslides in soil; pink, subaqueous slides (Olje- og energidepartementet, 2012).

2.4   Behavior and mechanisms

A debris flow or debris avalanche is typically divided into an initiation zone, or release area, transport zone and depositional area (Jakob and Hungr, 2005a). For the purpose of this thesis, the release area is defined as the area where the mass that experienced the initial slope failure originated. The transport zone is defined as the part of the landslide path/channel immediately below the release area, down to the point where deposition is, and continues to be, larger than erosion, and velocity starts to decrease. The depositional area is defined from this point (the apex) and along the boundary of the area where masses are deposited (Norem et al., 2012).
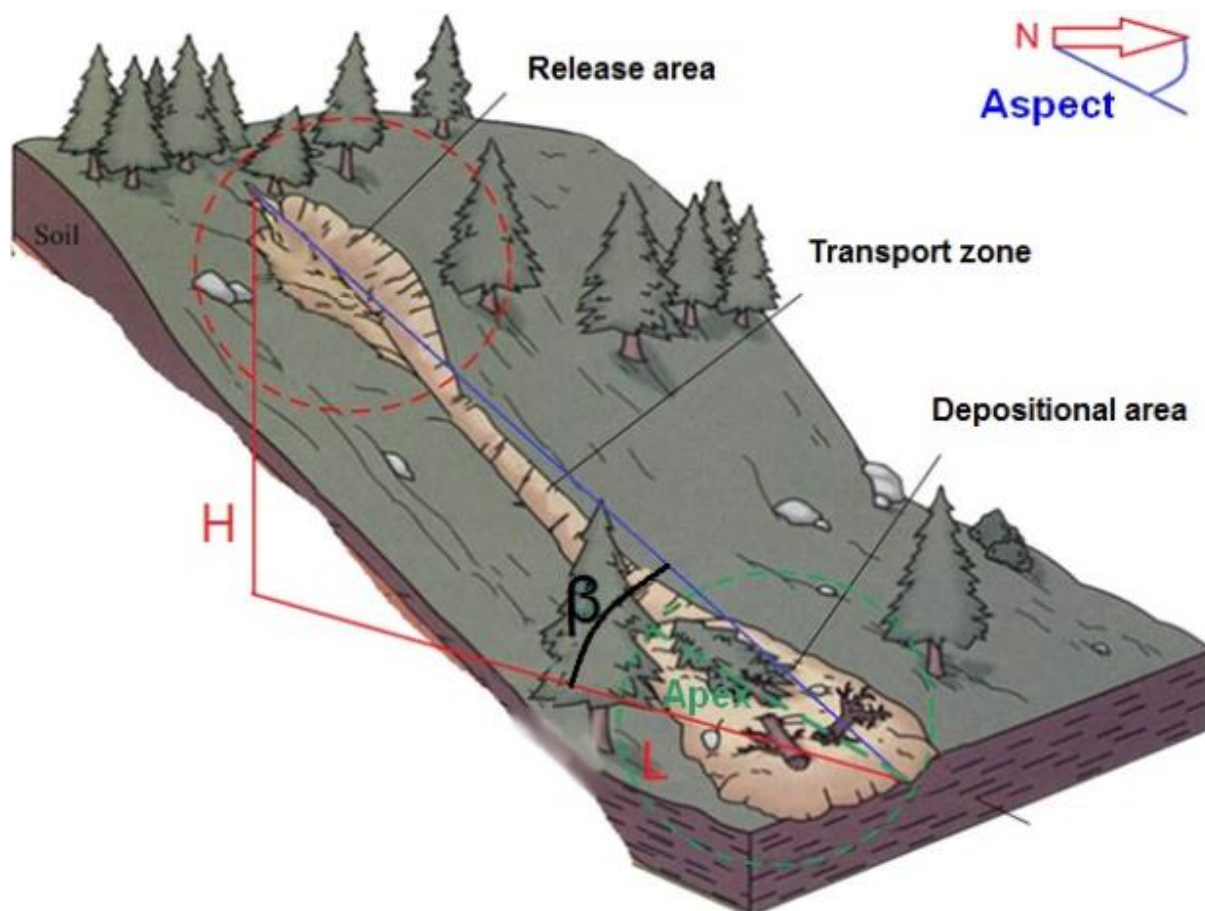
Figure 3: Sketch of a landslide with each of the three zones marked. Modified from Zhang (2015).

The horizontal distance from the release area to the front of the depositional area is called the total runout length (L), and the total elevation difference between each end of L is designated H. A certain amount of the finer material will be washed away given sufficient water and topography. In the field surveys and aerial photography analysis, the depositional area will be defined as the visible depositional lobe and deposits clearly originating from the landslide event. L is measured to this point. A ratio of H/L is often calculated, and a travel angle (β)

(Figure 3) defined as tangent inverse of this ratio. The β-angle, as defined above and used throughout this thesis, should not be confused with the β-angle used in the α-β-modell, frequently used in snow avalanche runout length estimation (Norem, 2011). Defining the front of the depositional area is largely dependent on the purpose of the investigations, and different experts often give different definitions (Jakob, 2005b), illustrating the need for a standardized method.

The most important factors, in addition to topography and channel geometry, in controlling type of motion, velocity and runout length for water related slides are: Size and volume of the slide, erosion along the path, particle size, pore water pressure and roughness and thereby friction of the terrain over/in which the masses flow (Norem et al., 2012). Increased volume normally increases velocity and runout length, while erosion in turn increases the volume. Larger particles normally increase friction, thus limiting velocity and runout length. High pore pressure increases velocity, and roughness in the terrain/channel increases friction and reduces velocity.

With intergranular grains typically constituting 30-70 % of the volume (Iverson, 2005), debris flows behave very differently from both water torrents and slides in dry granular media, and are often described as an intermediate between the two (Hillestad, 2013). The amount of sediments and clasts means that grain to grain interactions will play a much more important part than in a torrent. On the other hand, the high water saturation means that the solid-liquid interactions play a much greater role than in the case of a dry granular media. This makes prediction and modelling of debris flows particularly difficult, because their behavior conform less to established rheologies, and ideally needs to be simulated as a multiphase system. Rheological parameters are therefore often established empirically or through back calculations.

2.4.1 Channelization

As the flowing or sliding mass progresses down its path, debris avalanches will often follow gullies or steep stream channels (Jakob and Hungr, 2005a). They might also build their own channels as they erode the soil and build levees at the lateral boundaries of the flow direction (Costa, 1984). Thus, a debris avalanche, or debris slide, might evolve into a debris flow or display behavior resembling debris flows. By confining the flowing masses laterally, the level of channelization, and channel geometry, greatly affects the pore water pressure as

exemplified by the surging nature of debris flows. This means that the channel characteristics can influence the rheological behavior of the flowing material.

In Norwegian conditions, channelization is mostly natural, though artificial channelization is known to occur. In the Las Colinas landslide of 2001, occurring in the residential area of Santa Tecla, a suburb of San Salvador in El Salvador, buildings on both sides of a street are thought to have channelized the landslide, limiting lateral spreading (Figure 4), thus increasing the runout length considerably (Evans and Bent, 2004).

Figure 4: The Las Colinas landslide. The two main paths of the landslide can be seen on each side of the buildings in the lower center (Evans and Bent, 2004) A and B marks the two different paths.

2.4.2 Surging

Debris flows commonly move in distinct surges (Jakob and Hungr, 2005a, Norem et al., 2012, Costa, 1984, Davies, 1986, Pierson, 1995). The surges usually feature a head and a tail, though they vary a greatly in morphology and mechanism. Often the surge will consist of a front dominated by larger clasts, and if present, boulders, followed by an increasingly fine grained tail of suspended particles (Costa, 1984, Jakob and Hungr, 2005a). The large clasts accumulate at the head primarily by being incorporated in transit and by selective sieving (Iverson, 1997). In selective sieving, the large clasts fail to travel through the small voids opening up between the smaller clasts behind it, thus the flowing mass experiences a longitudinal sorting process, resembling sieving. Coarse grained surge fronts have little pore water pressure, while the finer grained debris behind the front is nearly liquefied by high pore water pressure (Iverson, 1997). The movement is thereby characterized by a coarse front with high friction being pushed forward by the finer core and tail (Norem et al., 2012, Høeg et al., 2014). Where large boulders and clasts are not present the pulse might have a turbulent highly erosive head, followed by laminar flow (Davies, 1986).

The head is usually higher than the tail (Figure 5) and the largest debris flow surge might have a peak discharge more than 1 order of magnitude larger than the largest hydrological flood (Hungr et al., 2013). Surging might also occur when channels are periodically blocked and dammed, releasing once sufficient masses, and thus resulting force, have been built up behind the dam (Costa, 1984). It is suggested however, that such processes are not sufficient to explain the surging in several larger debris flows (Davies, 1986), where turbulent fronts and longitudinal sorting are the preferred explanatory mechanisms.

Due mainly to retrogressive failure or enlargement of the source slide, debris avalanches also surge when not evolving into debris flows (Jakob and Hungr, 2005a). Evidence of surging can be found in the depositional sequence, which gives indications of the mechanisms of motion and behavior of the flowing material.
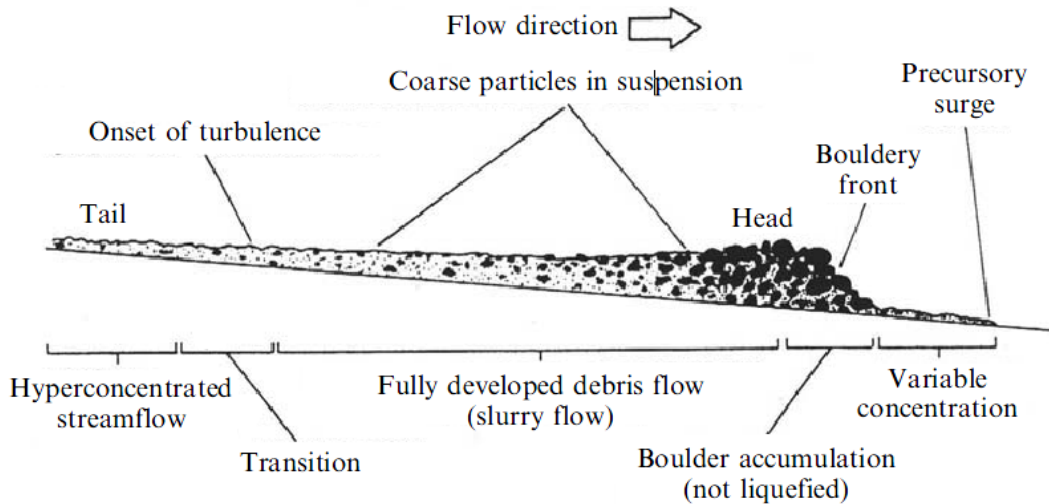
Figure 5: Diagram of a debris flow surge with boulder front (Hungr, 2005).

2.4.3 Entrainment

The bulk of material involved in a debris flow event is usually entrained through the flow path (Hungr et al., 2013). The surging, and consequent increased peak discharge, are likely responsible for much of this erosive power. There are two main mechanisms of material entrainment (Iverson, 2005):

1: Bed destabilization and erosion resulting from drag forces, and to some extent, strength loss due to loading and liquefaction.

2: Material entrainment through the undercutting of channel banks, resulting in their failure and subsequent incorporation into the flowing mass.

The undercutting might in fact itself contribute to the surging of the masses, as materials from the channel banks dam the channel, and are remobilized once sufficient forces are applied. Debris, per the definition given in this thesis, include organic materials such as logs, tree stumps and organic mulch (Jakob and Hungr, 2005b). These are mostly entrained throughout the landslide path due to the abovementioned erosive forces and undercutting of vegetated surfaces.

2.4.4 Deposition

In the depositional area, the velocity of the moving masses is retarded, continuously depositing material until all the masses are deposited. Similarly to the selective sieving of surge fronts, experiments indicate that the initial velocity retardation, where coarse fronts have developed, is driven mainly by the aforementioned coarse grained front. This is due to the negligible pore water pressure and high grain to grain and grain to bed friction of the coarse front, compared to the finer core (Major and Iverson, 1999). Decreased slope angle and reduction or removal of channelization, in addition to natural and artificial impediments to flow, are the main depositional factors (VanDine, 1996). The deposition will normally start at slopes of around 15°-20° (Norem et al., 2012), though material properties and channelization have such a large effect that this will vary significantly. Impediments can be natural in the form of logs, large boulders or previously deposited natural debris dams. Impediments can also be artificial, both unintentionally, such as roads and buildings, or by design, as in mitigation measures like artificial dams and walls.

Normally, both debris flows and debris avalanches will display a coarse to fine depositional sequence, where the coarsest clasts and boulders are deposited first, often as levees, with increasingly finer deposits towards the front (Norem et al., 2012, Schanche, 2014). Well-developed boulder front surges often experience an accumulation of coarse clasts at the front and margins (Pierson, 2004), and have diminishing diameters rearwards (Takahashi, 2007). The inverse grading, and tendency of larger grains to appear at the top, has been fittingly dubbed the 'brazil nut effect' or 'brazil nut problem', in subjects regarding granular physics. It refers to the tendency of the larger nuts to surface in a box of nuts with different sizes (Huerta and Ruiz-Suárez, 2004).

A precise border between the transport zone and depositional area (Figure 3) is often hard to find, as the debris flows, and to some extent debris avalanches, often will have a zone of partial deposition where levees develop, followed by a depositional lobe (VanDine, 1996). Debris flows are recognized as one of the most important agents in building alluvial fans (Costa, 1984). The deposits will settle, and volume decrease as pore water pressure decreases and porosity and permeability decrease in the deposited debris (Iverson, 1997).

Part of the finest fraction will often be transported further by what is designated as hyperconcentrated flow. This term is used to describe flows intermediate between water

floods and debris flows or mudflows (Pierson, 2005). Hyperconcentrated flow can be defined by sediment concentration, bulk rheological properties and the amount and behavior of sand suspended in the flow (Pierson, 2005). This thesis will not focus on these definitions, instead recognizing hyperconcentrated flow as an important agent in transporting fine grained sediments. Defining the boundary of the depositional area is further complicated by this process, and one should be aware that parts of the flowing mass might be transported further, while being spread too far and thin to be recognizable.

2.5 Slope stability

The slope, and the slope stability, is a complicated system evolving through time, gravity being the most important actor. Generally, a landslide occurs when the resistant forces (S) become smaller than the driving force (T) (Sidle and Ochiai, 2006). Thus, whether a slope will fail can be expressed by the fraction of S divided by T. This is called the factor of safety:

$$F_s = \frac{S}{T} \tag{2.1}$$

where the slope fails if $F_s < 1$ (Bell, 1998).

Figure 6 illustrates how this problem is set up by Sidle and Ochiaci (2006) as an infinite slope:
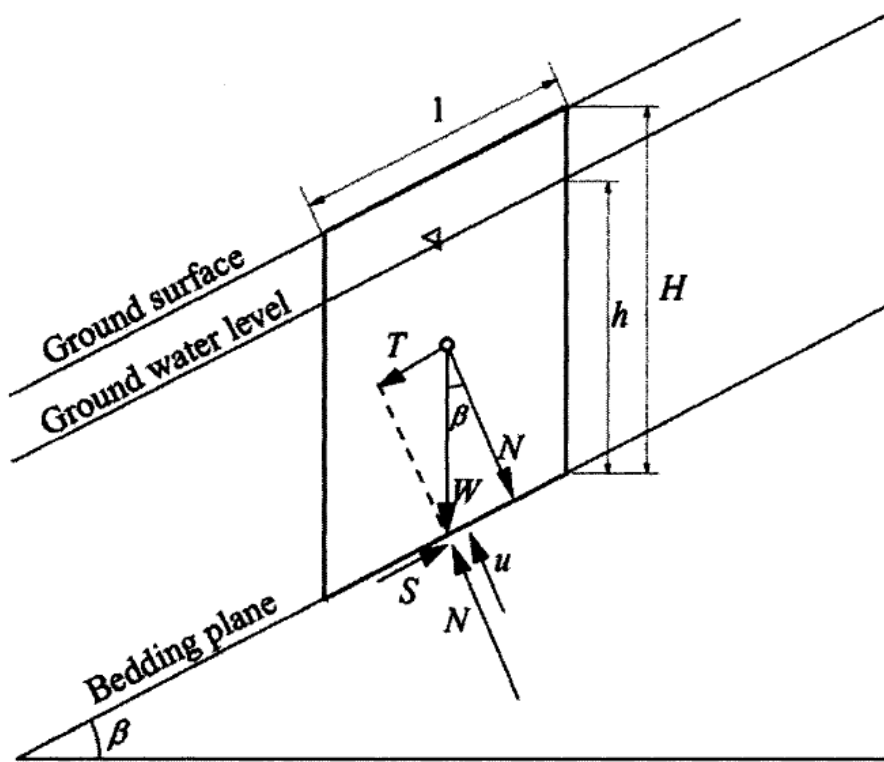
Figure 6: The slope and the parameters governing S and T (Sidle and Ochiai, 2006).

As mentioned above, S and T are the resisting and driving forces, respectively, N the normal force to T, and W the weight acting on the slice. β is the angle between the slope and the horizontal plane and l the length of the slice of a portion of the sliding mass sliding over the surface. The pore water pressure acting on the bottom of the slice is u when the vertical water depth is h. S can be expressed as:

$$S = c + (W \cos \beta - u) \tan \Phi \qquad (2.2)$$

Where c is the cohesion factor of the soil and Φ is the internal friction angle. For seepage parallel to the sliding surface, u is given by:

$$u = \gamma_w \, h \, cos^2\beta \qquad (2.3)$$

Where γ_w is the unit weight of water and h the vertical height of the water table above the sliding surface. H is the vertical height of the soil layer. The weight (W) acting on the slice is:

$$W = [\gamma_t (H - h) + \gamma_{sat} h] \cos \beta \qquad (2.4)$$

16

Where γ_t is the unit soft weight of the soil above the water table and γ_{sat} the saturated unit weight of the soil. H is the vertical depth of the soil, and h the ground water level.

T is related to W by:

$$T = W \sin \beta \qquad (2.5)$$

The factor of safety is defined by dividing S by T:

$$F_s = \frac{c}{W \sin\beta} + \frac{\tan \Phi}{\tan \beta} - \frac{u \tan \Phi}{W \sin \beta} \qquad (2.6)$$

Equations and explanations are taken from (Sidle and Ochiai, 2006).

Unit weight and internal friction angle is input parameters used in the runout simulations (section 3.4).

2.6 Slope failure

For a slope to fail, there are three main prerequisites (Norem et al., 2012, Aaheim et al., 2008):

1: The terrain geometry.
2: A sufficiently thick layer of soil with limited stability.
3: A triggering mechanism.

2.6.1 Terrain geometry

Generally, the release area of debris flows and debris avalanches will be located in steep slopes (Glade, 2005, Costa, 1984), usually between 20° and 45° (Jakob and Hungr, 2005a). This is because flatter slopes might not provide sufficient force to initiate a failure, while steeper slopes rarely accumulate a sufficiently thick cover of sediments. Slope gradients alone are however not sufficient in determining areas prone to slope movement. Slower processes such as soil creep have been recorded on slopes as gentle as a couple of degrees (Finlayson, 1981) and soil creep is often a precursor of landslides in soil (Sidle and Ochiai, 2006).

The shape of the slope is also of great importance as it affects whether water is concentrated in an area, or dispersed. Three basic hydrogeomorphic slope units are identified by Sidle and Ochiachi (2006): Divergent, planar and convergent.
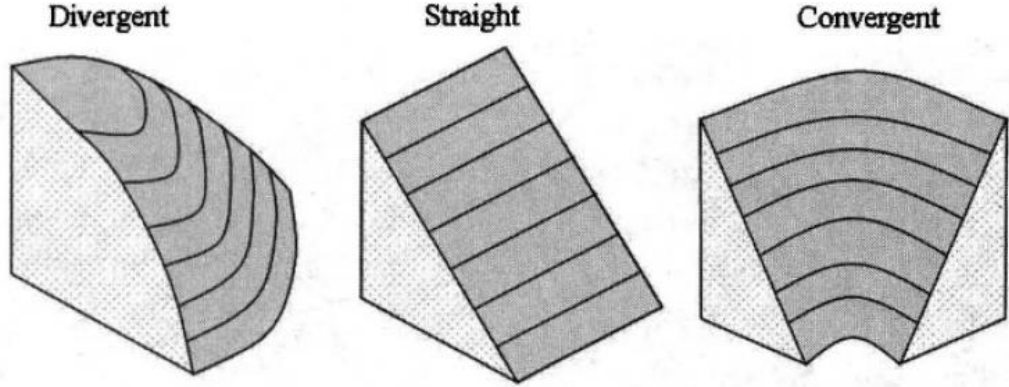
Figure 7: The three hydrogeomorphic slope units identified by Sidle and Ochiachi (2006).

The geometries (Figure 7) indicate that the divergent slope, with its convex shape, will disperse the water over a greater area, thus lowering the soil saturation, surface erosion and pore water pressure. Convergent slopes, with their concave geometry, will have an opposite effect, accumulating water in a smaller volume, thus increasing surface erosion, saturation and pore water pressure. The straight geometry is an intermediate between the two, ideally displaying the same erosion, saturation and pore water pressure at each point perpendicular to the flow direction. Generally, all else being equal, divergent slopes are regarded as the most stable, convergent as the least stable, and straight an intermediate (Sidle and Ochiai, 2006).

2.6.2 Soil layer, bedrock and stability

The majority of debris flows and debris avalanches are initiated on steep slopes underlain by relatively strong rocks with a thin mantle of soil (Savage, 2005). In Norway, landslides in soil are primarily initiated in till, which makes up the majority of the soil cover above the marine limit (Schanche, 2014). Looking at equation 2.6, it is evident that for landslides in shallow soils, such as debris avalanches, cohesion and pore water pressure are important, and become less important as W increases with depth (equation 2.4). Thus, the factor of safety decreases with greater depth, approaching:

$$F_s = \frac{\tan \Phi}{\tan \beta}, \qquad when \qquad \frac{\tan \Phi}{\tan \beta} \gg \frac{c}{W \sin\beta} - \frac{u \tan \Phi}{W \sin \beta}$$

This means that for deeper soils, internal friction angle and slope inclination are most important. Equation 2.6 shows how increased cohesion increases the factor of safety, while increase in pore water pressure has the opposite effect (Figure 8).
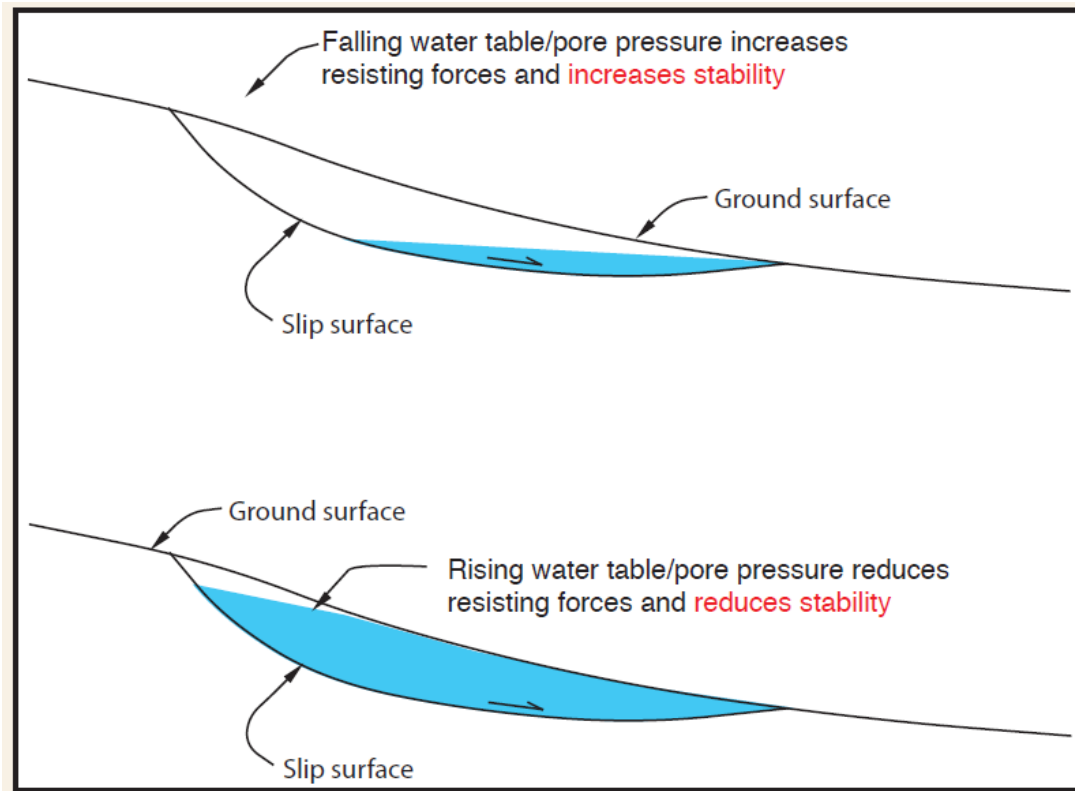
Figure 8: Schematic of the effects of falling and rising ground water table on slope stability (Highland and Bobrowsky, 2008).

The true cohesion of soils stems from the bonding of fine grained particles, while the parameter c used in the equation above is a combination of the true soil cohesion and other physical properties. These include soil moisture, grain size distribution and relative density. Generally, cohesion decreases with increased soil moisture, though very small amounts of water might create negative pore water pressure, or suction, when bridges between otherwise uncohesive grains form (de Blasio, 2011). This is the effect seen when building sand castles. Typically, cohesion increases with clay content. Internal friction angle represents the degree of interlocking of individual grains or aggregates and is influenced by the shape, size and packing of the particles (Sidle and Ochiai, 2006). As angular particles have greater interlocking capabilities, they generally contribute to a larger internal friction angle.

The slope units identified in section 2.6.1 (Figure 7), and their consistent relation between geometry and water processes, on the surface and in the sub surface, assume a similar consistency between bedrock and surface topography. This will not always be the case. The bedrock might lead water into the overlying masses purely by its geometry, or fractures in the rock, and form a plane for the masses to slide over. Also, weak and weathered rock might itself constitute a weak layer. Generally, bedrock with layers parallel to the potential plane of failure is regarded as a destabilizing factor as they provide less mechanical support to the overlying masses and facilitates water flow (Chatwin et al., 1994). Determining the depth to, and topography of, the bedrock often requires the use of geophysical methods, some of which have been used in this thesis (sections 3.3, 5.2 and 6.2).

Weathering modifies the mechanical, chemical and hydrological characteristics of the soil and rock, thus modifying slope stability, and contributes in producing weak layers and fractures. Mechanical weathering is exemplified below by freeze thaw processes. Chemical weathering includes dissolution, where air and water moving through rocks and minerals dissolve and mobilize chemical constituents (Sidle and Ochiai, 2006). The most important biological weathering agent is vegetation and root growth.

Freeze and thaw processes contribute to the destabilization of slopes and cause rockfall (Highland and Bobrowsky, 2008). As water expands when frozen, the freezing causes cracks to expand, and while the ice temporarily "glues" the rock together, the subsequent thawing leaves the rock weaker. This expansion of cracks is an example of mechanical weathering. For soils, the thawing removes a similar glue-effect (Schanche, 2014), leaving the soil with higher pore water pressure. In permafrost regions, water from snowmelt and precipitation concentrates in the active layer, limited vertically by the permanently frozen layer, causing large pore water pressure (Geertsema et al., 2014). This boundary, or the lithological boundary depending on which is closer to the surface, acts as a sliding surface (Leibman et al., 2014), similarly to weak soils underlain by bedrock. On Svalbard, seasonal freezing and thawing of the active layer are in some instances thought to have stabilized slopes otherwise thought to fail from large water input (Humlum, 2017).

2.6.3 Vegetation

One of the primary factors related to debris flows is vegetation (Gao et al., 2014). The vegetation primarily affects slope stability through modification of soil moisture and response

to air humidity, and through reinforcing and anchoring of the soil (Ziemer, 1981). Increased soil moisture decreases the soil cohesion and increases pore water pressure and weight, while consumption of water or interception of precipitation reduces soil moisture (Breien et al., 2013). The root anchoring effect increases the total cohesion of the soil and might, depending on the root system and bedrock, anchor the soil layer to the bedrock or underlying strong layers. The roots might also contribute in fracturing the rock itself, and vegetation can as such be an agent of biological weathering. Other effects include wind speed attenuation and surface flow retardation, both reducing erosion and mass movement (Barker, 1986). During strong winds, vegetation might also have a destabilizing effect, acting as a sail mobilizing and destabilizing underlying masses (Breien et al., 2013). Depletion of soil moisture may also accentuate desiccation cracking in the soil, increasing infiltration capacity (Bell, 1998).

The removal of vegetation will, given time, remove its stabilizing effects (Norem et al., 2012). In addition, wildfires can cause intensive drying of the soil, changing the infiltration characteristics of the soil and lead to decrease of infiltration, thus increasing overland flow (Cannon and Gartner, 2005).

For some shallow landslides, the evapotranspiration itself might not be too important as factors controlling snow accumulation and melt dominate the spring hydrologic performance of individual slopes (Megahan, 1983).

2.6.4   Triggering mechanisms

Debris flows originate when poorly sorted rock and soil debris are mobilized from hillslopes and channels by the addition of moisture (Costa, 1984). They often occur simultaneously with floods (Hungr et al., 2013) and are often numerous in a region (Jakob and Hungr, 2005a). The addition of moisture cannot be stressed enough, as debris flows and debris avalanches by definition have a high degree of water saturation (Hungr et al., 2013). The primary sources of moisture are rainfall, snowmelt and in some instances glacial outburst floods (GLOF) (Costa, 1984). Water influx might also stem from water escaping fractured bedrock.

As explained in sections 2.6.2 and 2.6.3, increased soil moisture content can increase pore water pressure and decrease cohesion, both lowering the factor of safety of the slope. In this respect, the influx of water can act as a conditioning factor, decreasing the stability of the slope, while other processes trigger the failure itself. The effects of decreased cohesion and

increased pore water pressure might also be the triggering process. This often happens when high pore water pressure builds in and along the boundary between layers of different permeability, such as soils overlaying bedrock or soils of other hydrological characteristics. In Norwegian circumstances, tills weathered by freeze thaw processes, overlying more consolidated and less permeable tills, frequently display such behavior, where a sliding plane forms along the boundary(Figure 9) (Bargel et al., 2011).
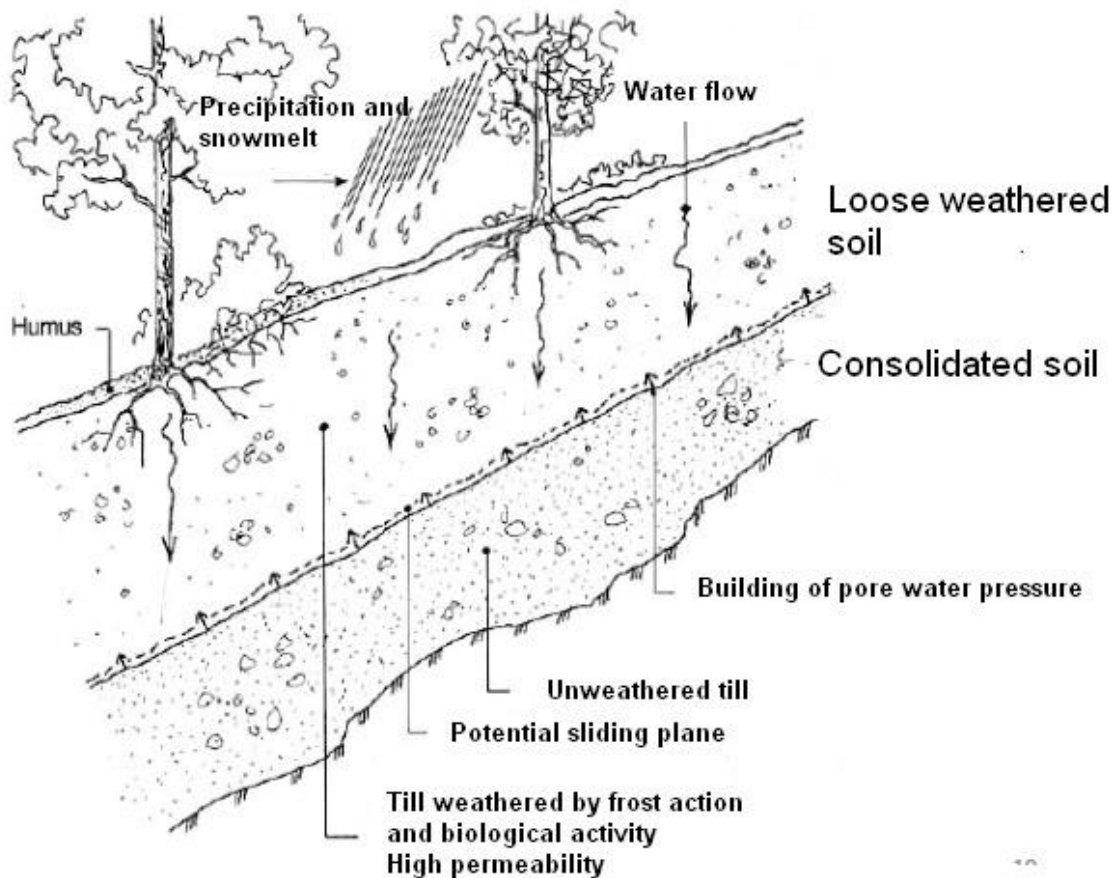
Figure 9: Forming of a sliding plane along the boundary between layers of different permeability. Modified from Bargel et al. (2011).

For rainfall to trigger landslides, the combination of a certain intensity and duration (Wieczorek and Glade, 2005) or extreme values for either (Jaedicke et al., 2008) are required. Several empirical models that calculate a threshold, above which landslides frequently occur, exist, exemplified by the findings of Guzzetti et al. (2008) (Figure 10).

22
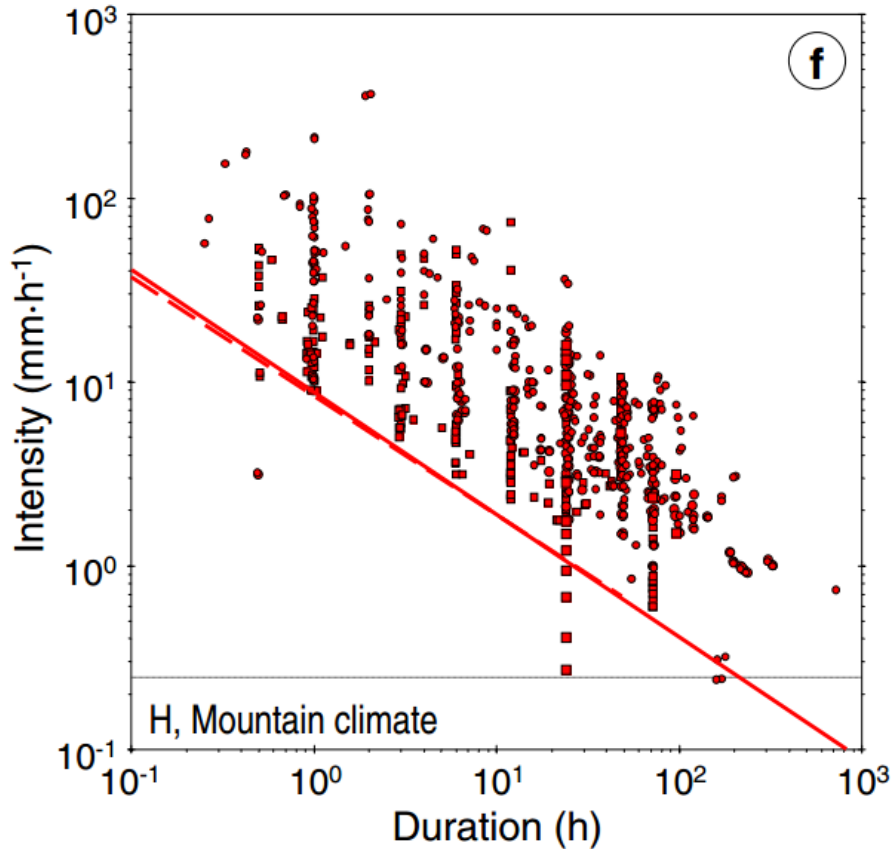
Figure 10: Intensity duration plot. The red line marks the threshold over which landslides frequently occur, and the dots and squares are registered shallow failures and debris flows respectively. The data is from a mountain climate (Guzzetti et al., 2008).

Sandersen et al. (1996) found, when investigating a series of debris flows in Norway, that the critical water supply for slope failure, as percentage of mean annual precipitation, could be expressed by

$$P = 1{,}2 * D^{0{,}6} \tag{2.7}$$

where D is the duration (in hours) of the precipitation event. For D = 6 h, 12 h and 24 h this returns P = 3.5 %, 5.3 % and 8.0 % respectively. Equation 2.7 is used in sections 5.4 and 6.3, when analyzing climate data for Norangsdalen 2 and Kvam. The equation is however based on only 30 events, and local variations mean that it should be viewed primarily as a rule of thumb for the purpose of this thesis. The threshold turned out to be too high for issuing warnings (Meyer et al., 2012).

Other ways water can trigger or condition the slope to fail include increasing the slope gradient, by erosion at the toe of the slope, and increase loading, as the voids in the soil are filled with water.

As debris flows often are associated with floods, the flow of water might itself entrain enough material to develop into a debris flow (Norem et al., 2012), a process known in sedimentologic literature as bulking (NOAA-USGS Debris Flow Task Force., 2005). As seen in section 2.2, this mechanism was described by Stini (1910), and is the most common cause of debris flows in Norway (Norem et al., 2012).

Debris flows and debris avalanches are also frequently triggered by landslides and rockfalls (Highland and Bobrowsky, 2008). Debris avalanches often originate from debris slides (Hungr et al., 2013), and debris avalanches often develop into debris flows (Costa, 1984). Earthquakes and volcanoes, although not common in Norway, also trigger landslides (Highland, 2004). The aforementioned Las Colinas landslide was triggered by a 7.6 Mw earthquake (Evans and Bent, 2004).

2.6.5 Anthropogenic factors

Looking at the prerequisites for slope failure, change in slope geometry and soil properties will affect the slope stability. As with water erosion at the toe of the slope, excavation at the toe will increase the overall slope above the excavation site, and decrease the resisting forces (Guadagno and Revellino, 2005). Road cuts in slopes have this effect, and might also act as a water flow inhibitor (Breien et al., 2013, Fergus et al., 2011), causing larger pore water pressure, or surface erosion (Guadagno and Revellino, 2005). In Norway, modification of the natural drainage pattern is the most frequent anthropogenic cause of shallow landslides in soils (Schanche, 2014), often in the form of logging roads (Fergus et al., 2011).

Increased loading will increase the driving forces (equation 2.6). Filling of material at the head of slopes will increase loading (Figure 11) and slope inclination, and similarly buildings will also increase the loading.
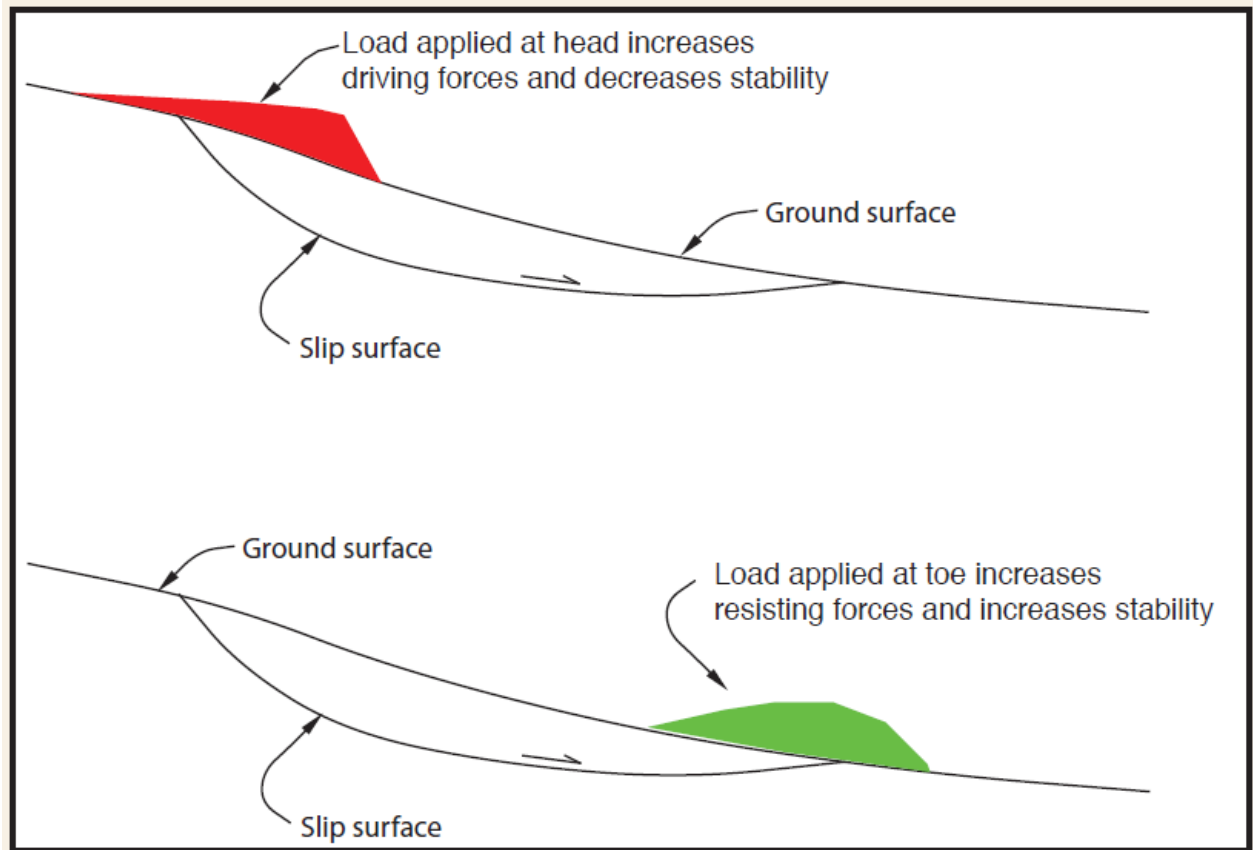
Figure 11: Consequence of loads applied at head and toe of a slope (Highland and Bobrowsky, 2008).

Logging and land clearing will also severely affect slope stability (Highland and Bobrowsky, 2008), and debris flows and debris avalanches are known to occur in conjunction with these actions (Breien et al., 2013).

2.7 Rheology

One of the challenges when estimating characteristics and modeling a landslide event, is the selection of a rheology, constituting the equations governing the material behavior. The two-parameter Voellmy rheology has been found to reproduce debris flow and debris avalanche behavior well (Revellino et al., 2004, Scheidl et al., 2013, Bertolo and Wieczorek, 2005, Lee and Chen, 2003), and will be used in the simulation in this thesis (section 3.4).

In the Voellmy rheology, flow resistance is calculated by:

$$\tau = \gamma H \left(\cos \alpha + \frac{a_c}{g} \right) (1 - r_u) \tan \varphi + \gamma \frac{v^2}{\xi} \tag{2.8}$$

Where τ is the basal flow resistance, γ the bulk unit weight, H the flow depth, α channel slope, a_c the centrifugal acceleration, g the gravity acceleration, r_u the pore-pressure coefficient, φ the dynamical basal friction angle, v the velocity and ξ a turbulence coefficient. The bulk basal friction is often expressed as

$$\mu = (1 - r_u) \tan \varphi \tag{2.9}$$

and r_u can be expressed as

$$r_u = \frac{\gamma_w}{\gamma} \tag{2.10}$$

Where γ_w is the unit weight of water (9.81 kN/m^3) (Dahl et al., 2013). The turbulence coefficient is an empirical coefficient intended to account for all velocity dependent resistance, additional to the effects of path curvature and momentum transfer during entrainment (McDougall, 2006). This thesis will not go into further detail on all the parameters involved or how the equation is solved, though it should be noted that the two parameters being calibrated when back calculating using Voellmy rheology are the bulk basal friction (μ) and the turbulence coefficient (ξ). Selected values and results are found in section 5.3.

2.8 Mitigation measures

In regards to mitigation measures, there is a distinction between active and passive measures (Huebl and Fiebiger, 2005). Passive methods involve no direct engineering as no modification of the event itself is attempted, instead reducing the risk by removing the elements at risk. Active measures require engineering, as modification or removal of the event is attempted (VanDine, 1996).

2.8.1 Passive mitigation measures

Passive mitigation measures can be subdivided into preventive measures and event response (Huebl and Fiebiger, 2005). The preventive measures typically involve land use planning, information and education and rules of conduct. In Norway, land use planning and building specification is regulated through the Planning and Building Act (*Plan- og bygningsloven*) and its *Byggteknisk forskrift* (TEK10) (Schanche, 2014, Direktoratet for byggkvalitet, 2016). The regulation relates building classes to consequence of hazard, designating a minimum return period for each class (Table 2).

Table 2: Safety class related to impact with minimum return period to the right (Direktoratet for byggkvalitet, 2016).

Landslide/avalanche safety class	Impact	Greatest nominal annual probability
S1	slight	1/100
S2	moderate	1/1000
S3	severe	1/5000

Class S1 includes buildings for which landslides will have small consequences such as garages and storage facilities. Landslides striking class S2 buildings will have moderate consequences and include work related buildings normally not housing more than 25 people. Landslides striking class S3 buildings will have severe consequences, and includes residences of more than 10 people, larger work related buildings (housing more than 25 people) and schools, kindergartens, medical facilities and emergency services (Direktoratet for byggkvalitet, 2016).

Education and information are typically handled in schools and courses, and by media and government or municipality.

Rules of conduct will naturally vary between countries, though in Norway *allemannsretten* (public right of access) places few limits upon where and when one can travel, except for special purpose areas and special circumstances (Miljødirektoratet, 2016).

Event response include early warning and evacuation, providing assistance and information (Huebl and Fiebiger, 2005). Effective warning is particularly important, and highly dependent on early warning systems and hazard mapping. Forecasting based on intensity duration curves (Figure 10) have showed some promise in this regard (Guzzetti et al., 2008). In Norway, the web service www.varsom.no (2017) provides warning levels (Table 3) from the Norwegian Early Warning System (EWS) ranging from green (1) to red (4) based on weather data/forecasts, hydrological simulations, estimated thresholds, other web-tools and expert judgement. Devoli et al. (2015b) found that the system provided 93 % correct warning messages during 2013. The warning levels on the time of the landslides at Årset and Kvam are reported in section 5.4.

Table 3: The warning levels in the Norwegian EWS and the expected outcome of each level (Calvello et al., 2017).

Warning level	Classification criteria
4 (Red)	> 14 landslide (per 10-15.000 km2) Hazard signs: Several road blockings due to landslides or flooding
3 (Orange)	6-10 landslides (per 10-15.000 km2) Hazard signs: Several road blockings due to landslides or flooding
2 (Yellow)	1-4 landslides (per 10-15.000 km2) Hazard signs: flooding/erosion in streams
1 (Green)	No landslides 1-2 landslide caused by local rain showers 1 small debris slide if in area with no signs of elevated warning level Man-made events (from e.g. leakage, deposition, construction work or explosion)

2.8.2 Active mitigation measures

Active mitigation measures will attempt to modify the event, either by preventing the event from happening, or by diverting or stopping it, limiting the frequency and magnitude of events (Huebl and Fiebiger, 2005). Modification of slope inclination is again possible, by removing material from the head of the slope and filling at the toe (Figure 11). Retaining walls and piles are often used at the toe of slopes to stabilize it (Highland and Bobrowsky, 2008).

Planting vegetation will, given time, give the stabilizing effects listed in section (2.6.3) (Huebl and Fiebiger, 2005). Improved drainage can reduce pore water pressure and erosion, thus increasing stability. Surface drainage is the simplest drainage measure, and is intended to reduce erosion and infiltration. Subsurface drainage can be done using drainage pipes or trenches and ditches (Highland and Bobrowsky, 2008).

Measures along the expected path include limiting susceptibility to erosion, building of dams, locally decreasing inclination, and the construction of levees to stop the masses from spreading laterally, or lead it away from vulnerable areas (Takahashi, 2007). Similar structures will often be built in the depositional area, leading the masses away, under or over vulnerable objects, or slowing the flow of masses (Norem et al., 2012).

2.9 Climate change and consequences

It is anticipated that climate change will cause increased precipitation in most of Norway (Sorteberg and Kvamstø, 2008). Glacial retreat and deterioration of permafrost are known to have been the cause of slope destabilization (Wieczorek and Glade, 2005), and are expected to be of increasing importance. Change in occurrence of fires might also affect the occurrence of debris flows and debris avalanches.

The Research Council of Norway (RCN)-funded GeoExtreme project (Aaheim et al., 2008) found, based on the Intergovernmental Panel on Climate Change (IPCC) scenario (SRES A2) of a global temperature increase of 2.5 °C to 3.5 °C by year 2100, that:

1: Number of days with extreme precipitation will probably increase. 70 % increase expected for all seasons, except summer. Margin of error means that lowest probable value is 15 % and highest 120 %.

2: The precipitation during extreme events will increase 10 % (±10 %) for all seasons.

Based on the findings of the project, the change in frequency of landslides in soil was estimated (Figure 12).
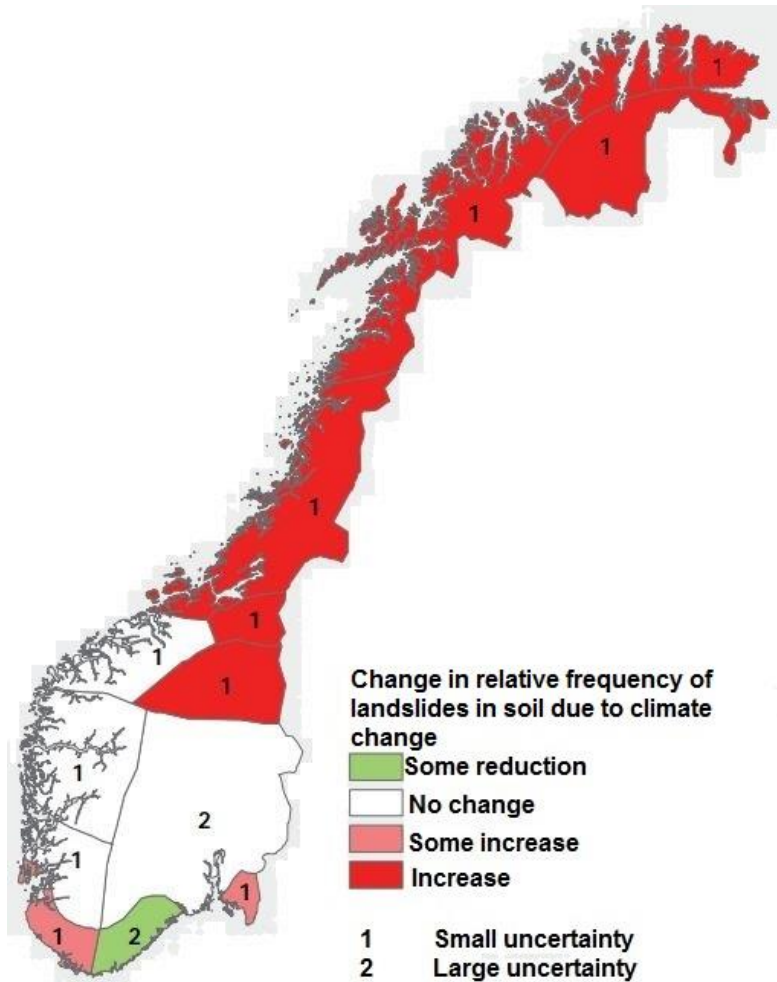
Figure 12: Change in frequency of landslides in soil due to climate change divided across regions in Norway. Based on Aaheim et al. (2008).

For most parts of Norway, frequency of landslides in soils was expected to increase or remain similar to present frequencies. A more recent report (Hanssen-Bauer et al., 2015) by Norwegian Centre for Climate Services (NCCS) upholds these findings.

3 Methods

3.1 Field work

The field work can roughly be divided into three phases:

1: Planning
2: Reconnaissance/exploratory surveying
3: In-depth survey

The planning started early 2016, with a meeting between Klima 2050 partners aimed at selecting criteria for the selection of case study areas for the project as a whole. During April and May of 2016, the valley Norangsdalen in Western Norway was selected as one study area for this thesis, mainly because of the number of events and different types of landslides. The valley was described as a "debris flow laboratory", due to the many types and large number of debris flows in the area. The study was expanded to include side valleys to road E 39 (Figure 13) between Ørsta and Festøya when it was confirmed that local expert Arnold Hustad from Norwegian Public Roads Administration (Statens Vegvesen) would join the surveying party. During later stages of the planning, the area of Kvam in Gudbrandsdalen was also selected for surveying, and the specific slide being surveyed in Kvam (Figure 14) was chosen after a meeting with Klima 2050 partners from SINTEF and Norwegian University of Science and Technology (NTNU) on September 26. Kvam was selected because of the high number of slides in 2011 and 2013, and the different climate compared to the formerly selected sites.

On June 27. the exploratory survey was conducted during favourable weather conditions, with little to no precipitation and a temperature of about 15 °C. Driving through the previously designated areas, particularly interesting slides were more thoroughly investigated and the web service www.Skrednett.no (2016) was used to locate previous events not visible from the road. Based on this, three of the sites observed during the day were chosen for the in-depth survey.
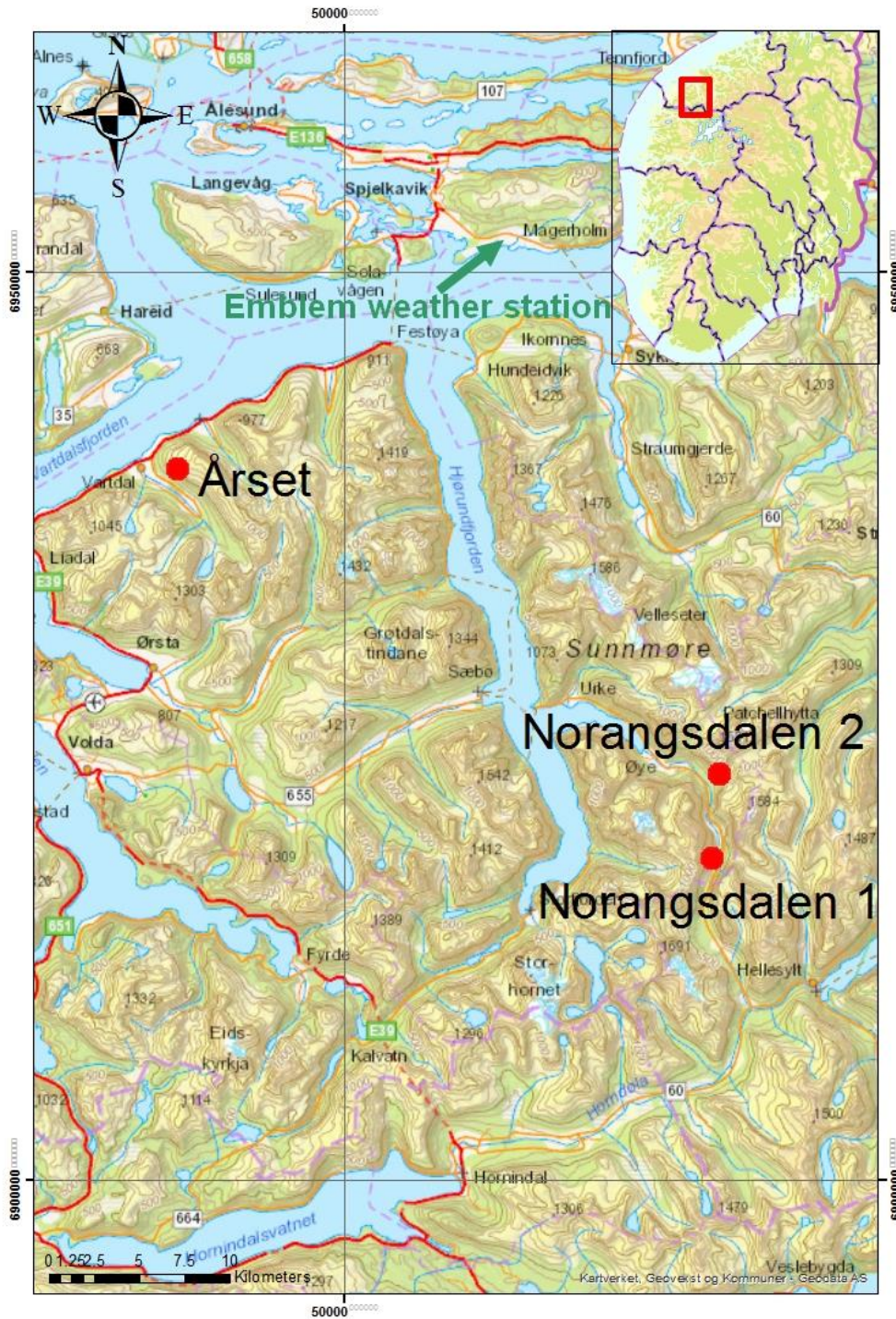
Figure 13: The selected sites in Western Norway. The weather station registering hourly precipitation used in section 5.4.1 is marked at the top. Modified from Kartverket (2017).

The three sites selected in Western Norway (Figure 13) were also revisited the two next days, and soil samples were collected. Notes, measurements and pictures were taken, and are presented in the results section. In addition, new visits to the sites were done between October

13. and 17. During this time there was no precipitation, and temperatures were between 6 °C and – 4 °C. On October 17. geophysical methods were applied at the Kvam site.
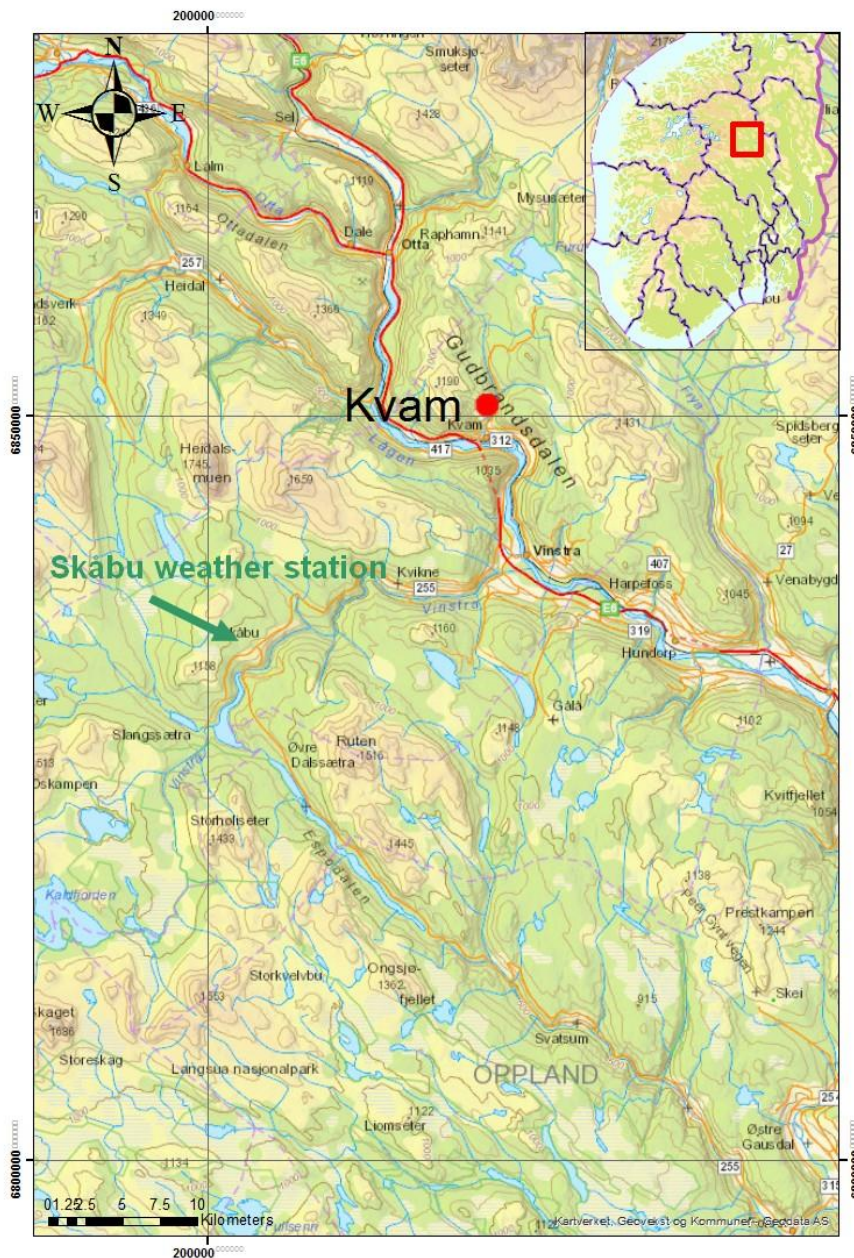
Figure 14: Overview of the Kvam site. On the left side the weather station registering hourly precipitation, used in section 5.4.2 is marked. Modified from Kartverket (2017).

A differential GPS was used to record geometric parameters as accurate as possible. The GPS uses both satellite and the GSM (mobile phone) network in order to achieve an accuracy of 10 cm. Profiles were measured along and perpendicular to the landslide channels, and measurements along the borders of the release and depositional areas were made, where

possible. The GPS data were uploaded into the Geographic Information System (GIS) ArcMap, by Esri (2017) for use in measurements and calculations, and Surfer, by Golden Software LLC (2017) for visualization and interpolation (section 3.4). Initial and final volume was calculated constructing polygons in ArcMap, assigning average source depth and deposit height for each polygon. All georeferenced data are in the WGS 1984 UTM zone 33N format.

3.1.1 Soil sampling

During the field excursions, a total of 16 soil samples were taken from the four sites, the contents of which can be divided into a bagged soil sample containing soils and gravel up to 16 mm, and pictures of the sample and larger clasts. The latter were separated and photographed vertically above the samples with a meter stick as scale (Figure 15). This approach was selected so that the grain size analysis would also give information about the content of larger clasts. It would otherwise be impractical to sample in the field (due mainly to carrying capacity) and analyze in the lab (due to equipment and time limitations).

Figure 15: The sample, separated into coarse and finer fraction, with meter stick as scale.

While the grain shape of the sample is not the subject of detailed analysis, the shape of the grains have been roughly estimated and compared relative to other samples (section 5.1), using the classification scheme by Nichols (2009) (Figure 16).
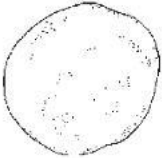
	Well rounded	Rounded	Subrounded	Subangular	Angular	Very angular
Low sphericity						
High sphericity						

Figure 16: Chart comparing roundness and sphericity of grains (Nichols, 2009).

3.1.2 The field work form

In the time leading up to the surveys, a draft field work form was developed. The form was intended to be comprehensible and easy to use while still containing sufficient parameters to perform runout simulations. Initially, the form was compiled using parameters found in literature to be important factors controlling or indicating landslide behavior, mentioned in the theory section. Testing and improving the field work form has been a central part of the field work, and the form has been used since June 2016. Several iterations have been tested, and expert feedback has been important during development. The form is presented in Appendix 1.

3.2 Grain size analysis

Grain size analysis was performed on a total of 16 samples from the four locations. The results of each analysis are listed in the results section, and the photographs of the samples, and sample sites, are found in Appendix 5. The International Organization for Standardization

(ISO) (2002) classification (Table 4) is used to divide the size ranges between clay, silt, sand and gravel in the grain size analysis in section 5.1.

Three methods were combined for the grain size analysis: Picture analysis in order to determine the coarsest fraction, sieving to determine the medium to small fractions (16 mm-0.063 mm and 16 mm-2 mm) and Coulter test to determine the smallest fractions (<0.063 and <2 mm). The reason for the change in minimum mesh size is explained in section 3.2.1. Sieving and coulter tests were done in the lab at the Department of Geosciences at the University of Oslo. The methods combine a measure of percentage of weight, through sieving, percentage of volume, in the Coulter data, and number of nodes in the picture analysis, to identify the distribution of grains ranging from clay to cobble (Figure 19).

Table 4: An overview of the different grain sizes (International Organization for Standardization, 2002).

Soil fractions	Sub-fractions	Symbols	Particle sizes mm
Very coarse soil	Large boulder	LBo	> 630
	Boulder	Bo	> 200 to 630
	Cobble	Co	> 63 to 200
Coarse soil	Gravel	Gr	> 2,0 to 63
	Coarse gravel	CGr	> 20 to 63
	Medium gravel	MGr	> 6,3 to 20
	Fine gravel	FGr	> 2,0 to 6,3
	Sand	Sa	> 0,063 to 2,0
	Coarse sand	CSa	> 0,63 to 2,0
	Medium sand	MSa	> 0,2 to 0,63
	Fine sand	FSa	> 0,063 to 0,2
Fine soil	Silt	Si	> 0,002 to 0,063
	Coarse silt	CSi	> 0,02 to 0,063
	Medium silt	MSi	> 0,006 3 to 0,02
	Fine silt	FSi	> 0,002 to 0,006 3
	Clay	Cl	⩽ 0,002
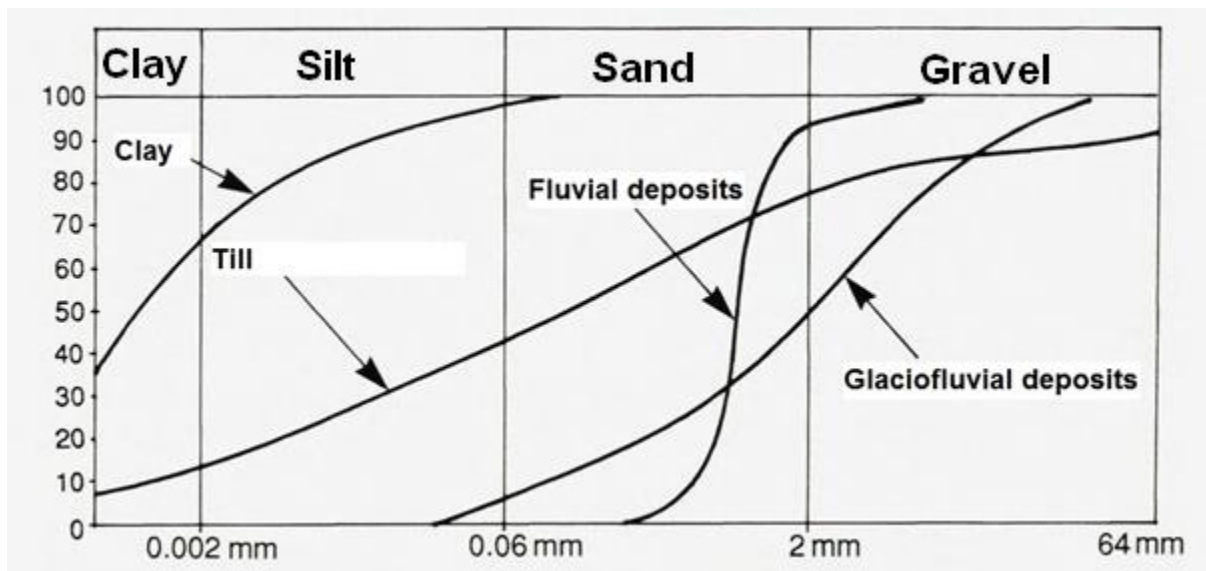
Figure 17: Some typical grain size distribution plots, modified from Neeb (1992).

3.2.1 Sieving

In sieving, the weight of grains within each size interval is measured by pouring the sample through a stack of sieves, under shaking from a vibrating table, with increasingly smaller mesh size down through the stack. The weight of grains left in each sieve is plotted cumulatively, providing a plot from 0 to 100 % where at 100 %, all grains are smaller than the corresponding grain size.

For the dry sieving, representative subsamples of each sample were extracted. This was done by thoroughly mixing the sample in the field sample bag. The sample was then poured into a flat bottomed pan, where it was further mixed to ensure an as homogenous distribution as possible. The sample in the pan was then split into equal quadrants, one of which was extracted into a cup, where it was left to dry at 110 °C for 24 hours and then weighed.

The samples were then washed to avoid aggregates of grains, which would skew the results towards larger grain sizes. In this process, the sample cup was filled with water, and the

contents mixed. The sample cup was then put in a water bath with an ultrasound emitter, in order to dissolve the grains from each other. The contents were then poured through a sieve, the sample continuously exposed to water, until the water escaping the sieve was transparent, indicating that all grains below the mask size had been washed through. The water containing the finer particles was put in another cup. The cup containing the water and fine grains and the cup containing the coarse sample were then set to dry at 110 °C for 24 hours.

Initially (samples 1 to 3) during this step, a 0.063 mm sieve was used. This demanded a large amount of water that had to be stored and dried, for which the equipment is not dimensioned. For this reason, a sieve mask size of 2 mm was selected for samples 4 to 16 during the washing process, leaving all grains < 2 mm to be measured in the Coulter test.

Figure 18: The sieves clamped down in the vibrator.

When dry, the coarse samples were weighed. Two different stacks of sieves were used. Samples 1 to 3 used a complete stack from 16 mm to 0.063 mm in accordance with the Wentworth scale. Samples 4 to 16 had a lower minimum mask size of 2 mm, as the finer particles had already been washed out. The stacks were put in a vibrator (Figure 18), clamped down, and left for 15 minutes. At that point, each individual sieve was shaken by hand until no more grains fell through. The sieves were then weighed. The bottom bowl was also weighed, and the fines smaller than 0.063 mm and 2 mm respectively, were transferred into the corresponding cup of the fines of that sample.

For further details on the sieving process, see the handbook "Laboratorieundersøkelser" (Statens Vegvesen, 2014).

3.2.2 Coulter test

This analysis was done using an LS 13 320 laser diffraction particle size analyzer, from Beckman Coulter Inc. The instrument measures the patterns of scattered (laser) light produced when particles of different sizes, suspended in water, are exposed to beams of (laser) light (Beckman Coulter inc, 2011). The total volume of the sample, and the volume and diameter of the particles are measured, and a cumulative distribution of the particle sizes is produced. The particle diameter is estimated with an assumption of sphericity (Beckman Coulter inc., 2011).

The cups containing the finer fraction of the samples were thoroughly mixed, and a smaller representative sample extracted into a second cup. A small amount of the sample, ranging from 0.2 g to 2 g depending on the grain size of the sample, was extracted into a beaker, diluted with a solution of 5 % calgon (natriumpyrophosphate) and left for five minutes in the ultrasonic bath. The latter two steps were both done in order to disaggregate grains from each other. The sample was then poured into the main chamber of the Coulter device, and if necessary more was added until an obscuration of 8-12 % was achieved. This procedure was done twice for each sample, and the results were compared. If there were irregularities between the results, new tests were done. The device was cleaned and background noise checked between each run. When needed, about every 4-6 runs, the instrument was recalibrated.

For further details on the LS 13 320 and methods of use, see the manual Laser Diffraction Particle Analyzer (Beckman Coulter inc., 2011) and Standard Operating Procedure for: LS 13 320 Laser Diffraction Particle Size Analyzer Operation (Missouri State University, 2008).

3.2.3   Image analysis

In order to achieve a higher level of accuracy, the freeware image analysis package Fiji (Johannes et al., 2012) for ImageJ (Caroline et al., 2012) was used. For each sample, the meter stick visible in each image (Figure 15) was used to calibrate a pixel per cm scale. This was necessary because the camera height above the sample and resolution varied. Once scale was established, the total area of the soil and larger clasts could be estimated by drawing polygons.

The diameter of the larger grains were estimated assuming the rock/gravel was resting with its shortest length axis vertical. Thus, the intermediate axis of the rock was assumed to be perpendicular to the longest visible axis, both being parallel to the horizontal plane, and its value recorded as the diameter.

The image analysis is assumed to be the least accurate of the three methods used. The reader should keep this in mind when reviewing the grain size distribution in section 5.1.

3.2.4   Data conversion and plotting

The three techniques return somewhat different parameters, and in order to plot them together they needed to be converted accordingly. The Coulter counter returns a value for the percentage of the sample's volume having a diameter smaller than values ranging from 0,002 mm to 2 mm. Sieving returns the weight of samples larger than their respective mask sizes. In this instance, the sieving results are recorded using the same intervals, > 16 mm is listed as < 32 mm, and both the Coulter and sieving results are multiplied with the fraction of mass of fines and coarser material to the total mass of the unwashed sample. Thus, cumulative grain size distributions sums up at 100 %, by weight, when these two datasets are added together.

The image analysis data, in contrast, does not include any mass data, and is instead plotted as number of nodes below the sizes of 32 mm, 64 mm and 128 mm. The fraction of the soil samples to the larger clasts have been estimated using their respective areas calculated during

the image analysis, and are weighed accordingly (number of nodes times fraction of larger clasts to the total area) in the final plot. Thus, the three methods sum up to 100 % (Figure 19).
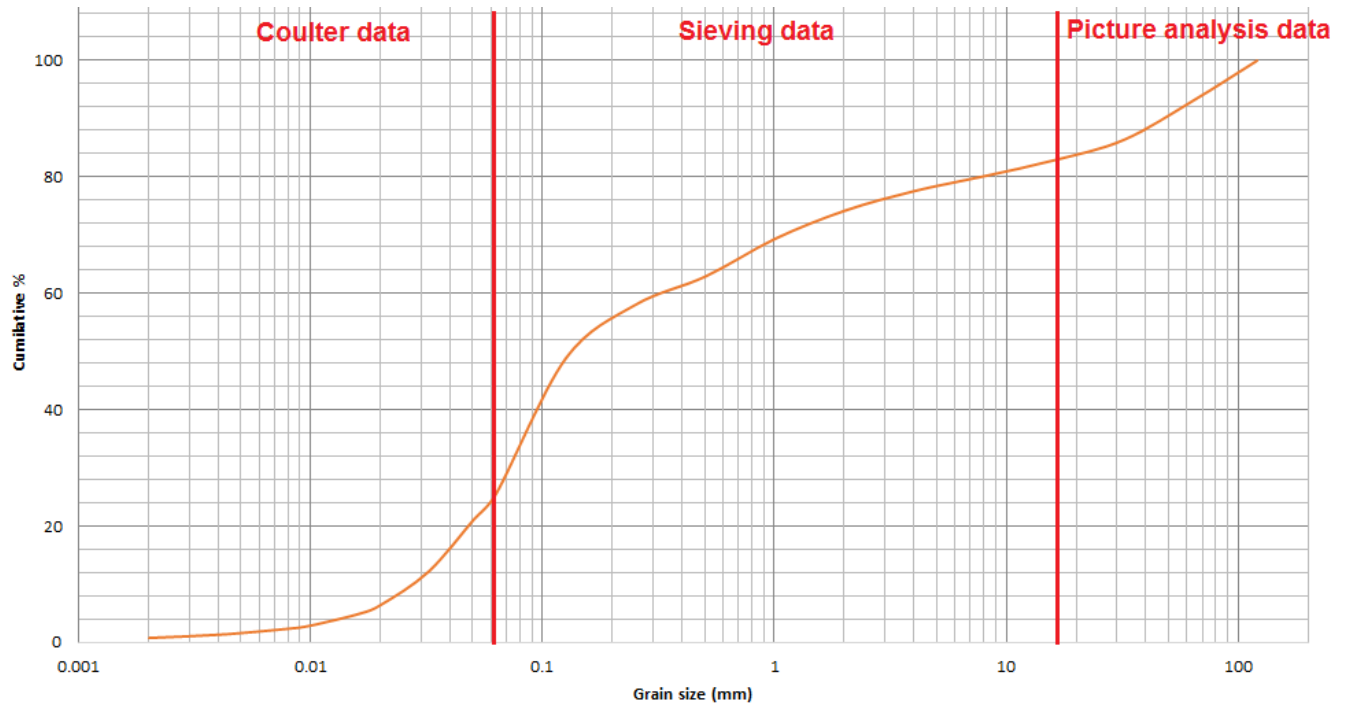
Figure 19: Example of the grain size distribution and the method used to gather data on the different ranges of grain sizes. This example assumes a lower sieve size of 0.063 mm.

3.3   Geophysical methods

During the field work at Kvam on October 17., two geophysical methods were used; Ground Penetrating Radar (GPR) and Electric Resistivity Tomography (ERT). During the ERT acquisition, Induced Polarization (IP) measurements were also carried out. The profiles surveyed were preplanned earlier the same month on the basis of feedback from Klima 2050 partners from SINTEF and NTNU, and are all connected to the landslide path being studied the previous field day and a neighboring landslide. The survey was done together with Asgeir Olaf Kydland Lysdahl and Helga Anschütz from the Geosurveys department at NGI.

3.3.1 Ground penetrating radar (GPR) data acquisition and processing

3.3.1.1   Theory

GPR uses electromagnetic (EM) wave pulses (listed as traces in the radargrams) in the micro-wave to radio-wave spectrum (typically ~1 MHz to 1000 MHz) to record backscattered waves in the form of reflections and diffractions, though forward transmission methods are also possible (Daniels, 2004). The wave velocity can be expressed as:

$$V_m = \frac{c}{\left[\left(\frac{\varepsilon_r \mu_r}{2}\right)\left[\left(1 + P^2\right) + 1\right]\right]^{1/2}}$$ (3.1)

where c is the speed of light in vacuum, ε_r is the relative dielectric constant, μ_r is the relative magnetic permeability and P is the loss factor. The loss factor increases with conductivity, and decreases with increased dielectric constant and frequency. In low loss and non-magnetic materials, the formula is simplified to (Reynolds, 2011):

$$V_m = \frac{c}{\sqrt{\varepsilon_r}}$$ (3.2)

The wave velocity is important because the depth to reflectors are calculated based on the two-way travel time (TWT) used by the wave to travel from the transmitter (Tx), down to the interface and back up to the receiver (Rx).

Also important is the relationship between penetration depth, frequency and resolution. The frequency is related to the wavelength by:

$$\lambda = \frac{v}{f}$$ (3.3)

where λ is the wavelength, v the wave velocity in the medium and f the frequency. As a rule of thumb, the resolution (smallest object registered) is ~ $\frac{\lambda}{2}$. The penetration depth, however,

decreases with increased frequency (Reynolds, 2011). This means that there will always be a tradeoff between penetration depth and vertical resolution.

In order to acquire the wave velocity in the subsurface, an acquisition method known as common mid-point (CMP), where Tx and Rx are moved with increased distance relative to a fixed point, is used. This method is relatively time consuming, and requires a system with two movable antennas. During reflection profiling, where the distance between Tx and Rx is constant, a common method of estimating wave velocity in the medium is to use the diffraction hyperbola displayed in the radargram, created when an object is hit by waves from multiple directions as the antennas are moved. This requires an object in the subsurface, acting as a point reflector.
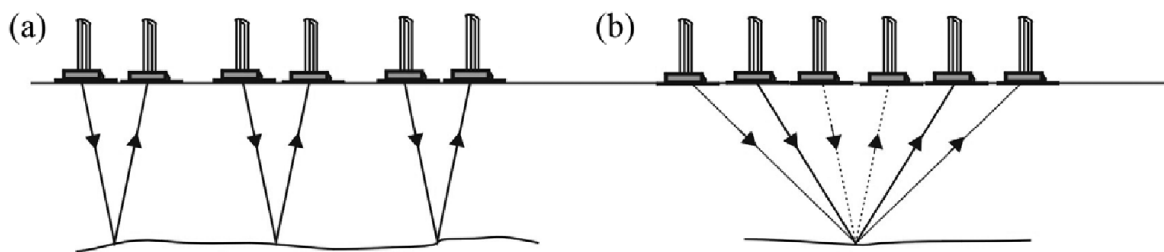
Figure 20: a) Reflection profiling b) Common midpoint method (Daniels, 2004)

High conductivity materials such as salt water and wet clays cause large energy loss, and thus signal attenuation, and are generally regarded as negative for GPR acquisition. Conductivity is the inverse of resistivity, measured in ERT.

Table 5: Relative dielectric constant, radiowave velocity and conductivity for a range of geological and manmade materials. [1] Strongly dependent upon snow density, [2] Strongly temperature dependent below -5 C° (Reynolds, 2011).

Material	ε_r	V (mm/ns)	Conductivity (mS/m)
Air	1	300	0
Water (fresh)	81	33	0.5
Water (sea)	81-88	33	3000
Polar snow[1]	1.4-3	194-252	~0.05
Polar ice[2]	3-3.15	168-172	≤0.06-0.08
Temperate ice	3.2	167	5×10^{-8}
Pure ice	3.2	167	5×10^{-8}
Freshwater lake ice	4	150	$1-10^{-6}$
Sea ice	2.5-8	78-157	10-100
Permafrost	2-8	106-212	0.1-10
Active layer permafrost	25	60	
Gravel	5	134	10
Sand and gravel (unsaturated)	3.5-6.5	118-160	0.007-0.06
Sand and gravel (saturated)	15.5-17.5	72-76	0.7-9
Coastal sand (dry)	5-10	95-134	0.01-10
Sand (dry)	3-6	122-173	$10^{-4}-1$
Sand (coastal, dry)	5-10	95-134	0.01-1
Sand (wet)	10-32	53-95	0.1-10
Sand (golf course)	10-25	60-95	10
Silt (unsaturated)	2.5-5	134-190	1-100
Silt (saturated)	22-30	55-64	≤100
Clay (dry)	2-5	134-212	2-100
Clay (wet)	8-40	47-106	20-1000
Till (unsaturated)	7-21	65-113	2.5-10
Till (saturated)	24-34	51-61	2-5
Moraine	7-14	80-113	$10^{-5}-10^{-7}$
Marsh	12	86	
Peat (freshwater)	57-80	33-40	≤40
Agricultural land	15	77	
Pastoral land	13	83	
Soil (fine-grained)	41-49	43-47	40
Average 'soil'	16	75	5
Granite	5-8	106-120	$10^{-3}-10^{-5}$
Limestone (dry)	4-8	100-113	
Limestone (wet)	6-15	77-122	10-100
Dolomite	6.8-8	106-115	
Basalt (wet)	8	106	

3.3.1.2   GPR profiling

Two different radar antennas were used during the surveys. One 50 MHz unshielded rough-terrain antenna (RTA) produced by MALÅ Geosciences AB, provided by the Department of Geosciences at the University of Oslo, and a shielded 200 MHz SIR 4000 box antenna produced by Geophysical Survey Systems Inc. (GSSI) provided by NGI. Because both devices have a fixed antenna spacing, and CMP acquisition would not be practical given the terrain in the study area and the time available, reflection profiling was the method used. Altogether 16 profiles were surveyed with the 50 MHz antenna, seven of which were discarded due to bad readings, and two profiles were surveyed with the 200 MHz antenna, one of which was discarded for the same reason. Difficult terrain and vegetation limited the use of the 200 MHz antenna to the field above the release areas, thus the larger number of surveys for the 50 MHz antenna. GPR profiling using the 50 MHz antenna is the only geophysical method used directly on the landslide paths. While the 200 MHz antenna utilizes an attached wheel to measure the distance along the profile of each individual trace, the 50 MHz antenna relies on the attached GPS, with an accuracy of 5-6 m, to record the profile along which the survey was done. Thus it should be noted that the 50 MHz antenna triggers a trace every second, while the 200 MHz antenna triggers a trace every 5 cm.

All GPR data processing was done using Reflexw by Sandmeier Geophysical Research (Sandmeier, 2017), provided by the Department of Geosciences. Processing steps were done to improve the signal/noise ratio, correct topography and antenna height and remove noise, including background removal, start time correction, removal of low frequency part (dewow), averaging of horizontal and vertical features (average xy), band-pass filtering and gain. Since reflection profiling does not by itself provide velocity for the waves in the subsurface, this has been estimated to 0.13 m/ns with the help of diffraction hyperbolas, where visible. Terrain corrections were done using GPS data. As the 200 MHz device has no integrated GPS, the data from the 50 MHz acquisition along the same profile were used.

3.3.2 Electric Resistivity Tomography (ERT) and Induced Polarization (IP) data acquisition and inversion

3.3.2.1 Theory

Electrical resistivity methods use the relationship between a current (I), the potential drop (V) and the resistance (R), established in Ohm's law:

$$V = R * I \tag{3.4}$$

Resistance is calculated when a current is induced into a body of mass, resulting in a potential drop (Reynolds, 2011). This is done by deploying a number of electrodes into the ground with a fixed spacing, all connected to a battery pack and control unit, inducing the current. R is, in turn, dependent on the geometry of the body through which the current is induced, so to get any useful data on the actual materials in the subsurface, the resistivity (ρ) of that material needs to be calculated. In a cube, the relationship between the geometry of the cube, R and ρ is:

$$\rho = \frac{VA}{IL} \tag{3.5}$$

where A is the area of the cross section of the cube and L the length of the end faces (see Figure 21).
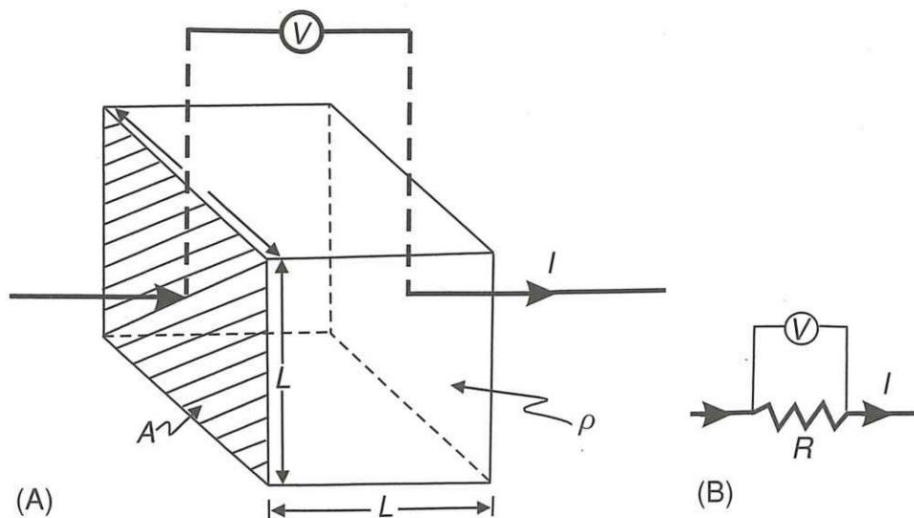
Figure 21: Schematic figure of the body through which the currents are transmitted (Reynolds, 2011).

46

In practice, the calculation of resistivity is done through inversion software that models the geometry and resistivity that would produce the apparent resistivity (ρ_a) recorded in the field. This is an iterative process that aims at producing the model resembling the observations the best.

Table 6: Resistivities of rocks and clay (Henderson and Henderson, 2009).

Material	Resistivity range (Ωm)
Clays	$1-100$
Shales	$0.4-2 \times 10^3$
Limestone	$1.3 \times 10^3 - 8.4 \times 10^6$
Sandstone	$1-6.4 \times 10^8$
Quartzite	$10-2 \times 10^8$
Slate	$2 \times 10^{-4} - 2 \times 10^7$
Marble	$100-2.5 \times 10^8$
Schist	$20-10^4$
Gneiss	$2 \times 10^3 - 3 \times 10^6$
Hornfels	$8 \times 10^3 - 6 \times 10^7$
Basalt	$10-1.3 \times 10^7$
Andesite	$100-4.5 \times 10^4$
Syenite	$100-10^6$
Gabbro	$100-10^6$
Peridotite	$3 \times 10^3 - 6.5 \times 10^3$
Granite	$160-3.6 \times 10^6$

The IP method records the time it takes for the voltage to decay to zero when an applied current is switched off, and subsequently, the time it takes for the voltage to build up again when the current is reapplied (Reynolds, 2011). The measurements can be indicative of geological factors such as mineral composition and water saturation.

3.3.2.2　ERT and IP data acquisition

The ERT survey was done along a 200 m profile, with an ABEM Terrameter-LS provided by NGI, using multiple gradient protocol, a 2 m electrode spacing and a threshold of 10 Ohm. The soil was soft and unfrozen. During the survey, induced polarization (IP) was also measured. A handheld differential GPS (10 cm precision) logged xyz position of every electrode and was used to correct for topography.

The inversion of the ERT data was done using res2dinv by Geotomo Software (Gan, 2017), provided by NGI.

3.4　Runout simulations

In the runout simulations, the program Dynamic Analysis of landslides in Three Dimensions (DAN3D) was used. The program was developed for the runout analysis of extremely rapid flow-like landslides, and is a calibration-based model (McDougall, 2006). This means that the rheological parameters are defined by back-analysis, in which different sets of parameters are first input on the basis of knowledge of the materials involved, and then tuned to best reproduce the events observed in reality. DAN3D was chosen for the abovementioned reasons, and for being available for free for academic use. The model uses "a meshless, Lagrangian numerical method adapted from Smoothed Particle Hydrodynamics to discretize and solve the depth-averaged equations of motion for an "equivalent fluid", a hypothetical material governed by simple rheological relationships" (McDougall, 2006). The in-data are grouped into control parameters, grid files and material properties.

The control parameters include number of material types to be simulated, number of particles to be simulated and the erosion rate (which DAN3D will calculate based on length of the erodible zone and initial and final slide volume). The erosion rate parameters were calculated from aerial photography, GPS data and manual measurements done in the field, using ArcMap.

The grid files consist of the path topography file, source topography file and erosion map file. The path topography file is defined as the topography of the sliding surface over which the slide flows, and the source topograhpy file defined as the depth topography of the sliding mass at time step t = 0 (Hungr, 2010).

An erosion map can also be added, defining the individual parts of the landslide path with a number, related to their material property. This is only necessary if one wants to simulate the effect of different materials through the landslide path (Hungr, 2010). The gridded map files need to have the same amount of grid nodes not exceeding 1000 nodes on each axis, and the same spacing.

The path topography file is a Digital Elevation Model (DEM), and was created from Felles Kartdatabase (FKB) (Kartverket, 2016) contour elevation data with an equidistance of 1 m, except for parts of the Norangsdalen 2 dataset, which has an equidistance of 5 m. Due to the low resolution of the Norangsdalen 2 DEM, a new DEM was interpolated from the GPS data gathered in the field. This was done using the kriging function in Surfer. Because this DEM provided increasingly unreliable information outside of the area covered by the GPS data, the DEM was merged with the 5 m DEM outside of the channel area. The contours used at Kvam and the upper parts of Norangsdalen 2 are based on data preceding the landslide events, while the data at Årset and the lower parts of Norangsdalen 2 and the GPS data are gathered after the events. The DEMs were clipped and converted into a .grd file readable by DAN3D in several steps using Arcmap, Scripter (an extension of Surfer) and Surfer. The source topography file was prepared assigning the nodes in the release area values based on the depth of the scarp, measured in the field, and blanking all nodes outside of the release area. Erosion map was not used. A detailed guide on the making and conversion of the path topography and source topography files can be found in Dahl (2011).

As Norangsdalen 1 is the results of several events during more than 60 years, tuning a single event simulation to field observations would be a misuse of the field observations. Also, the available DEM only had a 5 m resolution, and satellite and GSM coverage was insufficient to produce GPS data for interpolation of a high resolution DEM. For these reasons, Norangsdalen 1 has not been simulated.

The material properties include frictional, Newtonian, plastic, bingham and vollemy rheologies (Dahl et al., 2013). 10 different parameters are either disabled, or enabled and can be defined, depending on the choice of rheology. Several materials can be defined at the same time, and will govern the material behavior within each zone defined in the erosion map, depending on their assigned number. The parameter values tuned (ξ and μ) used in the

simulations are listed in the results section, and the finaloutput.txt files for each simulation are appended (Appendix 2) and contain details on input and output parameters.

As the rheology selected was the Vollemy rheology in accordance with the recommendations of McDougall (2006), the frictional (μ) and turbulence (ξ) coefficients had to be tuned to fit the observations. Based on modeling cases in McDougall (2006) internal friction angle (φ_i) was set to 35 °, which is reasonable for soils with this size distribution (Ameratunga et al., 2016, Bell, 2002). Dynamic basal friction angle (φ) was set to 34 ° as $\varphi<\varphi_I$ is necessary when working with friction-type flow resistance laws (Dahl et al., 2013). The initial friction coefficient (μ) was estimated using equation 2.9 and 2.10, using the unit weight of the sample and the unit weight of water, and tuned to produce the runout length corresponding to field observations. Simulation 1 (Table 7, section 5.3), for all sites, were done using the initial friction coefficient.

The turbulence coefficient (ξ) was initially set at 1000 m/s^2 as an intermediate of the parameter estimated in similar studies (Bertolo and Wieczorek, 2005, Dahl et al., 2013, McDougall, 2006), and subsequently 1500 m/s^2 and 500 m/s^2. Velocity is mostly used to tune the turbulence coefficient (Dahl et al., 2013) and as little velocity information was available only one additional value was tested at Norangsdalen 2.

Unit weight was derived from lab results. Max erosion depth is based on field observation of deepest channels and depth to bedrock at Norangsdalen 2 and Årset. As geophysical data were available at Kvam, these data were used to estimate this parameter at this site.

Results are extracted from the output file of DAN3D, and by superimposing the depositional grid file on a map in ArcMap. The program does not calculate total runout length, instead providing coordinates of each particle at each time step. For this reason, the horizontal distance between the GPS coordinates from the top of the release area and the depositional front of the thickness grid file was used (Figure 22). A list of input parameters for each site is listed in appendix 2.
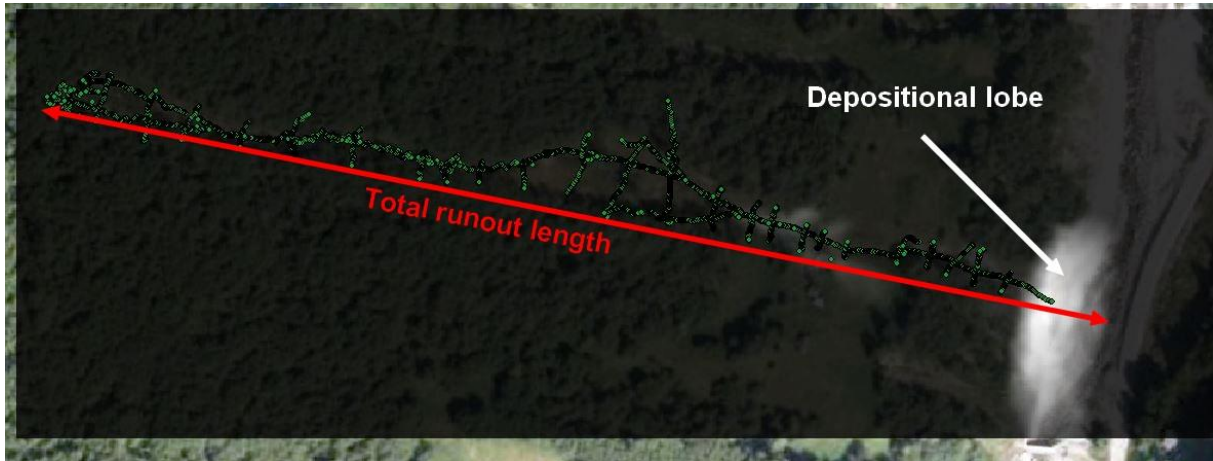
Figure 22: The thickness grid file provided at the final time step of the simulation, superimposed on an aerial photography with the GPS profile enabled. This particular simulation was done at Kvam.

Note also that in sections 5.3.1 and 5.3.2, the final volume of the flowing masses, calculated throughout the flow path by DAN3D, includes masses deposited through the transport zone, while the values to which they are compared are the volume of the depositional area, measured in the field. Volume estimated in the depositional area was chosen in these cases because it is believed to have higher accuracy than the volume estimated through the channel/transport zone and produced less than 8 % deviance, in the case of Norangsdalen 2, or smaller final volume, in the case of Årset. As such, one would expect the simulations to produce a slightly higher final volume in these two cases. Simulated deposition through the flow path is much smaller than that in the depositional area (Figure 22, Figure 59, Figure 60, Figure 61), and this effect is not expected to produce a large deviances.

3.5 Velocity estimation

Few features on which velocity estimation could be done were observed in the field. However, at Norangsdalen 2, estimating the velocity from the elevation difference (superelevation) between the inside and outside of a channel bend was attempted. The method uses the simplified forced vortex equation

$$U = \sqrt{\frac{g \Delta h \, r c}{b}} \qquad (3.6)$$

where g is the gravitational acceleration, Δh is the elevation difference between channel sides/levees, and r_c is the radii in an imaginary circle, in which the bend would fit. b is the width of the channel. The equation was originally derived for water, and b is often multiplied with a correction factor (k) to correct for this, though estimates of such a factor varies with multiple orders of magnitude (Prochaska et al., 2008).

Similairly, velocity can be estimated on the basis of the runup height of masses deposited on obstacles or the opposite valley side or river bed:

$$U = \sqrt{2gh} \tag{3.7}$$

In this equation, h is the runup height. The equation assumes the obstacle to be oriented perpendicular to the flowing masses and is found to yield velocities up to 30 % lower than those observed in large-scale flume experiments (Jakob, 2005a).

3.6 Weather data

The weather data was extracted from www.senorge.no (2017). Interpolated 24 hour precipitation has been used at Årset and Kvam. In addition, hourly precipitation from nearby stations have been used at these sites. Sandersen's (1996) equation (2.7) has been used, as outlined in section 2.6.4. Estimations of the likelihood of landslides, from the landslide and snow avalanche site www.varsom.no (2017), ranging from 1 (green) to 4 (red), have also been extracted.

3.7 Combining the data

This section gives a short overview of the intended use of the data extracted using these methods.

3.7.1 Field observations and measurements

The measurements and observations done in the field, and logged in the field work form, provide information valuable in the characterization of each landslide. For the purpose of the runout simulations, the observations have been vital in the making of the source depth file and estimation of the erosion rate (from initial and final volume and total length of erodible zone).

The observations were also useful in the verification of the geometries produced during simulations.

3.7.2 Grain size analysis

For the purpose of this thesis, grain size distribution is used to differentiate soils and provide an indication to why specific layers failed, while others did not. The unit weight of the source material is also used as an input parameter for the runout simulations and the calculation of the bulk basal friction (μ), as outlined in sections 2.7 and 3.4.

3.7.3 Geophysical methods

The data provided by the geophysical method is intended to establish the depth to bedrock, and thus the maximum erosion depth parameter for the runout simulations. The bedrock topography will also be used in the assessment of likely conditioning and triggering factors.

3.7.4 Runout simulations

The output of the runout simulations, primarily runout length, final volume and to a lesser extent velocity, are used to verify that sufficient input parameters are provided by the field work form and field work.

3.7.5 Weather data

The weather data has primarily been used to give an indication of the circumstances under which the landslides initiated. Thus, this data is used in the characterization of the sites, and it has no use in the runout simulations.
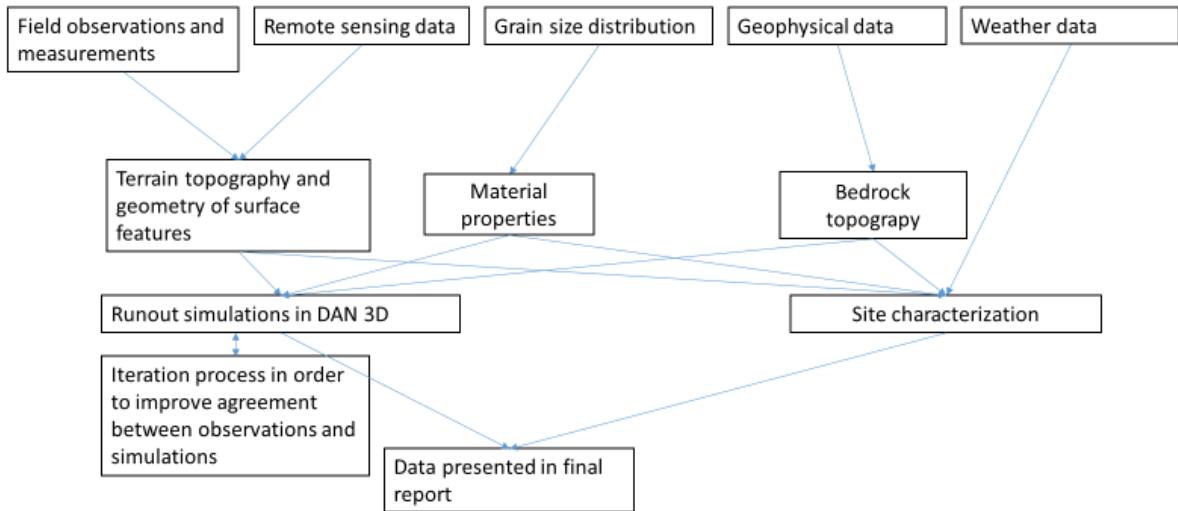
Figure 23: Chart of the intended use of the methods involved and the final product.

4 Description and observations

This section will present the sites and the observations done at each of the sites in the field, from aerial photography and geological maps. Aerial photographies (except drone images) and maps are oriented with the top facing north. Left and right is always given relative to the flow direction.

4.1 Geological history and climatic context

Among the most important instruments in shaping present day geology are the repeated glaciations and deglaciations throughout the last three million years, the effects of which are most obvious in U-shaped valleys and glacial deposits (Olsen et al., 2013). Estimates of Quaternary glacial erosion rates range from 10^{-4} mm/year to 10 mm/year illustrating not only the erosive forces shaping the terrain, and redistributing masses, but also their uneven distribution (Delmas et al., 2009). Quaternary glaciations have eroded the terrain selectively, meaning that pre Quartenary topography, shaped by other erosive agents such as rivers, have been conditioning the glacial erosion. This has in turn resulted in mountainous areas with deeply incised throughs, and virtually unaffected uplands (Olsen et al., 2013). Thus, large parts of Norway are dominated by landforms with large height differences within relatively short horizontal distances, or in other words, steep gradients. The majority of the subaerial soil in Norway is comprised of till (Schanche, 2014).

The depth of which the lithospheric plates float on the mantle is largely dependent on the masses weighing down the lithosphere itself. Thus the loading and unloading of ice, following glacial and interglacial periods, causes the system to move towards a new isostatic equilibrium (Lambeck et al., 1991). The release of loading also means that some areas are subjected to less vertical pressure than previously, rocks previously unexposed reach the surface, and masses of both rocks and soils reach a higher level of potential energy. This means that the equilibrium of the slopes themselves are also changed. The combination of isostatic rebound and volume of water in the oceans (eustasy), results in large changes in relative sea level, and large parts of Norway were previously below sea level.

According to the Köppen-Geiger (1936) system of climate classification, there are two major climatic regions in Norway:

1: Marine west coast climate (Western Norway)

2: Continental sub-arctic climate (Eastern Norway).

(Sandersen et al., 1996).

Generally, the marine climate along the west coast of Norway, where Norangsdalen 1 and 2 and Årset are located, receives more precipitation than do the inland areas where Kvam is found (Hanssen-Bauer, 2015). The west coast has most of the precipitation falling during autumn, and winter flooding is more common, often as a combination of rainfall and snowmelt during the mild winters (Tollan, 1977). Thus, water supply will be highest during the autumn and winter on the west coast, while the inland will experience a large input of water during the spring melting. The slope aspect is also important, as the south west and west facing slopes see high meltwater production as they are more exposed to solar radiation and wind. On the west coast they are also subject to orographic precipitation (Sandersen et al., 1996). Meyer et al. (2012) found that south west facing slopes of the Norwegian mountain ranges had a hydro-meteorological regime promoting debris flows.

4.2   The sites and why they were selected

The sites are located in the counties of Oppland in central Norway, and Møre og Romsdal, Western Norway (Figure 24). The four landslides involve different characteristics and mechanisms, as outlined in the objectives of the thesis (section 1). The Kvam and Norangsdalen 1 sites act as examples of channelized landslides, Norangsdalen 1 having the most well defined channel, while Årset is an open slope. Norangsdalen 2 acts as an intermediate, in regard to channelization. Norangsdalen 1 has evolved over time and does not display one distinguishable event, while the three others clearly do. Climatically, Kvam is located farther inland in a cold temperate climate, while the other three are located close to the coast in a milder climate (Meteorologisk Institutt, 2017). The sites should thus provide insight into some of the differences and similarities of different kinds of debris flows and debris avalanches, and give a good indication on whether or not the field work form contains sufficient parameters to characterize the events.

Figure 24: Map of Southern Norway, with the four selected sites.

The landslides in Norangsdalen did not impact infrastructure or buildings. Kvam, however, experienced flooding and numerous landslides in June 2011 and May 2013 damaging local buildings, roads and the railway. In 2011, the estimated damages in Oppland county on roads

alone amounted to 162 million NOK (Statens vegvesen Region, 2012). The total societal cost of the 2013 flooding and landslides in Gudbrandsdalen are calculated to 1.1 billion NOK (Siedler, 2013). The Årset site, while in a less populated area, destroyed one house, damaged others and blocked the local road. Limitations on land use were imposed on the land owner and have been source of conflict in the years following the event (H. Aarseth, pers.comm., 2016).

4.3 Norangsdalen 1

Norangsdalen 1 is located in the Norangsdalen valley, on an east facing slope. The top of the channel is located at 70136E 6917600N, at 455 m.a.sl. The whole track is visible from road 655, and the slide is clearly channelized. Aerial photography shows a distinct channel as early as 1962 (Figure 25), indicating a continuous process evolving the channel over several decades. The land slide has a total runout length (L) of 408 m and an elevation difference (H) of 193 m giving a H/L ratio of 0.47 and a travel angle of 25 °.

Figure 25: Aerial photography of Norangsdalen 1 from 1962 (bottom) and 2015 (top). The site being investigated is in the centre, marked with red arrows. The scale in the middle is 50 m across. Modified from Norge i bilder (2017).

4.3.1 Terrain

The slope in which the channel is eroded starts at the foot of the valley mountainside. The average slope from the mountainside to the valley floor is 21 °, and it has a straight surface geometry. The area in general is dominated by overlapping depositional lobes from the valley floor up to about 450 m.a.sl. and is riddled with channels and landslides of differing sizes. The site is neighbored by a similar channel in the north, originating from the same area, and there are less developed channels to the south. Towards the distal parts of the depositional area, a small lake can be found. The valley is u-shaped, thus the slope angle decreases towards the valley bottom. The slope itself has a straight to divergent surface geometry (Figure 7,

section 2.6.1) while the mountainside above the channel has a convergent, syncline, surface geometry, with ridges on both sides (Figure 28).

Figure 26: The landslide area, observed from the road 240 m east. The site Norangsdalen 1 is the one to the left in the picture. Visible in the picture is the incision in the mountainside that forms the convergent geometry of that area. The slope around the channel displays a divergent geometry.

4.3.2 Soil characteristics

The Geological Survey of Norway (NGU) geological map (Figure 27) lists the soil in the area as a continuous cover of landslide material, in some areas of high thickness (NGU, 2017b). This is supported by field observations of angular rocks, and what seems to be oblique stratification (Figure 29). The material in which the channel is eroded consists of coarse angular clasts ranging from gravel to boulders, surrounded by a matrix of grey fines. A boundary between a darker and lighter looking soil was identified in the channel, and both were sampled. Grain size analysis of the samples will be elaborated on in section 5.1.1.
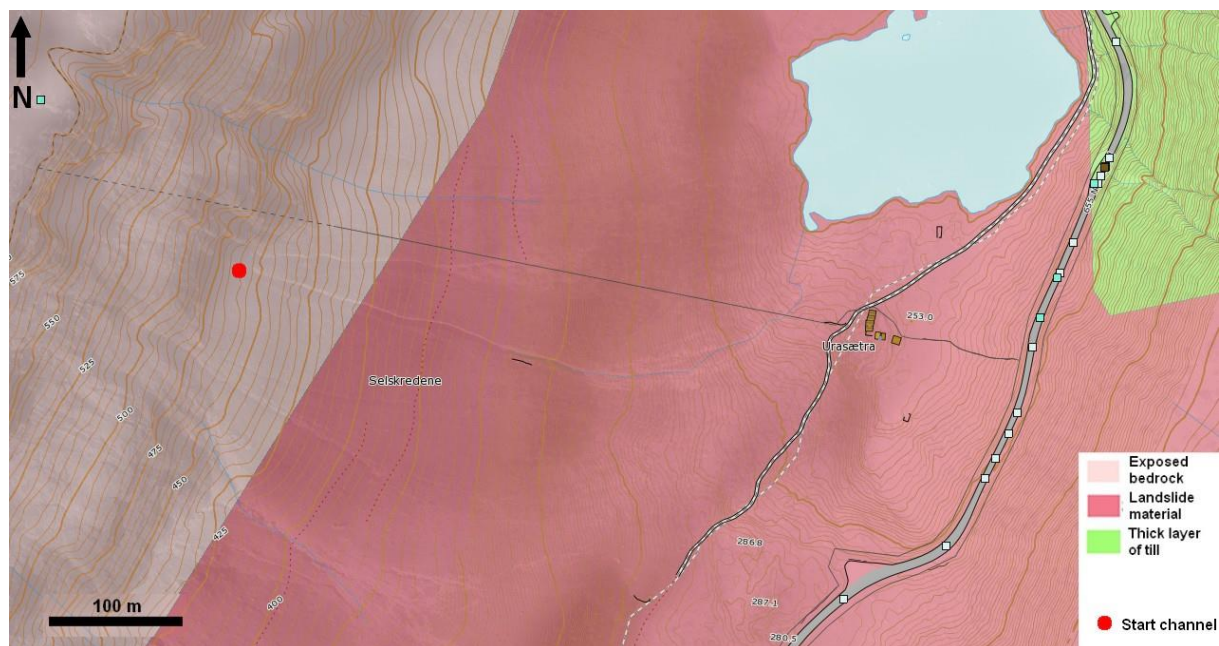
Figure 27: Sediment map with topography and inventory, superimposed on an aerial photography of Norangsdalen 1. The stream in the depositional area was not observed in the field. Squares marks previous events. Grey suqares are registered snow avalanches, blue squares are events of unknown type and brown are landslides in soil. Note that registrations done on the road often mark the location of the person registering the event, and that the event itself probably originates on the slopes above. Based on the NGU (2017b) geological maps, Norge i bilder (2017) and skrednett (2017).

4.3.3 Bedrock

The bedrock in the area is listed as dioritic to granitic gneiss and migmatite (NGU, 2017a). During the field surveys the bedrock was deemed to be gneiss, though no further analysis has been conducted, and will not be the focus of the thesis. In general the bedrock in the area has east-west strike orientation, with a southward dip of 20-40 ° (NGU, 2017a).

4.3.4 Vegetation

As visible from Figure 25 vegetation is sparse around most of the channel length, with grass, bushes and heather dominating the slope. Approaching the depositional area, birch covers an increasingly larger part of the ground, reaching heights of up to 2 m at the valley floor. The general impression is one of decreasing vegetation towards the mountainside, with the mountainside itself only covered by rare patches of grass.

4.3.5 Release area

The release area itself is not self-evident. The channel starts at the transition from the mountainside to an area where the bedrock is covered by coarse sediment filled deposits and the slope reaches ~40 °. Above this point, there are furrows in the bedrock from running water, which terminate into the start of the channel. There are no visible sources of larger soil masses (Figure 25), except for sporadic thin vegetated layers of soil and loose rocks. There is however a structure of low angled ledges of rock in the mountainside, where some masses, primarily snow or colluvium, could accumulate.

Figure 28: Picture taken at the top of the channel, viewed from below. Note the exposed rock in the channel bed, and on each side of the area above forming a convergent geometry. The white dotted line at the top of the picture indicates ledges where masses could accumulate.

4.3.6 Transport zone

The transport zone is a well-developed channel approximately 250 m long with an elevation difference of 142 m giving an average slope of approximately 30 °. At the start, the channel is

eroded down to the bedrock (Figure 28), and has a depth of 1.8 m, a top width of 4 m and a bottom width of 2 m. This 8 m section has been designated the start section. A sample was taken in this area (sample 16). The bedrock is exposed, stepwise sinking with the channel depth increasing accordingly.

The next 150 m of the channel have been designated the mid-section and it has a depth ranging between 2 and 2.5 m. Width at the channel top is 4-5 m and at the bottom 1-2 m. Inclination of the channel walls are generally steep (~ 60-70 °). Except for the first 30 meters, the bedrock is not exposed in this section. The channel bed is filled with gravel reaching cobble size. On the right side there seems to have been eroded an extra 'step' above the channel top and this is also a profound feature through the first 70 meters of the channel. At its widest, the level expands the channel top width 5 m, and has an inclination of 5-15 °. Aerial photography from 1962 (Norge i bilder, 2017) shows a wider eroded area in the same segment, reaching a width of 15 m at the most. The average slope in this segment is 29 °.

There is evidence of undercutting at the sides as detached vegetated slabs of soil can be found along the channel sides and bed. The rocks exposed in the channel sides seem to be obliquely stratified (Figure 29). 90 meters from the top, a large boulder, ~70 cm in diameter, is blocking parts of the channel, and a lot of smaller rocks are stacked behind and around it in a minor dam. The depth here is 2.3 m, and the width is 5 m at the top of the channel, and 1.4 m at the bottom. 10 meters further down there is another area of stacked rocks causing a second dam. A sample was taken here as well (sample 2).

Figure 29: Picture taken approximately halfway down the channel, looking up-slope. Red lines display oblique stratification. Also visible in the image are the angular boulders.

During the second field trip, under colder weather conditions, it was discovered that there seemed to be two layers of soils, one darker grey (topmost layer), and one lighter red (bottom layer). These were sampled (samples 4 and 7 respectively).

The next 150 meters have been designated the end section of the channel. The channel depth gradually decreases and there are locally thick deposits building a blockage of the channel (dam).
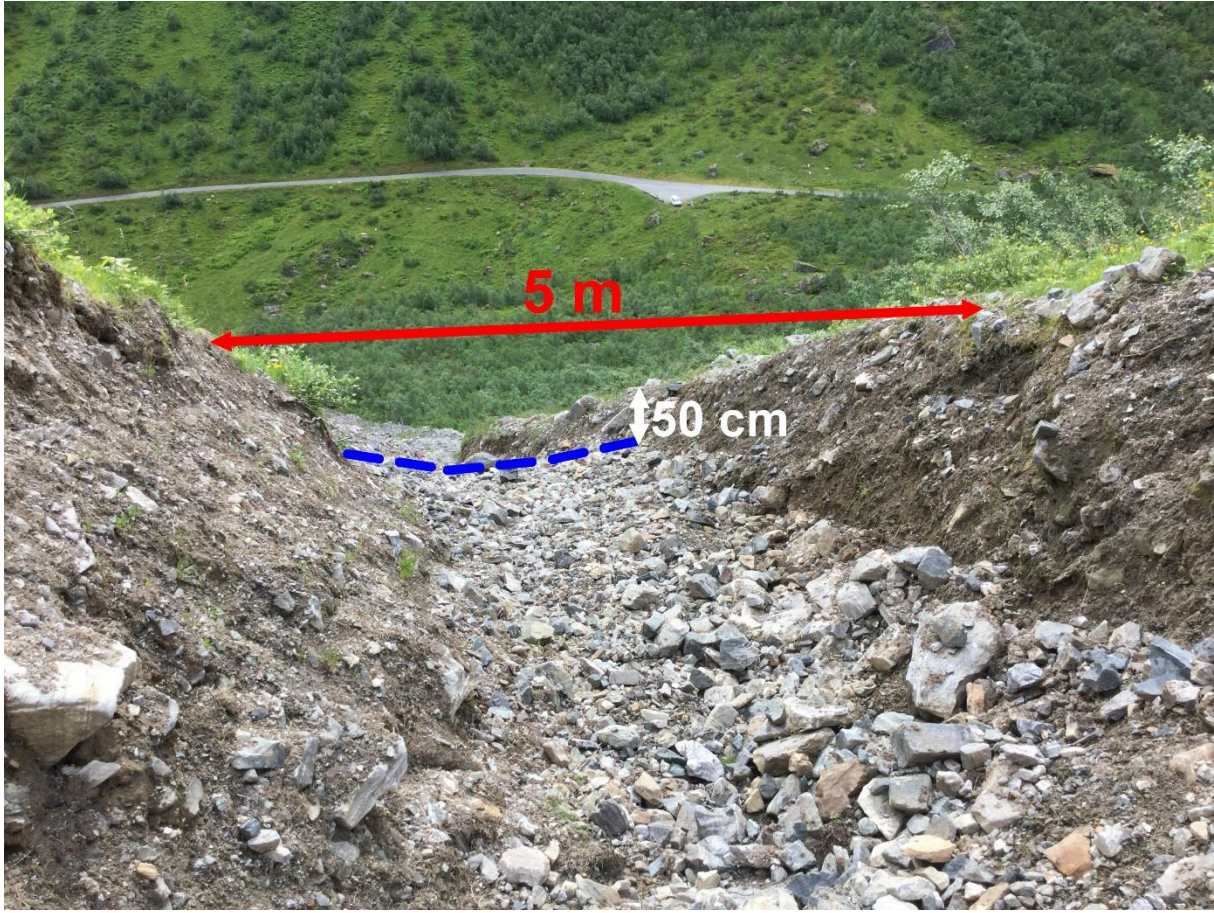
Figure 30: Picture taken aproximately 70 m from the end of the channel, facing down slope (east). In the centre the dam is visible, the top of which is marked in blue.

Towards the last 60 meters, the channel opens up considerably, and deposition is further increased. At the opening of the channel, a depth of 1.5 m, width of 5.4 m at the top and 2.6 m at the bottom was recorded. The channel walls had an inclination of 45 ° and the slope angel in this area is ~16 °.
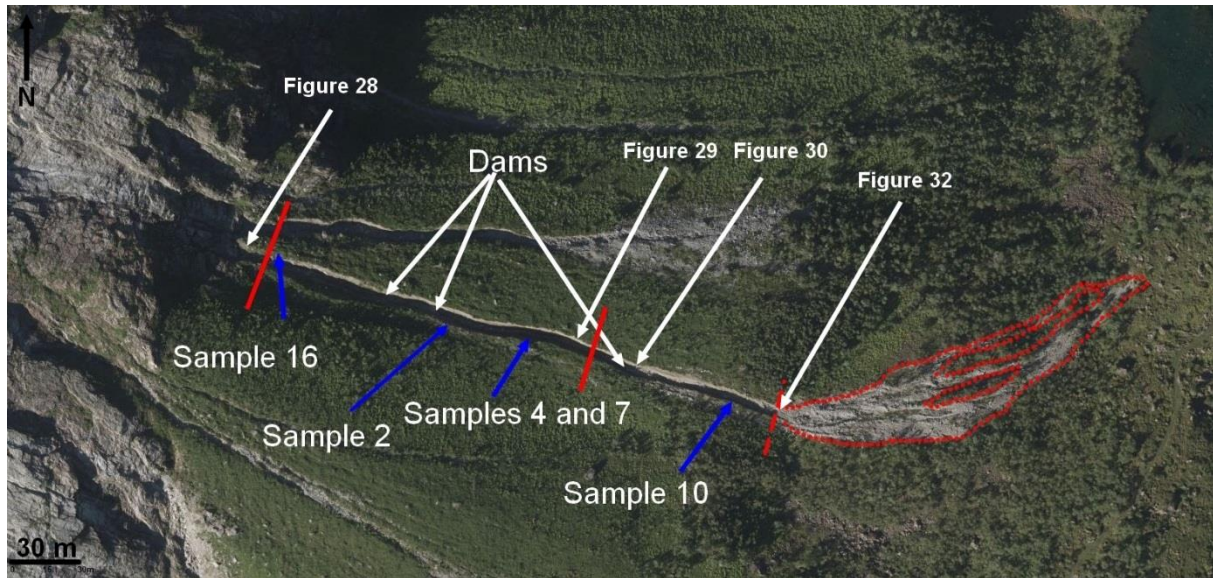
Figure 31: Overview of Norangsdalen 1, with the dams, figures and sample sites marked. Red lines indicate transition between segments, and the dashed red line the end of the channel. Edited from Norge i bilder (2017), photography from 2015.

4.3.7 Area of deposition

While larger rocks are dominating the channel bottom, similar rocks are dominating the entire depositional area, defined to start where the channel stops. The depositional area follows the topography and bends towards the nearby lake, and has a maximum width of 37 m and a length of 80 m. The whole area is not equally covered, and individual ridges and channels can be found, consisting primarily of rocks >32 mm. Some are as deep as 0.5 m, and there is vegetation separating the three main arms of the depositional area, each having built distinct levees and subsequent channels. Large blocks can be found in the levees and at the top and front of the lobe, which display some very sharp front and channel angles, some places more than 45 °. Aerial photographies show the depositional lobe to develop new arms between events, though temporal resolution is too limited to establish when each arm developed.

Figure 32: The depositional area of Norangsdalen 1, looking down slope (east), observed from the end of the channel.

4.4 Norangsdalen 2

Norangsdalen 2 is located in the Norangsdalen valley, 4.5 km north of Norangsdalen 1 on a south west facing slope. The top of the release area is located at 70581E 6922285N, 545 m.a.sl. Aerial photography shows the event to have occurred between 2013 and 2015. The total runout length (L) is 675 m, and the total elevation difference (H) 417 m giving a H/L ratio of 0.62 and a travel angle of 32 °. A distinct channel develops towards and over the depositional lobe. The initial volume of the flowing mass is estimated to 33 m^3, and the final volume of the depositional are 7040 m^3.

Figure 33: Sediment map with topography and inventory, superimposed on an aerial photography of Norangsdalen 2. On the bottom left corner, a rock avalanche from 2003 is registered. Based on the NGU (2017b) geological maps, Norge i bilder (2017) and skrednett (2017).

4.4.1 Terrain

The slope in which the slide has passed has several easily visible landslides and channels up and down the valley every 100-200 m. In general, the slope has a straight geometry, and an average slope angle of 30 °. The ridge at the top of the mountainside however is curved towards the south, giving this area a more convergent geometry. Aerial photography shows evidence of smaller events parallel to the site being investigated, the closest located 15 m to the south-east. The valley floor and area immediately around the depositional lobe is used for

68

agricultural purposes, both as cropland and for the grassing of cattle. The terrain surrounding the landslide is dominated by large blocks.

Figure 34: Norangsdalen 2, viewed from the road 270 m to the south-west. The depositional area is mostly hidden behind vegetation.

4.4.2 Soil characteristics

The NGU geological maps (Figure 33) list the soil cover as landslide material (NGU, 2017b), of more than 0.5 m thickness. This agrees well with field observations, though the upper parts of the slope display a lower soil cover thickness.

4.4.3 Bedrock

The bedrock in the area is listed as dioritic to granitic gneiss and migmatite (NGU, 2017a). During field observations, the bedrock was considered to be gneiss. The bedrock observed in the release area and upper transport zone was very fractured and could be peeled apart in several areas. In general the bedrock in the area has east-west strike orientation, with a southward dip of 20-40 ° (NGU, 2017a).

4.4.4 Vegetation

The slope is densely vegetated with birch, grass and moss. The trees are several meters tall, and though the vegetation density and tree height decrease towards the release area, there are still trees up to 3 m height. The scarp around the release area reveals a high density of short roots. Aerial photography shows the landslide path to have been densely vegetated prior to the landslide.

4.4.5 Release area

The release is located at 545 m.a.sl. and is 8-10 m wide. A slope angle of 39 ° was measured. The bedrock is exposed and the depth is between 0.5 m and 0.25 m. The bedrock is at a significantly shallower depth on the right side than on the left (Figure 35), where it is not exposed. The surroundings are densely vegetated, except for a small (12 m x 12 m) area of exposed bedrock 10 m north-east of the release area. The direction between this patch of exposed bedrock and the release area matches the landslide path. 19 m below the top of the scarp, the area narrows to 5 m as a slab on the left side is still intact.
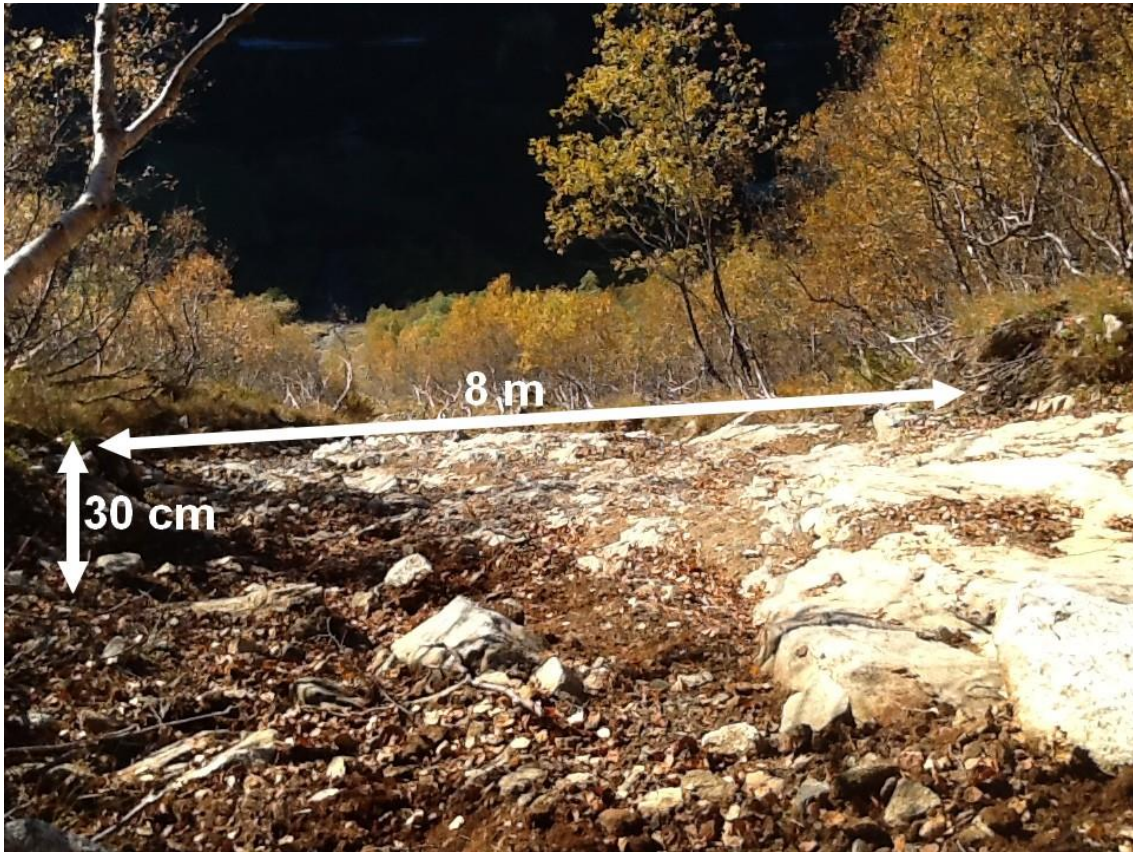
Figure 35: Picture taken from the top of the release area at Norangsdalen 2, looking down slope (south-west).

4.4.6 Transport zone

The transport zone has several distinct segments (Figure 37), and a total length of 530 m. The first segment is 130 m long and is characterized by a width of 3-7 m and vegetated patches with trees still present in the main path. Several of these patches have large masses accumulated upstream of them, while erosion has removed all vegetation around them. Where these patches are present, the track tends to widen, whereas similar patches on the left and right margins relate to a tightening. This area also sees several smaller failures parallel to the main path, joining it once it widens. The slope in this segment is 39 ° on average, though there are large fluctuations as exposed bedrock produces low gradients (~10 °) where coarse gravel is deposited in some areas. It was noted that in the lower 50 m of the upper segment, exposed bedrock seemed more weathered and some areas could be picked apart much more easily than the bedrock exposed in the area above. The erosion is generally shallow, reaching 0.5 m where channels develop, and the bedrock is exposed throughout this segment.

71

140 m from the top of the release area, the track opens up, initially 10 m wide. After 30 m a boulder, 4 m diameter, blocks the path (Figure 36), accumulating large rocks above it. An intact slab of vegetated soil is still intact below it, and on the side facing downstream, a birch tree is left in place, indicating that the rock has been rotated ~90 °. Bedrock was not exposed below this rock. A channel is eroded above the large rock, which continues on both sides of the rock and meets 170 m further downslope. At the time of the survey, these channels were filled with coarse gravel, and never exceeded a depth of 0.5 m.
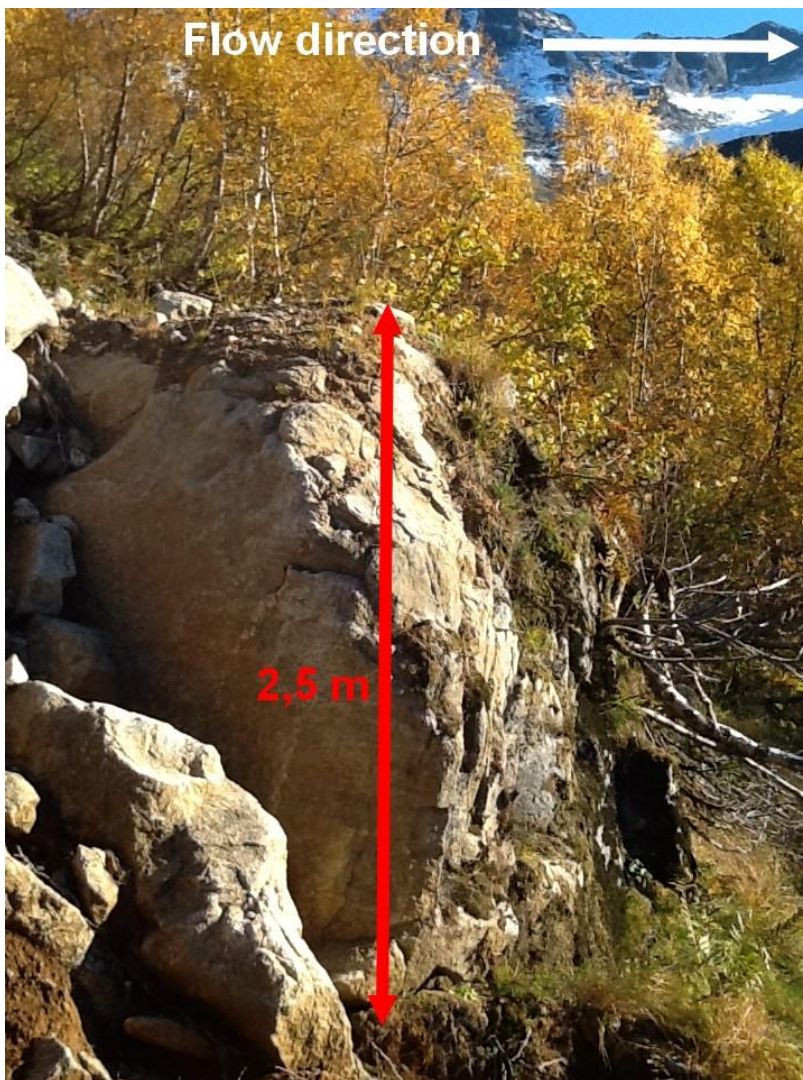
Figure 36: The large boulder dividing the channels in the upper part of the middle segment of Norangsdalen 2 transport zone.

The main track, in which these channels are eroded, widens downslope of the rock, reaching a width of 34 m at its widest. This segment is ~200 m long, has an average slope of 35 °, and has been designated the mid-section. Throughout this segment, there is little deposition at the

72

flanks, and except for the vegetation on the slab below the large rock, little vegetation is intact in the main track.
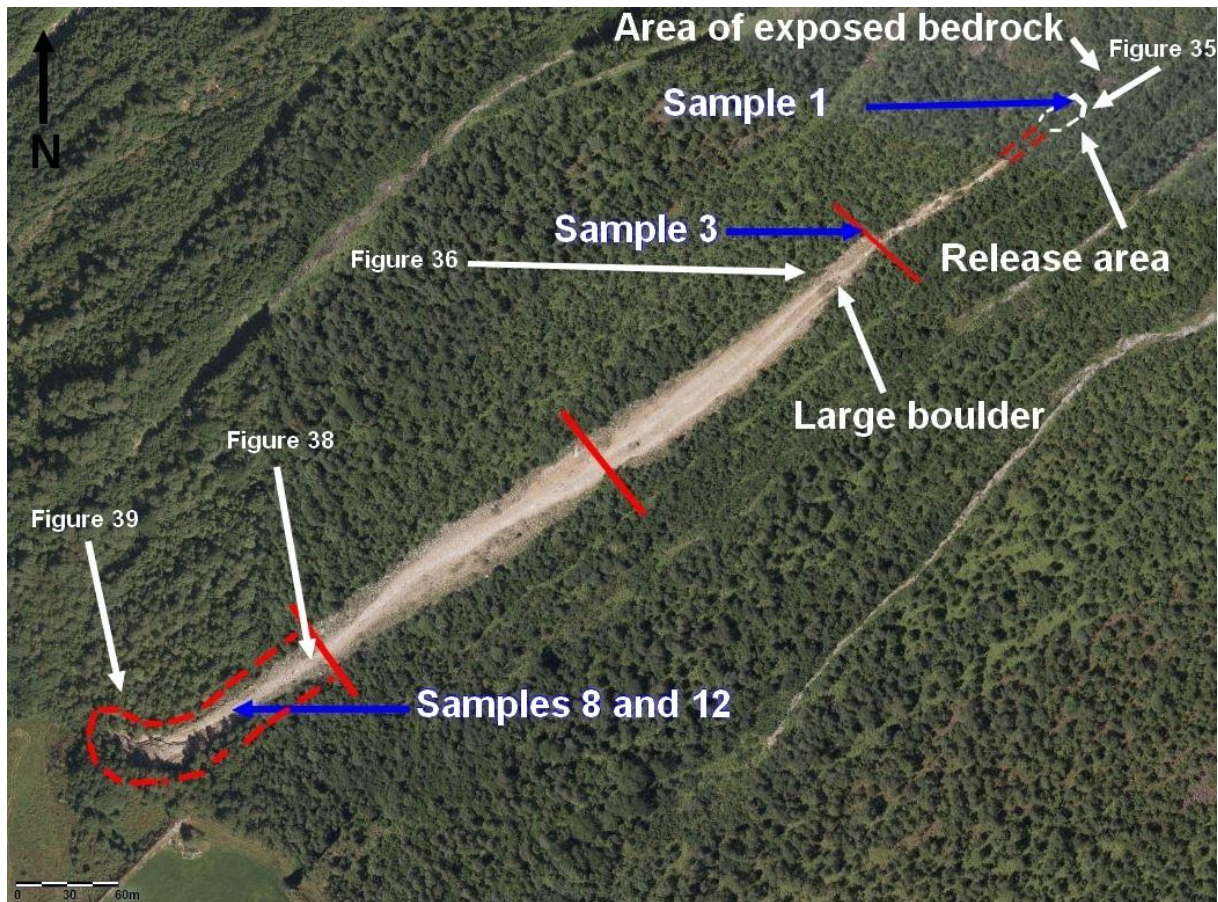
Figure 37: Overview of Norangsdalen 2. Red lines mark the transition between segments. Separated red lines mark the part of the path not visible in the picture (top) and depositional area (bottom). The scale on the bottom left is 60 m. Edited from Norge i bilder (2017), photography from 2015.

The last segment, in contrast to the middle one, displays more deposition, particularly on the left flank which is riddled with debris. The two channels observed further up, join in the top part of this segment, progressing as one down to, and over, the depositional lobe. The segment has a length of ~200 m, and the width is reduced to 10 m at the end, where it terminates into a depositional lobe.

The last 100 m see a buildup of distinct levees up to 2 m above the channel bed. The elevation difference between the levees and the area surrounding the tracks is however approximately 1 m. The segment has an average slope of 31 °, though the lower parts decrease to 27 °.

Figure 38: Picture taken from the depositional lobe of Norangsdalen 2. The channel is visible in the middle. Distance to the release area is aproximately 530 m.

4.4.7 Area of deposition

The depositional area is a distinct lobe, 2 m higher than the surrounding area at the most. The upper limit of the depositional area has been defined from the point that building of the lobe and levees is dominant. It is deposited in an area with an average slope of 22 °, dominated by larger blocks. On its right margin, it is limited by what seems to be old landslide materials. The channel observed through the track continues on the lobe reaching a depth of 1 m, terminating at the front of the lobe. The surface of the lobe is dominated by gravel, up to cobble size, and the lobe front has an inclination between 30 ° and 40 °. There is dense

vegetation all along the margins. On a channel running on the lobe, superelevation was observed and velocity estimation done using equation 3.6, found in section 3.5. The velocity was estimated to be 7.3 m/s. This is however only for one particular surge/phase, and the bulk of the flowing masses might have exceeded this velocity.

Figure 39: The depositional lobe of Norangsdalen 2, observed from the left side.

4.5 Årset

The Årset site is located 10 km north of downtown Ørsta, named after the valley, on a south-west facing slope. The center of the release area is located at 40876E 6939042N, at 637 m.a.sl. The landslide was initiated on the November 15. 2013 at about 23:30, after a period of intense precipitation (NRK, 2013)(H. Aarseth, pers.comm., 2016). The total runout length (L) is 1210 m and the total elevation difference (H) 570 m giving a H/L ratio of 0.47 and a travel angle of 25 °. Initial volume was estimated to 68 m^3, with a final volume of the depositional area of 46800 m^3.

Some minor flooding and landslides were observed during the snowmelting and heavy precipitation on 27. of November 2015, though no large landslides occurred (NRK, 2015). Skrednett (2017) lists a landslide in soil on August 22. 2014, though no information about this event was given by the landowner and is assumed not to have modified the site significantly. The Årset site has previously been included in a general hazard mapping effort in 2015 (Kronholm et al.), and in a more in depth survey, the results of which were published in 2017 (Sandøy et al.).
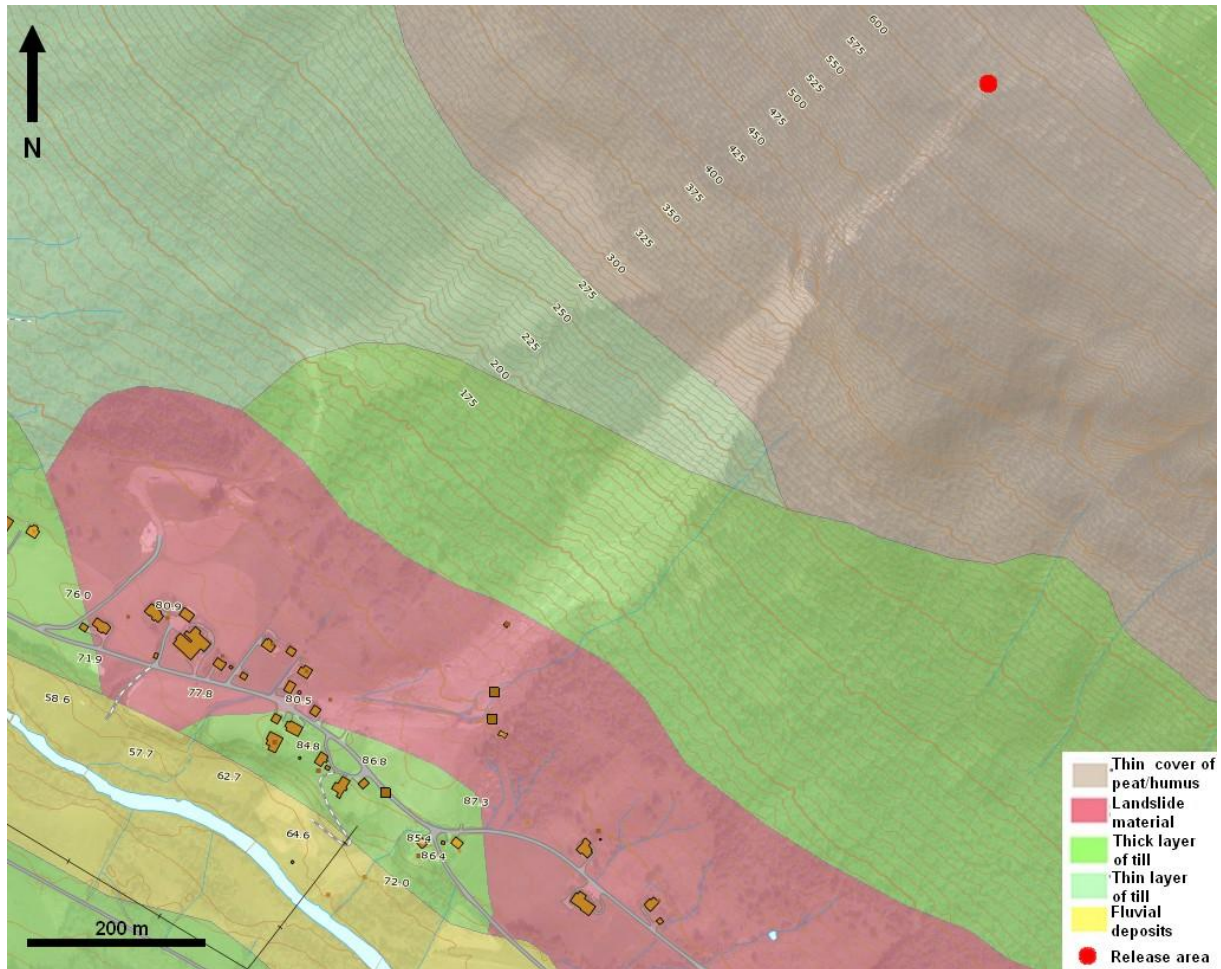
Figure 40: Sediment map with topography and inventory, superimposed on an aerial photography of Årset. Three brown squares, marking landslides in soil, are visible in the depositional area. The upper two designate the event being investigated, while the lower concerns an event in 2014. Based on the NGU (2017b) geological maps, Norge i bilder (2017) and skrednett (2017).

4.5.1 Terrain

The average angle of the slope is 25 °, and the geometry is slightly convergent. 250 m to the north of the release area, a distinct ridge going east to west forms a watershed. At the bottom of the slope, a road passes along the valley floor, and a river runs parallel to the road. There are several waterways and rivers parallel to the landslide being investigated, though none of these intersect the landslide path. These are most profound along the tree line. Fragmented rocks, believed to originate from frost processes, are dominant, mostly covered with a thin layer of peat. There are some patches of exposed fragmented rocks. Two are located within 10 m of the release area, and there are several others in the proximity. Aerial photography preceding the slide shows one such patch in the release area.
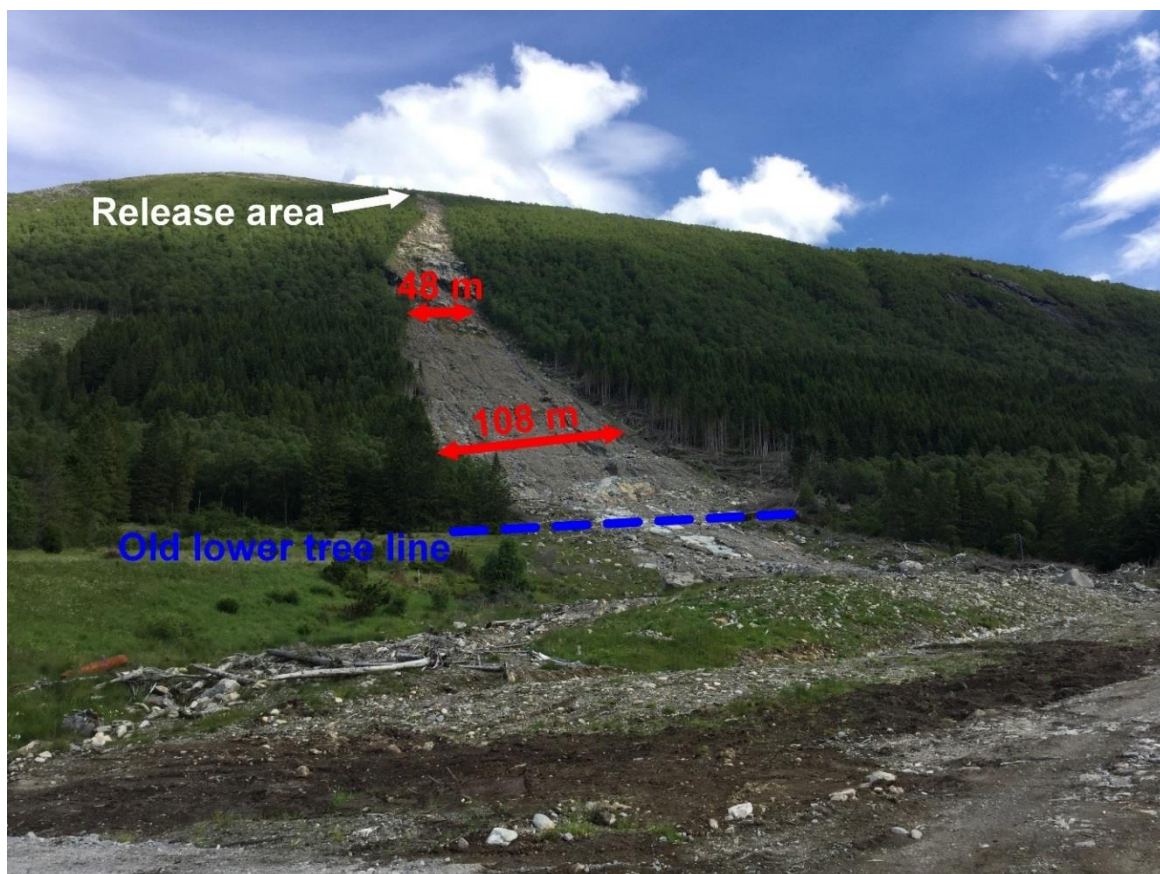
Figure 41: The Årset site viewed from a road constructed on the depositional area of the slide, looking north-east.

4.5.2 Soil characteristics

The soil cover (Figure 40) is registered as humus and peat from the release area down to 275 m.a.sl. The area below this is registered as till, starting with a 90 m strip of partial or thin cover, followed by a full cover of till down to 125 m.a.sl. Landslide material is registered throughout most of the depositional area. The area immediately surrounding the river has fluvial deposits, while till is registered in the lower parts of the depositional area, separating the landslide material and fluvial deposits (NGU, 2017b).

4.5.3 Bedrock

The bedrock in the area is registered as gneiss, with an east-west oriented strike and a southward dip up to 80 ° (NGU, 2017a). This agrees well with field observations. The bedrock exposed in the bottom part of the upper transport zone segment is fractured in some places where it could be picked apart.

78

4.5.4 Vegetation

The slope in general is densely vegetated with birch reaching several meters height, grass and heather up to about 630 m.a.sl. The density decreases approaching the tree line. From 260 m.a.sl. to 150 m.a.sl. a belt of spruce, more than double the height of the birch, has been planted, extending several hundred meters along the slope. 80 m north-west of the landslide path, a 270 x 150 m patch of this belt has been cut down. In the depositional area, there was only grass and bushes prior to the slide, except for the left margin of the depositional area which was densely vegetated. This is largely intact.

4.5.5 Release area

The release area is approximately 8 m at its widest, and 12 m from the top, it narrows down to about 5 m. The depth along the margins range from 0.2 m to 0.4 m, though the middle part of the release area sees some deeper parts, and the average slope is 34 °. Aerial photography shows an accumulation of larger rocks below the narrowing point, prior to the event. The release area is located at the tree line, and the vegetation is generally smaller and thinner than further down slope. At the top of the release area, a small ($< 1m^2$) failure cuts into the surface above, and there is increased erosion below this point, indicating drainage through this point. Except for this furrow, the release area has a very flat surface (Figure 42), not cutting into the layer below. The scarp reveals the failing soil to be overlain by a layer of large rocks covered in peat and moss.
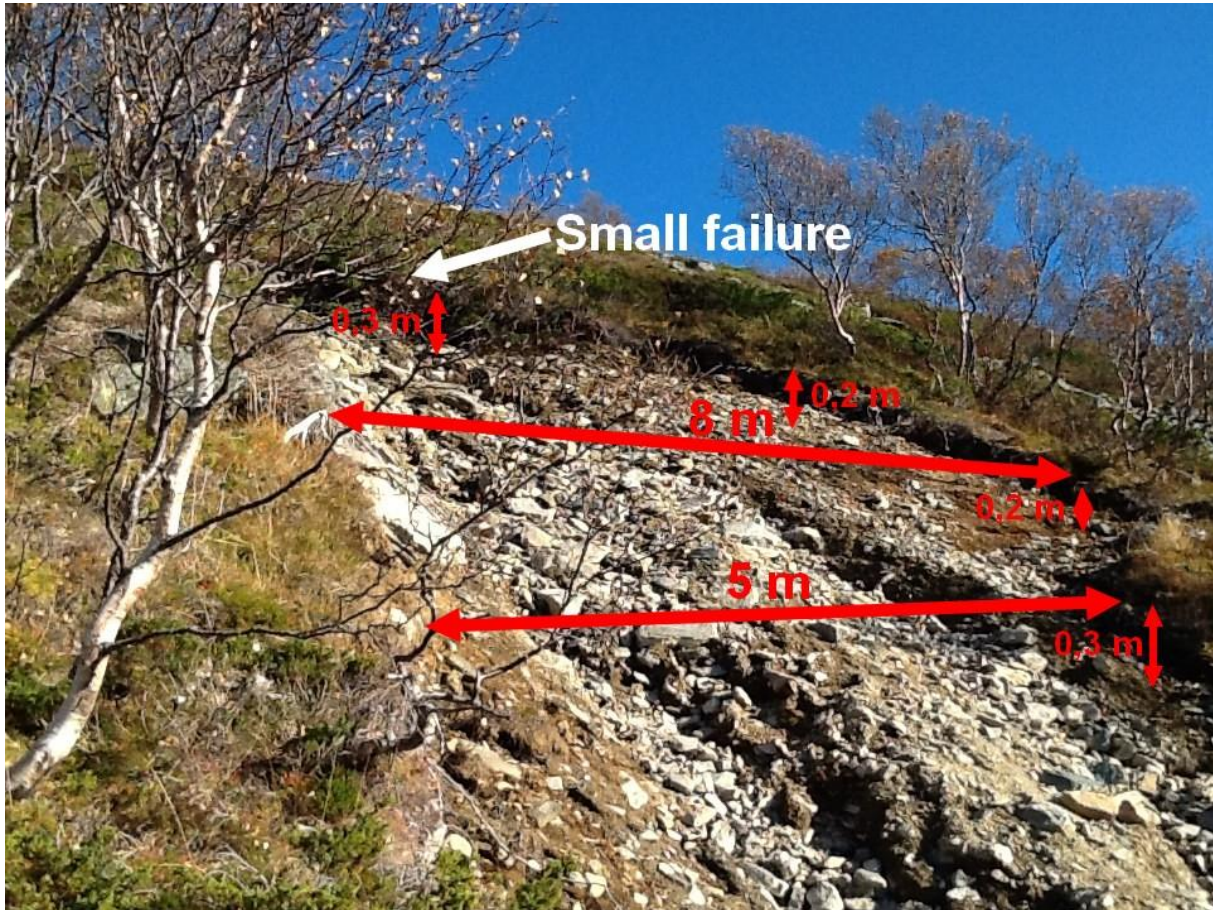
Figure 42: The release area of the Årset site, looking up slope (north-east). Note the predominantly flat surface of the release area.

4.5.6 Transport zone

The upper segment of the transport zone opens at a width of 10 m. It is 230 m long and has a slope angle of 35 °, similar to the release area. This segment, seen in profile, has a concave geometry. The upper part has a flat surface with a 0.4 m deep channel eroded in the middle. The channel, and much of the sliding surface, is covered with gravel of pebble to cobble size. As the gradient increases, 100 m from the start of the segment, the depth of the erosion increases to as much as 2 m at the most. This area also displays a buildup of levees, and larger clasts are deposited in channels and on obstacles. From this point, bedrock is increasingly exposed, becoming the dominant feature in the terrain at 170 m from the start of the segment. Depth of erosion in this area seems to be mainly limited by the bedrock depth.

The upper and lower segments of the transport zone are separated by a 100 m segment of cliffy exposed bedrock, with an equal drop in elevation. This area displays very little

deposition and marginal vegetation. The width increases from 30 m at the top of the segment, to 48 at the bottom.
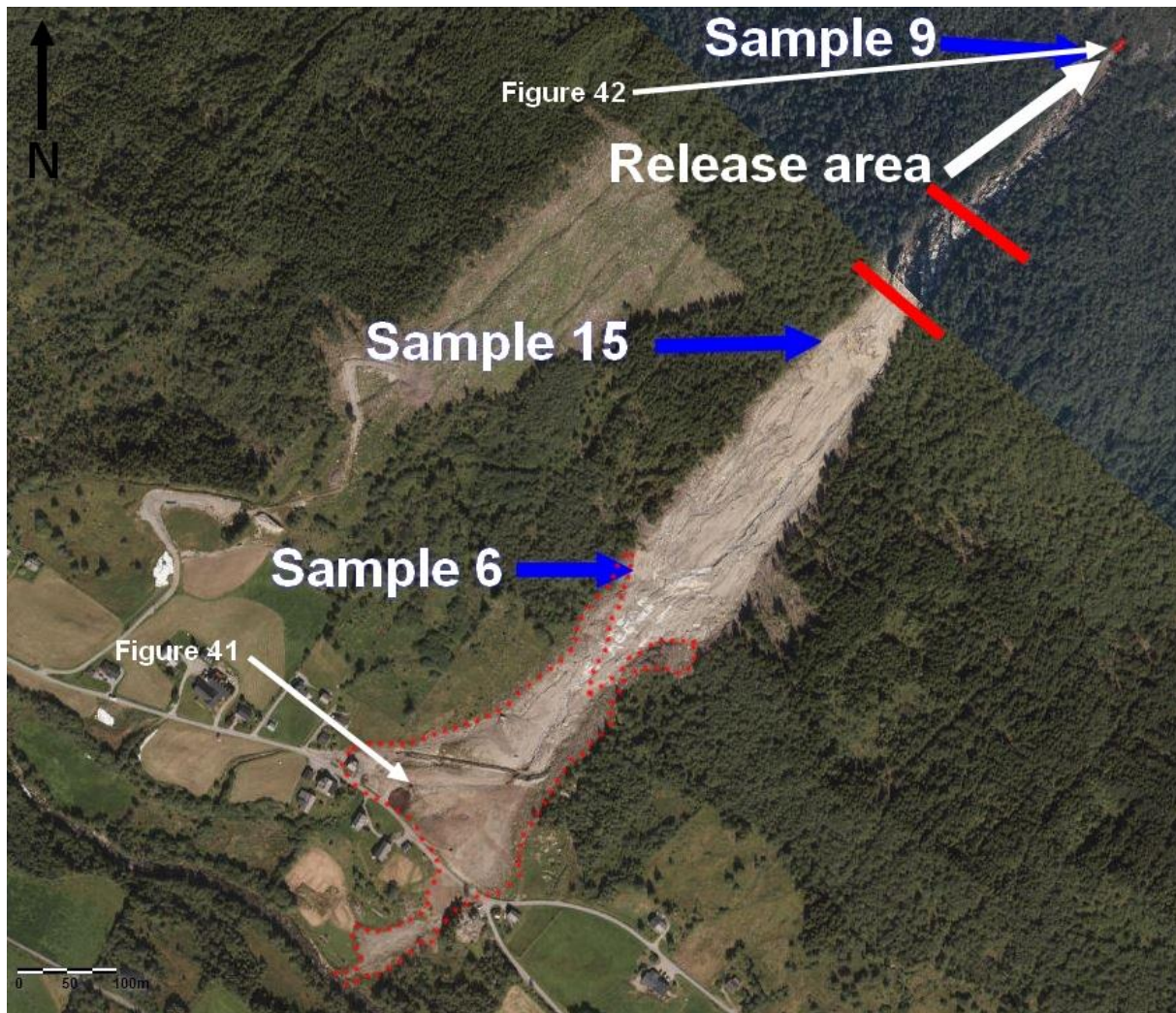
Figure 43: Overview of the Årset site. The segments of the transport zone are separated by red lines and the depositional area marked with punctuated lines. The scale on the bottom left is 100 m. Edited from Norge i bilder (2017), photography from 2014 (upper part) and 2015 (lower part).

The final segment is 450 m long and has a convex geometry, starting at a slope angle of 35 °. The segment widens gradually, as two channels have formed 80 m from the start of the segment towards the left and right margins. The left channel seems to originate from a through in the cliff above, while the right side channel stems from the right margin of the cliffs. Between these channels, five smaller channels are visible. The land owner claims these have eroded in the years after the landslide, and not as a part of the event (H. Aarseth, pers.comm., 2016). Pictures taken the day following the landslide show the two marginal channels present at that time, while the smaller channels are not yet well developed (Figure

44). Channels have probably been modified and/or created following the flooding and sliding in November 2015, and similar high water input events. The track is generally not deep, only eroding the top < 0.5 m layer, though the channels reach 2 m depth at the most.

Figure 44: Picture taken the day after the landslide. The border of the depositional area is marked in red (NRK, 2013).

The channels meet at the end of the lower segment, and the transport zone narrows down as deposition starts at the flanks. Trees have been leveled along the flanks, and in the lower left part (Figure 44), levees of trees can be observed. The slope in this area is 12 ° and the joining of the channels sees the width of the transport zone decrease. The transport zone terminates into the depositional area flanks first, followed by the centermost part. Polished bedrock is exposed in this area.

4.5.7   Area of deposition

News articles (NRK, 2013, Sunnmørsposten, 2013) provide pictures of the area taken less than 24 hours after the event (Figure 44), thus allowing for a higher level of detail when defining the depositional area. After initially depositing on the flanks of the transport zone, the masses spread as the slope approaches 10 °, reaching a width of 190 m. Along most of this width, the masses seem to have been limited longitudinally along the road, passing perpendicular to the flow direction. The exception is the left part, where masses are deposited as far as 150 m further, reaching the river in the bottom of the valley.

As the masses are reported to have settled significantly, the exact height of the deposits is not clear, though pictures taken the following day show masses reaching the first floor (second floor by Norwegian definition) of a house located on the southern side of the road (Sunnmørsposten, 2013). The land owner estimated the height of the depositional area to 4 m at the most, settling 2 m since then. Also, boulders of up to 7 ton had to be blasted with explosives as far down as the road (H. Aarseth, pers.comm., 2016). Figure 44 shows little elevation difference between the flanks of the depositional area and the surrounding surface, thus height will vary from virtually a few centimeters to several meters. The part of the lobe extending to the river has deposited around a power line mast. The mast has a sign marking what was previously 2 m above the ground, currently 32 cm above the surface. Thus, a max height in this area of 1.68 m is estimated, though the height before settling might have been considerably higher.

4.6 Kvam

The site designated Kvam is located in Veikledalen, approximately 2.5 km north of the village of Kvam, on an east facing slope. The upper margin of the upper release area is located at 218763E 6850648N at 669 m.a.sl. The landslide occurred on May 22. 2013. The total runout length (L) is 560 m, and the total elevation difference (H) is 278 m, giving a H/L ratio of 0.5 and a travel angle of 26 °. Initial volume was estimated to 663 m^3, and final volume, estimated through the flow path, to 12458 m^3. Numerous investigations and analysis into the events in the general area on 22. of May, their consequences and handling by the authorities have been done, including Olsen et al. (2015), Siedler (2013) and Direktoratet for samfunnssikkerhet og beredskap (2013).
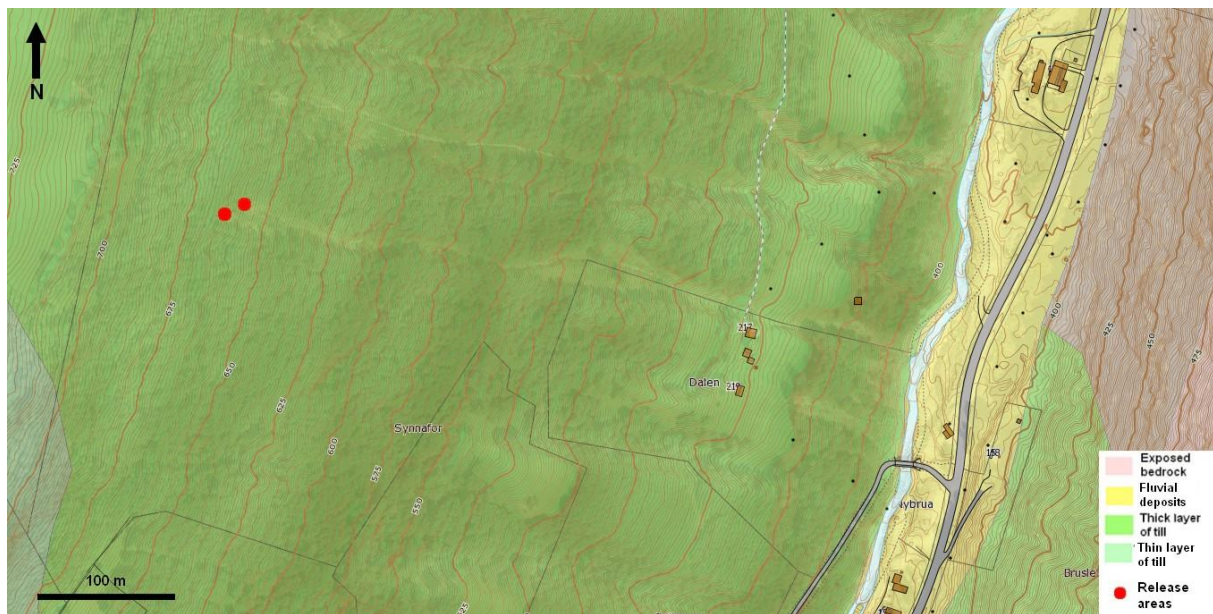
Figure 45: Sediment map with topography and inventory, superimposed on an aerial photography of Kvam. Landslide in soil is registered from 2011 (brown square), though it appeasr to refer to all landslides occuring on this slope in 2011. Another square further down valley (not in this picture) serves the same purpose for the 2013 events. Based on the NGU (2017b) geological maps, Norge i bilder (2017) and skrednett (2017).

4.6.1 Terrain

The slope in which the landslide has eroded is slightly convergent, with an average slope angle of 26 °. 110 m above the upper release area, there is an agricultural field, bordered in the north by a road. In the bottom of this field, larger rocks are assembled (Figure 46),

probably as the field above has been cleared and ploughed. Aerial photography from 2011 shows a smaller slide in this slope.

The slope ends in the valley floor where a river runs, and there is a road parallel to the river. In the lower part of the slope (450 m.a.sl.), there is an open field, and a small cabin. There are a large number of channels, from 50 m north of the landslide being surveyed and further northwards, several originating from the 2011 flooding. Aerial photography preceding the landslide shows a darker line, indicating less vegetation, along the path of the landslide, as far back as 2004.

4.6.2   Soil characteristics

The NGU geological maps (Figure 45) list the soil cover to consist of a continuous layer of till with high thickness in some areas (NGU, 2017b). This agrees well with field observations.

4.6.3   Bedrock

The NGU geological maps list the bedrock as phyllite and phylittic sandstone, with strike oriented north-west south-east and a north-east 20 ° dip (NGU, 2017a). During the field survey the bedrock was designated most probably phyllite. The bedrock is significantly fractured in some exposed areas, and these can be peeled in near horizontal sections. In general, the bedrock displays flat surfaces and sharp edges, presumably cut perpendicular to the layering of the rock. The flat top surface is oriented near horizontally.

4.6.4   Vegetation

The area surrounding the landslide is densely vegetated by birch, bushes and waist high grass. Trees reach heights of 10 m, and except for the fields mentioned in section 4.6.1, the density and height of the vegetation remain up the slope.

4.6.5   Release area

The Kvam site has two release areas, joining 75 m below the upper scarp of the uppermost (right) release area. The right, and uppermost, release area is 12 m wide and 1.5 m deep at most, while the left one is smaller with a maximum width of 9 m and a depth reaching 0.8 m. The right channel is located 10 m upslope of the left. Between the topmost release area and

the top of the other, a small (~30cm wide) channel is still visible, though overgrown. Though grass and moss is growing on much of the release area, bare patches and smaller scarps bear evidence of more recent activity. There is no exposed bedrock in this area. The average slope is 29 °. Separating the two release areas is a 2-4 m wide densely vegetated ridge, consisting of soil, present the first 50 m of the right release area. The release areas, and the ridge, were sampled.
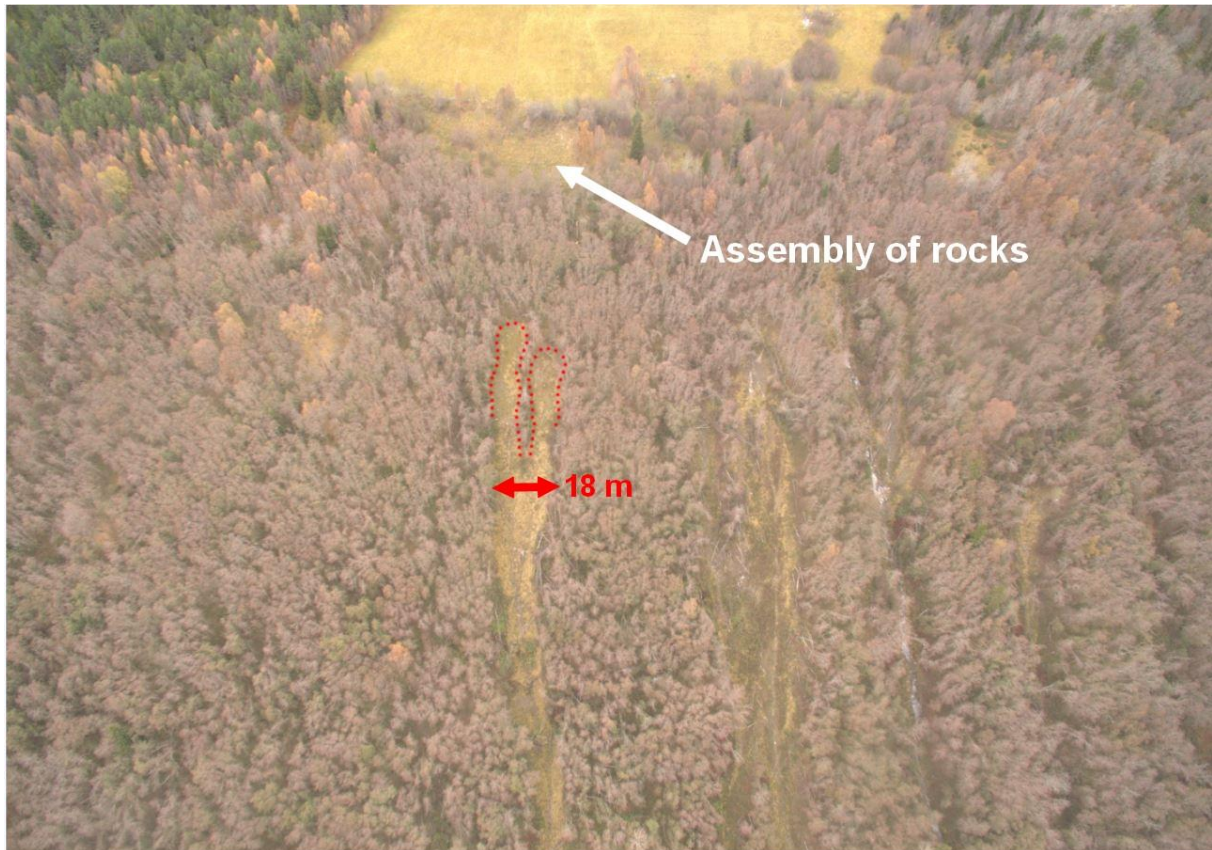
Figure 46: View of the release area of the Kvam site, looking up slope (west). Taken by Asgeir Olaf Kydland Lysdahl on October 17. 2016, using a drone.

4.6.6 Transport zone

Approximately 100 m below the uppermost release area, a more well defined channel has developed. This segment has an average slope of 29.5 °, and sees the channel exposing the bedrock at 615 m.a.sl. and several places throughout the segment. The channel reaches a maximum depth of 5 m, compared to the surface of the surrounding slope, and an upper width of 14 m at most. Still, the width of the deepest parts of the channel is rarely wider than 1 m. The middle of the channel is generally not vegetated and has water running through it, while the sides are mostly overgrown with grass and moss. Aerial photography from 2013 displays

a similar geometry (Norge i bilder, 2017). The channel has some sharp falls up to 3 m where bedrock is exposed, while other parts see the channel focusing as it is limited by bedrock on one or both sides. This segment sees bedrock topography as a dominating actor, both in directing the flow and by limiting bed erosion, thus increasing width.

The next segment starts 210 m from the top of the release area, and sees the transport zone opening, to a maximum width of 38 m. The main channel is redirected northwards, 14 m north of its original trajectory, around a ridge, joining the original trajectory in the bottom of the segment, 150 m below. This channel is up to 6 m wide, and 2 m deep. Similarly, a smaller channel is eroded on the opposite side of the ridge, its path closer aligned to the original trajectory of the channel. Also, the ridge itself has few trees left, and aerial photography from 2013 shows the ridge to have flattened vegetation and mud covering it. There is also an accumulation of coarser rocks on the stoss side. The slope in this segment is 29 °, similarly to that of the upper segment. The bedrock is exposed in the channel bed throughout this segment, and the lowest area of exposed bedrock is logged at 460 m.a.sl. during the GPS logging.
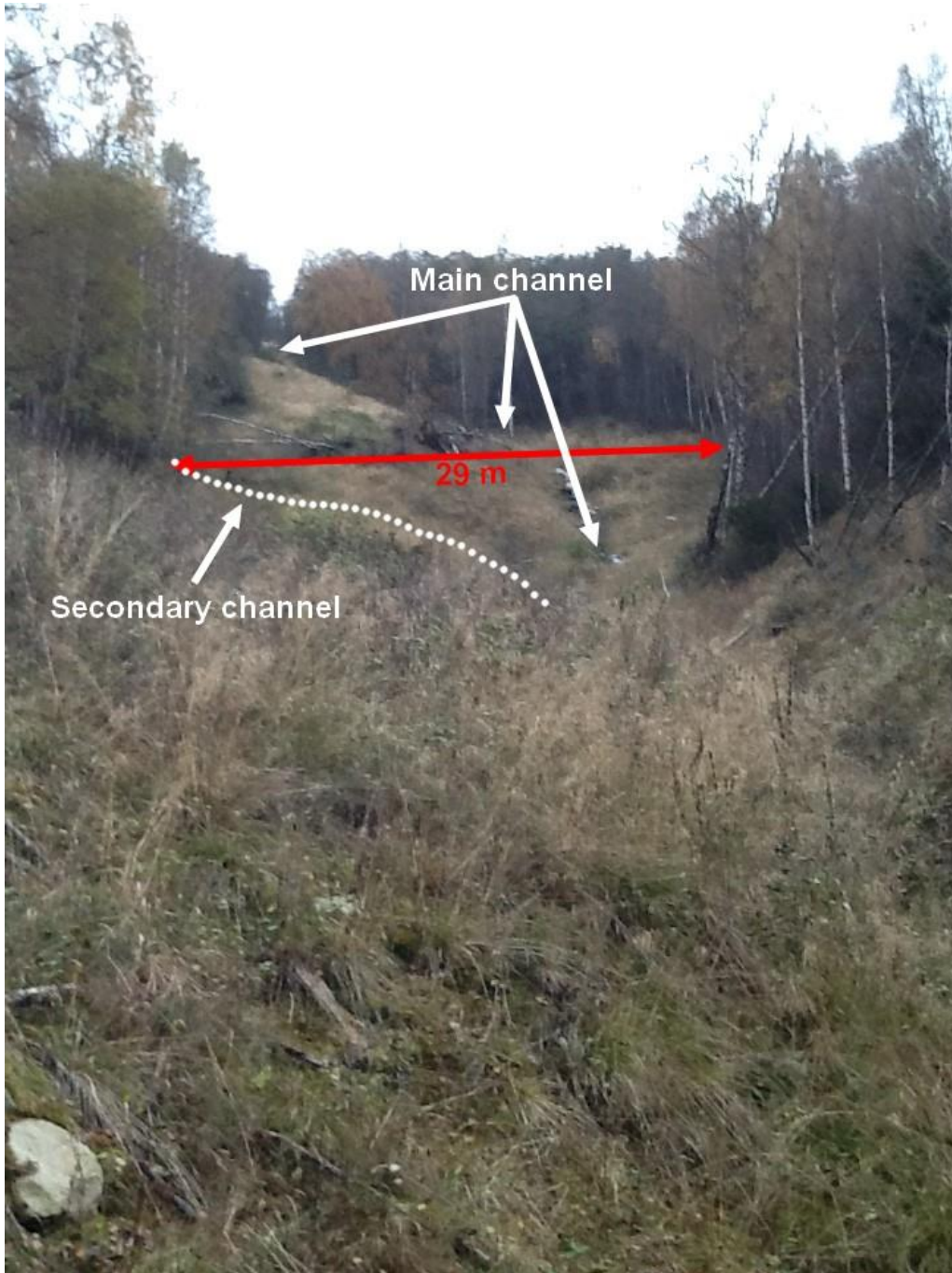
Figure 47: Picture taken from below the middle segment in which the channel runs around a ridge, looking up slope (west) at the Kvam site.

As the channels on both sides of the ridge join, the slope decreases, and the main channel decreases its width to 15 m and eventually 4 m. This segment is an open field with high grass, and some small cabins. The channel is 3 m at its deepest. On the right side, in the upper part of this segment, a 6 x 6 m cabin is left standing. The slope in this segment is 11 ° and the segment is 80 m long.

Figure 48: An overview of the Kvam site. Red lines mark the borders between segments of the transport zone. Modified from Norge i bilder (2017).

The last segment is 70 m long and leads to the river. Throughout it, there is a series of failures in the left side of the channel, expanding it from its width of 4 m to 15 m. The bottom half of the segment has a slope of 34 ° as the channel runs into the river. Aerial photography from 2013 shows the building of levees, especially on the left flank, covered and/or consisting of trees.

4.6.7 Area of deposition

The depositional area ends in the river. While a transitional zone, with building of levees, can be identified from aerial photography from 2013, most masses have probably been washed away or removed at the time the photography was taken.
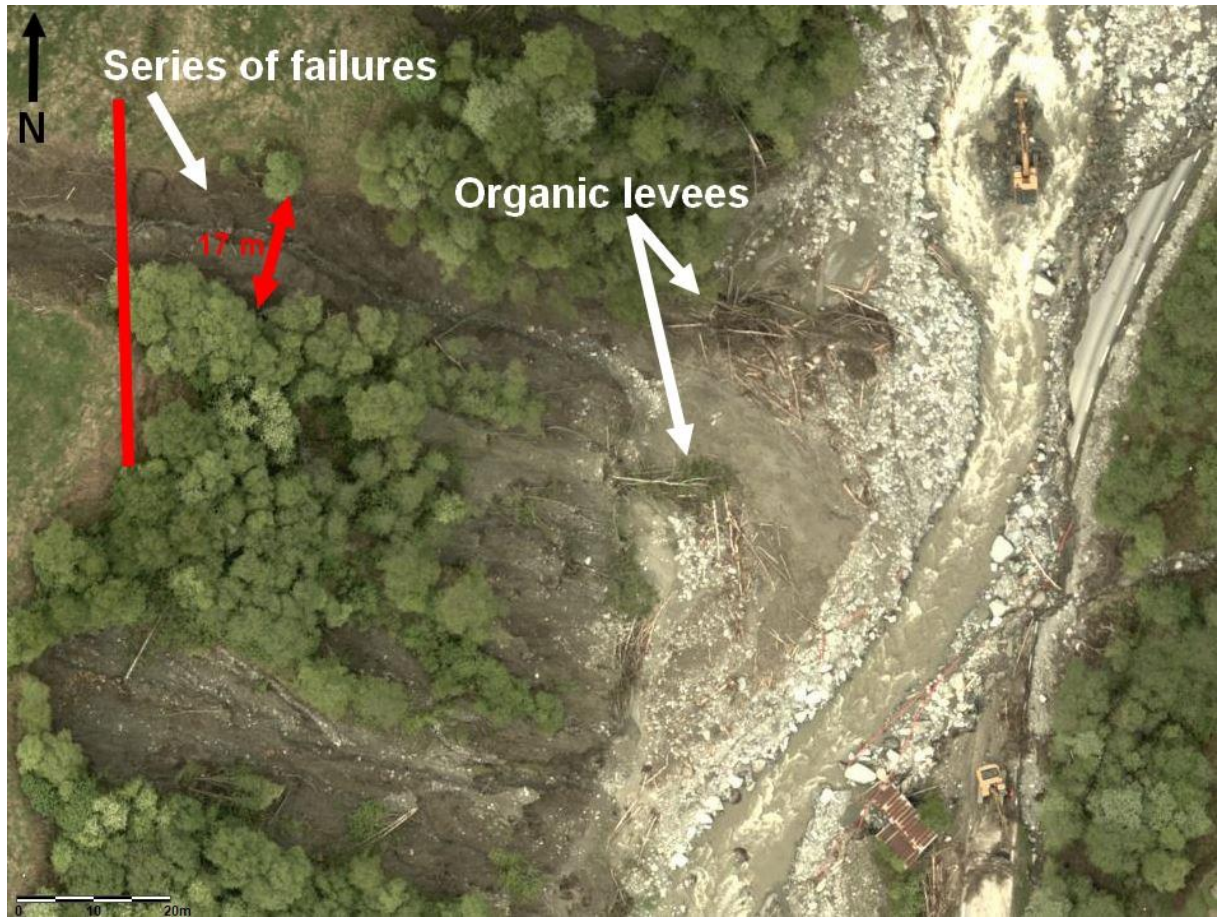
Figure 49: Last segment and depositional area of the Kvam site. Modified from Norge i bilder (2017).

5   Results

5.1   Grain size analysis

To make the sieving and Coulter data comparable, the cumulative values plotted correspond to the percentage of weight smaller than the corresponding grain size. Pictures of each sample, and where they were gathered, are found in Appendix 5, together with the grain size distribution data (Appendices 3 and 4).

5.1.1   Norangsdalen 1

Five samples from Norangsdalen were analyzed. As mentioned in section 4.3.2 the soil overlaying the slope was assumed to be landslide material, in accordance with the NGU (2017b) maps. Samples 4 and 7 were collected in late autumn (October), while the remaining samples were collected during summer (June). The location of each sample site is found in Figure 31.
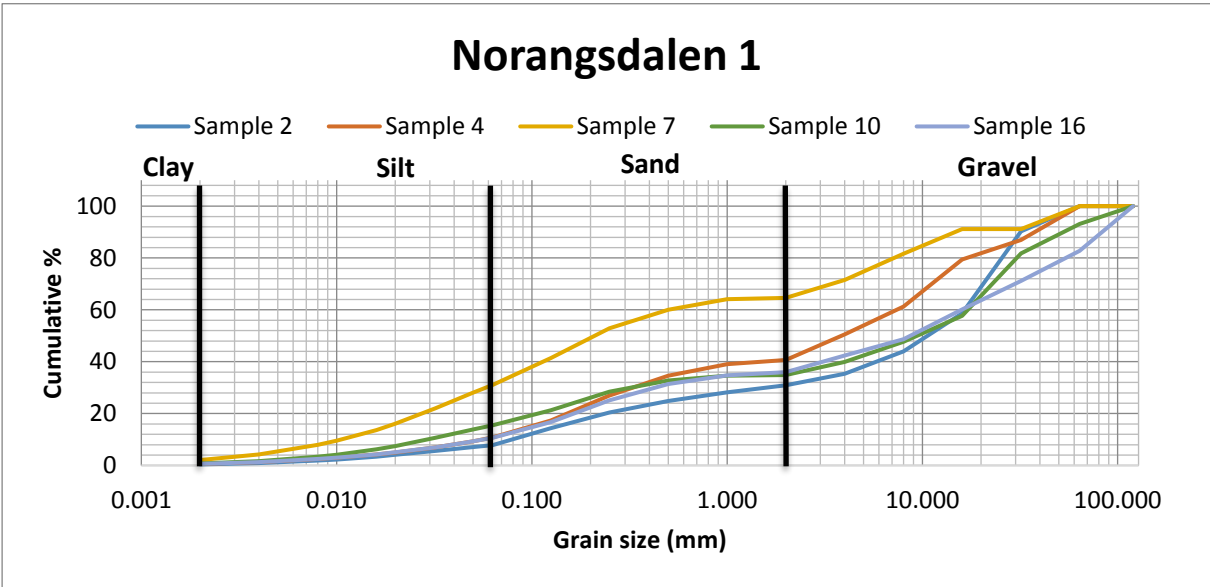
Figure 50: Cumulative grain size distribution of the samples gathered at Norangsdalen 1. Sample 16 was from the start of the channel. Sample 2 was collected 50 m from the start of the channel. Samples 4 and 7 were taken from what appeared to be two different layers in the channel wall half way down the channel. Sample 4 is the upper sample, while sample 7 is the bottom one. Sample 10 was collected 20 m upstream of the end of the channel. See Figure 31 for the location of each sample

site.

Most of sample 10 consists of clasts of gravel size, and to a lesser degree sand and silt. Thus, the sample is skewed towards larger grain sizes, and would still be so if the largest (>20 mm) clasts were removed from the dataset. The clay content was negligible. The distribution conforms well to the assumption that the soil covering the slope is landslide material. The coarser grains are generally angular.

Sample 4 is from the upper half (stratigraphically) of the channel. Its grain size distribution closely resembles that of sample 10, though displays a slightly lower content of silt, and more sand. Similarly to sample 10, gravel makes up the bulk of sample 4, though the gravel is finer, and there were fewer large (> 20 mm) clasts. Like in sample 10, the grains were angular. It was noted during the sampling that it had an organic smell.

Sample 7 is collected below (stratigraphically) sample 4. It was noted during the surveying that the layer in which sample 7 was collected appeared to have a lighter red color than the overlaying layer in which sample 4 was collected. The sample is evenly distributed, with grains up to and including silt making up more than 31 % of the sample, more than twice the amount of any of the other samples from this location. The grains seemed slightly less angular, than those of the layer above.

Sample 16 has a grain size distribution closely resembling that of sample 10. The difference is most profound in the largest grain sizes, where the error is assumed to be the largest. The grains are angular, like those of sample 10.

Sample 2 was collected in the middle (stratigraphically) of the channel, downstream from a dam. The grain size distribution is close to that of samples 10 and 16, though the content of silt is the lowest of all the samples from this location. Like the other samples, excluding sample 7, gravel makes up the bulk of the sample. The lowest mesh size during sieving was 0.063 mm, as opposed to 2 mm for the other samples, thus less of this sample was analyzed with the Coulter device.

Samples 2, 4, 10 and 16 have similar grain size distributions, and are dominated by gravel. The distribution of samples 10 and 16, collected at the start and end of the channel respectively, fit particularly well, indicating the same soil type to be present throughout the slope. The distribution fits that of landslide material, which is the soil cover registered in the

NGU geological maps (2017b). Sample 7 is more equally distributed and has a much larger content of fines than any of the other samples. It was sampled in a layer stratigraphically below the others, and was identified as differing from the others in the field. There are glacial deposits in the valley that might underlie the landslide deposits.

5.1.2 Norangsdalen 2

At Norangsdalen 2, four samples were collected. Samples 3, 8 and 12 were collected during the summer (June) while sample 1 was collected in autumn (October). Like at Norangsdalen 1, the soil cover of the slope is registered as landslide material (NGU, 2017b). Lower mesh size for sample 1 and 3 was 0.063 mm, and 2 mm for samples 8 and 12. The sample sites are displayed in Figure 37.

Figure 51: Cumulative grain size distribution of the samples gathered at Norangsdalen 2. The cumulative % is plotted as % below corresponding grain size. Samples 8 and 12 were collected on the depositional lobe, along the same profile. Sample 3 was collected at the top of the mid section of the transport zone, while sample 1 was collected in the release area. See Figure 37 for the location of each sample.

Samples 8 and 12, 8 being the upper of the two, have a very similar distribution. Sample 12 has a slightly higher content of silt and clay, while sample 8 contains more sand and gravel.

The samples have a high content of silt, and coarse gravel, while possessing little coarse sand and fine gravel. The grains appear sub-angular.

Sample 3 was collected on the right side of the channel. It consists 25 % silt, with less than 1 % clay. It is dominated by coarse silt and fine sand, while coarse sand and gravel are evenly distributed. The clay content of sample 3 is less than half that of sample 12. There was not much larger gravel in the channel side where the sample was extracted. The grain shape is angular to sub angular.

Sample 1 has a grain size distribution that fits the one of sample 3 nearly perfectly, and the differences are negligible. While rock fragments were abundant in the channel bed and release area, few were found in the side of the scarp, where the sample was extracted.

Samples 1 and 3 have an equal grain size distribution, dominated by coarse silt and fine sand and appears to originate from the same layer. Except for the material deposited by the landslide, similar soils seemed to be dominating throughout the slope. Samples 8 and 12 were deposited by the landslide, and are dominated by silt and coarse gravel. The grain size distribution fits what would be expected from landslide material, as designated in the geological maps. In the release area however, the thickness was lower than listed in the maps.

5.1.3 Årset

At Årset, 3 samples were collected. All samples were collected during the summer (June). A lower sieve diameter of 2 mm was used on all samples. The soil cover is listed as peat and humus in the release area and upper channel, and till through the rest of the transport zone (NGU, 2017b). The layer of peat and large rock fragments was not sampled. Figure 43 shows an overview of the sample sites.
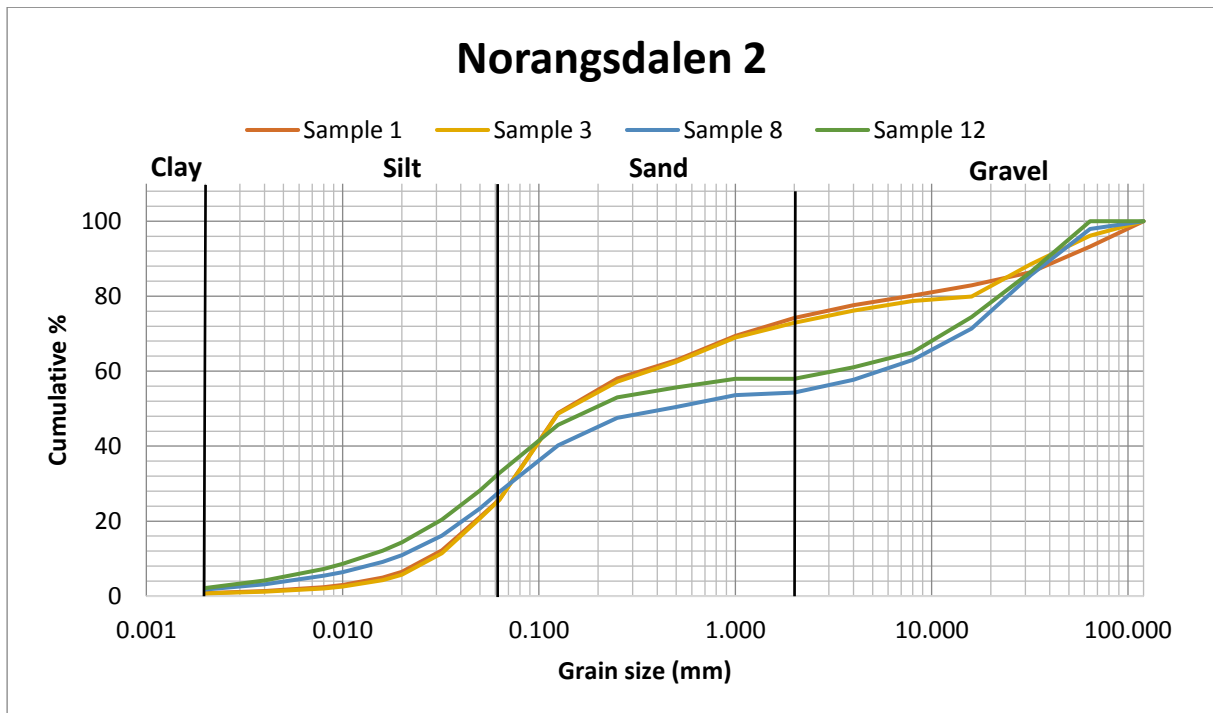
Figure 52: Cumulative grain size distribution of the samples gathered at Årset. The cumulative % is plotted as % below corresponding grain size. Sample 9 was collected at the release area, in the side of the failing layer. Sample 15 was collected in the side of a channel, midway through the transport zone. Sample 6 was collected in the coarse layer above the depositional area, assumed to be the same layer constituting the sliding plane upslope. See Figure 43 for location of each sample.

Though the area itself was riddled with gravel up to cobble size, sample 9 dug out from the side of the release area, contained fewer large clasts. The grain size is evenly distributed and contains more than 18 % silt and 1.4 % clay. Less than half the sample contains gravel, and clasts were angular.

Sample 15 has a grain size distribution equal to that of sample 9. It was collected in the channel side in what appears to be intact soil cover preceding the landslide. The grains appeared angular, though more rounded than those found in sample 9.

Sample 6 was collected in what is assumed to be intact soil cover preceding the landslide. It is assumed to represent the layer acting as a sliding plane through the release and transport zone. It contains less than half the amount of silt of samples 9 and 15, and only 0.5 % clay. It is dominated by gravel, making up more than half of the sample. The grains were sub angular.

Samples 9 and 15, while being collected 400 m apart in what is listed as different soils (peat and till), have an equal grain size distribution. Sample 6 is considerably coarser and has a

comparatively low clay content. This layer is assumed to represent the surface over which the landslide passed and to some degree eroded, and is designated as till in the geological maps.

5.1.4 Kvam

At Kvam, four samples were collected. All samples were sieved with a lower sieve size of 2 mm. The soil cover on the slope is listed as till on the NGU (2017b) geological maps.
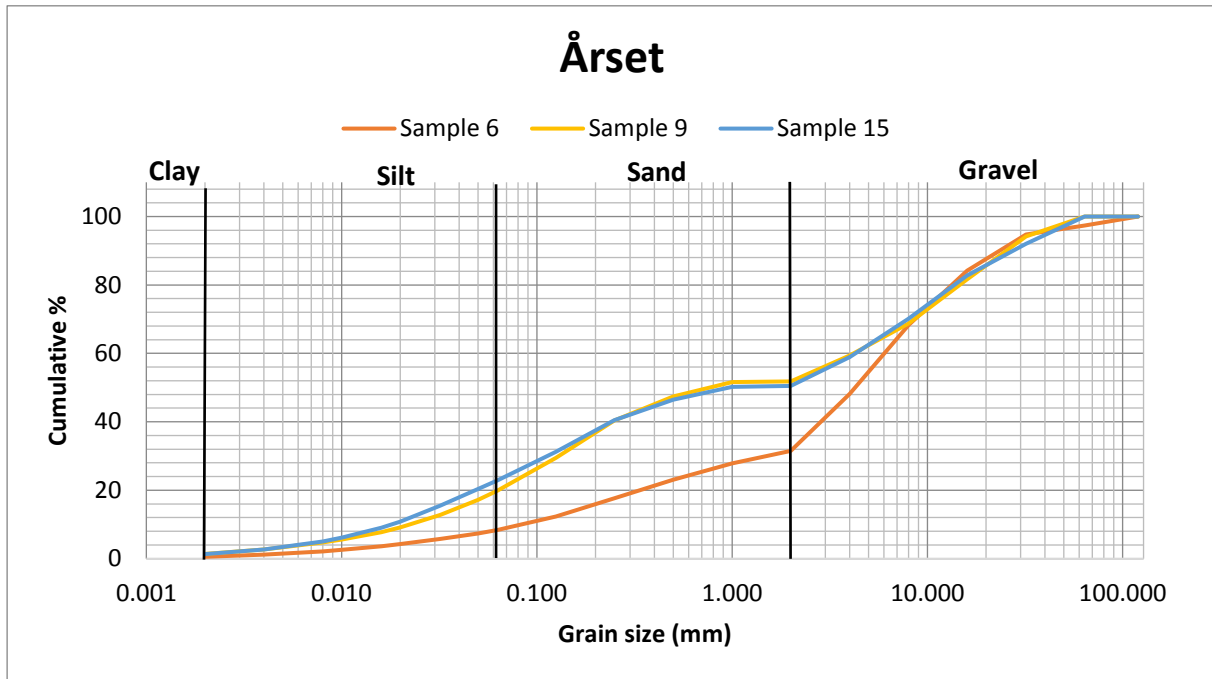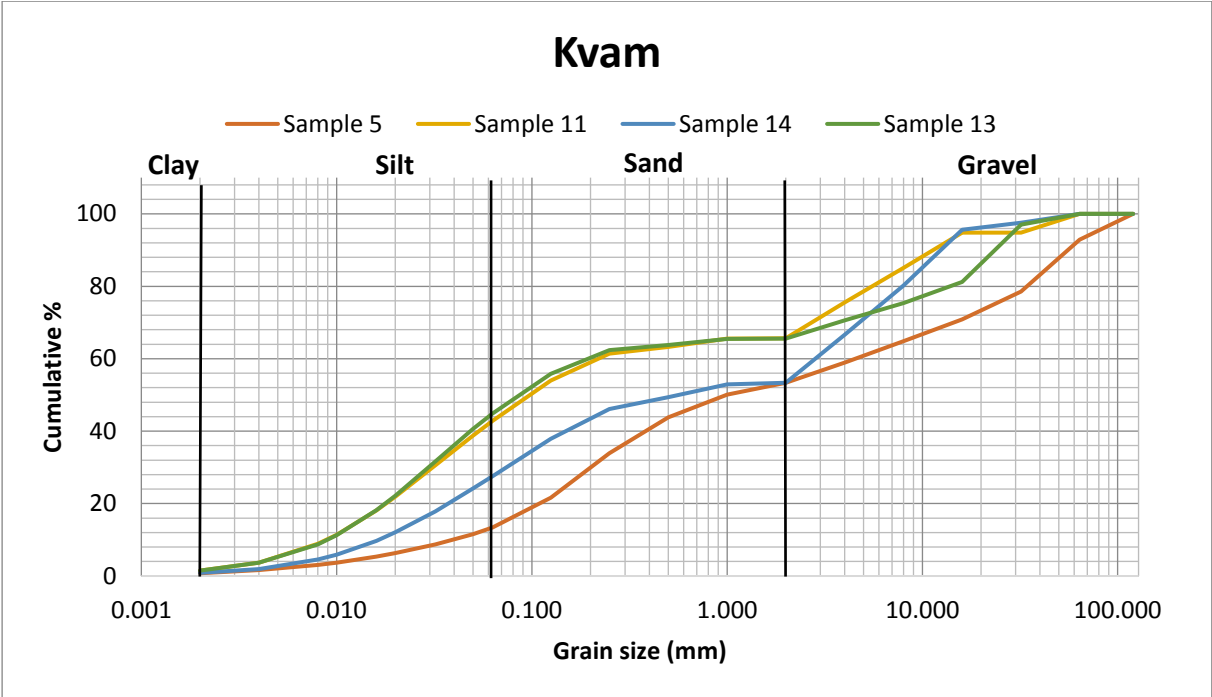

Figure 53: Cumulative grain size distribution of the samples gathered at Kvam. The cumulative % is plotted as % below corresponding grain size. At Kvam, samples 11 and 13 were collected in the scarp of the right and left release areas. Sample 5 was collected from the ridge separating the release areas, and sample 14 was collected in the lower part of the transport zone. See Figure 48 for location of each sample.

Sample 11 contains more than 40 % silt, and 1.5 % clay. The sample contains little sand, and has a significant amount of gravel up to pebble size. The grain shape was sub angular, though it was generally flatter than that found at the sites in Western Norway.

Sample 13 is in all aspects similar to sample 11, except for the gravel fraction, in which sample 13 is skewed towards coarser gravel. The clay content was found to be the exact same as that of sample 11. It was collected similarly to sample 11, though in the scarp located 10 m downslope and parallel to that of sample 11.

96

Sample 5 has the lowest content of clay and silt of the samples collected at Kvam. Gravel and sand dominates the sample equally, and the sand content is the largest of all samples from Kvam. The grain shape was similar to that of samples 11 and 13, though there were more large clasts in sample 5, and the cut from which it was extracted.

The content of clay and silt of sample 14 is intermediate between that of samples 11 and 13, and sample 5. Sample 14 contains an equal amount of gravel to sample 5, though skewed towards the finest fractions. The area where sample 14 was collected displayed a higher number of large (> 64 mm) well rounded clasts than did any of the other sample sites. These were not sampled.

Samples 11 and 13, collected in the release areas, have a very similar distribution. The ridge separating the two release areas (sample 5) has a distinctly coarser grain size distribution, with low content of clay and silt, and high content of sand. Sample 14, gathered in the lower transport zone, shows a grain size distribution intermediate of the other samples. This area had a higher number of larger, rounder, clasts.

5.2 Geophysical methods

The field west of the release area of the Kvam site is the only area where both geophysical methods (GPR and ERT) and both radar antennas were used. Also, the acquisition in this area was the most practical, with regards to the terrain. For this reason, this is the area used for calibration of depth and interpretations.
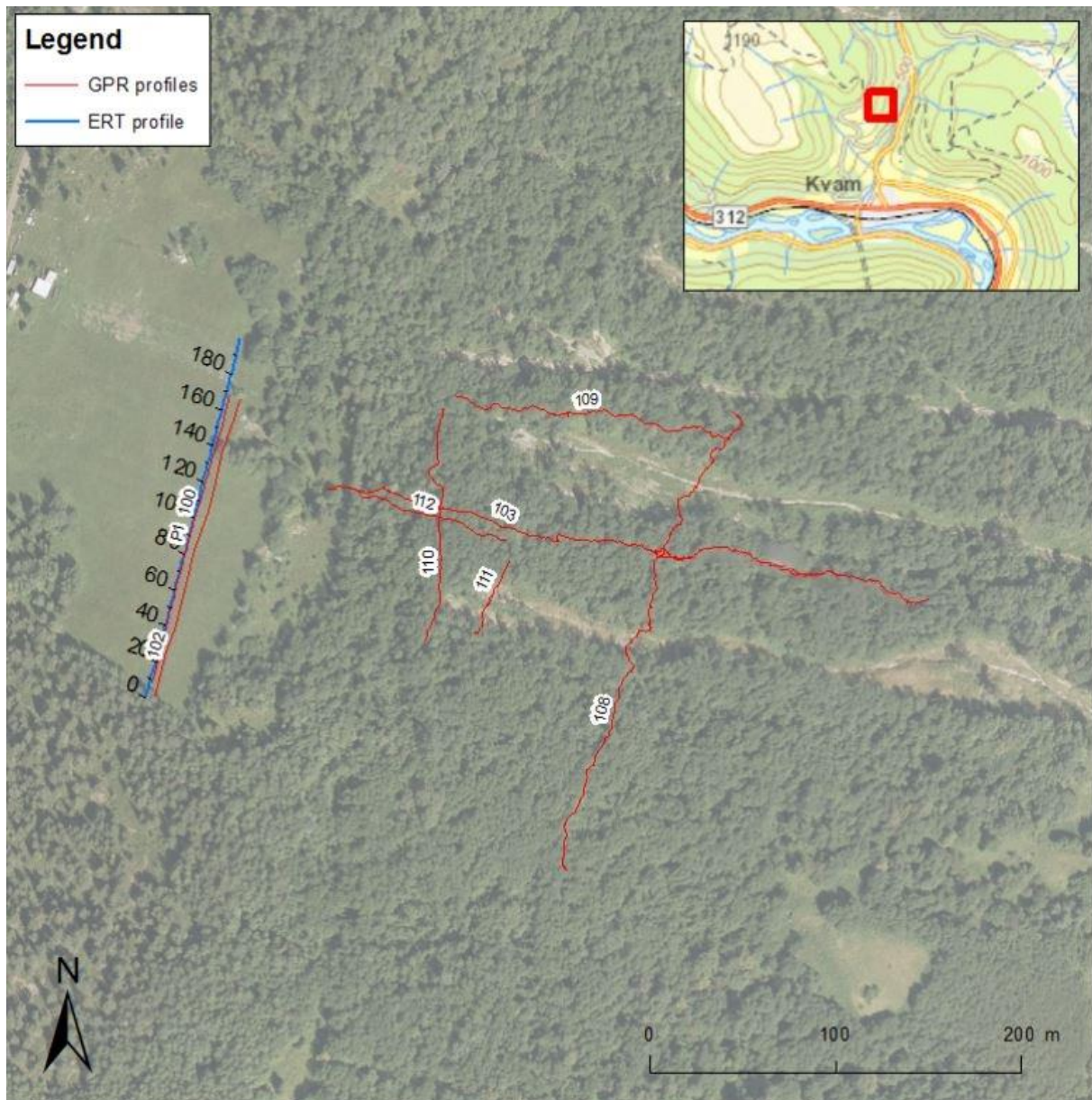
Figure 54: Airborne photography with GPS tracks of the profiles along GPR and ERT surveys were done (Anschütz et al., 2017). Profile 202 is aquired along the same line as the ERT profile, and profile 113 is aquired along the 56 m southernmost interval of profile 102.

GPR profiles 102 (Figure 55) and 100, going along the same line, both show a distinct horisontal reflector at 2-3 m depth, dipping in the northern 60 meters. Profiles 202 and 113

also show a similair dipping reflector along the southern part of the profile, while still displaying a horisontal reflector over the same area as profiles 100 and 102. In profile 202 the signal is varying below 2 m, though the same dipping features visible in the other profiles can still be observed. Profiles 100, 102 and 113 display a new horisontal feature at about 25 m depth.

The ERT data (Figure 56) displays a distinct high resistivity layer in the top 2-3 m along the profile, with low resistivity features dominating the surface and sub surface in the northernmost part, and the subsurface in the southernmost.
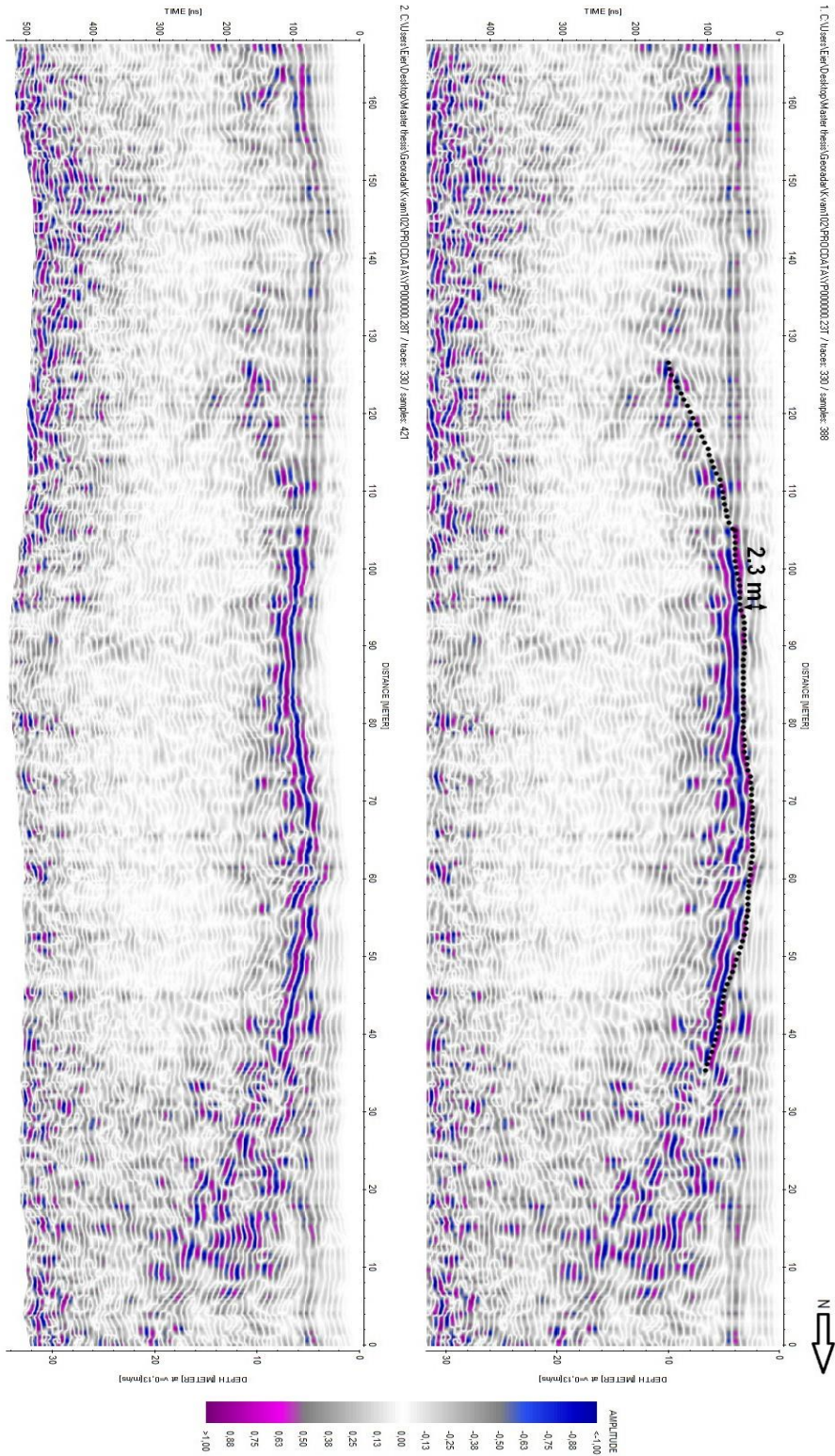
Figure 55: GPR profile 102. A reflector, at 2-3 m depth, is particularly well defined in the centremost areas, and the dipping features to the north and south agree well with those observed in ERT and IP plots. In the lower plot, topography corrections have been applied. Dashed line indicates the most easily identifiable interface.
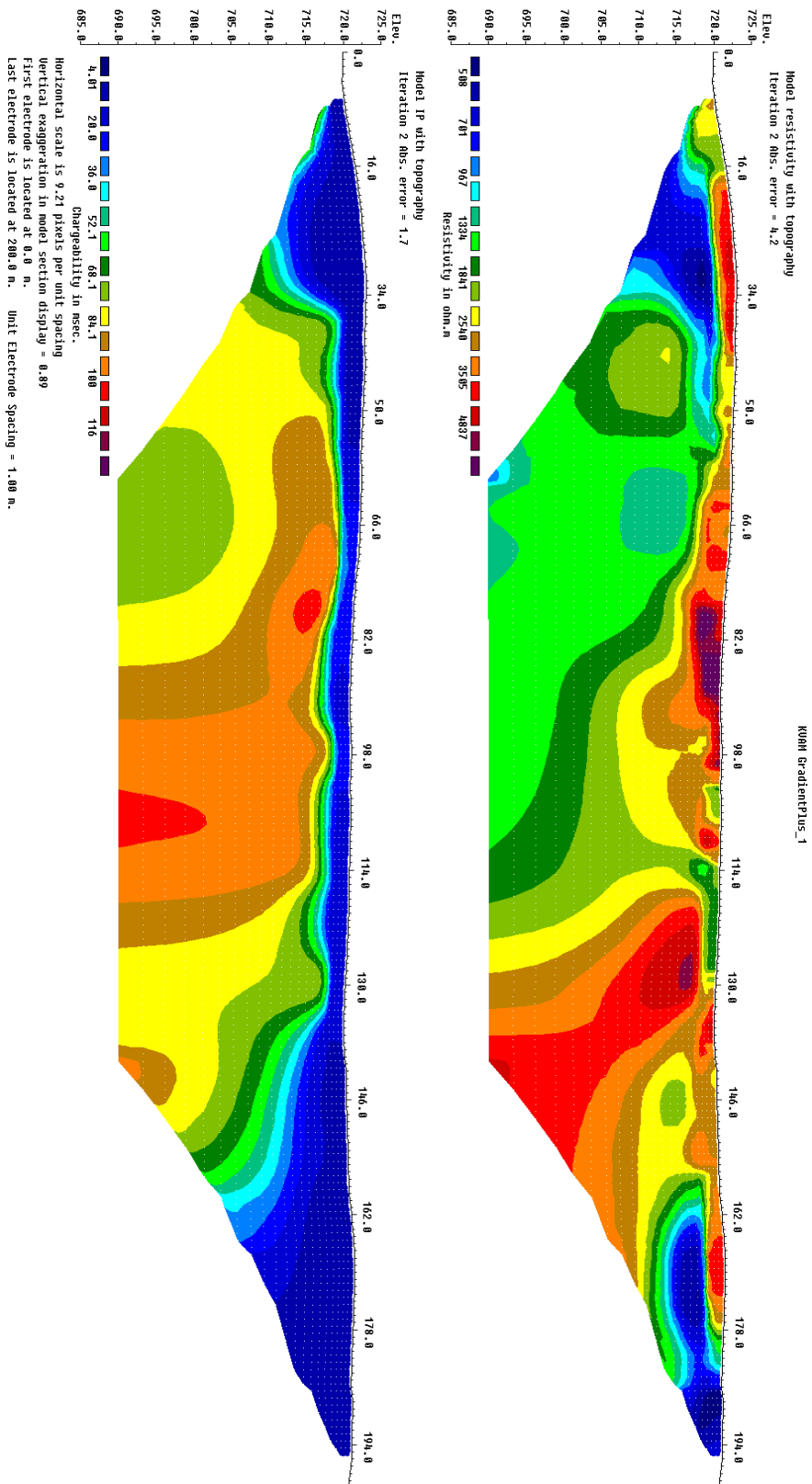
Figure 56: The IP (lower) plot shows a distinct interface in the 2-3 topmost meters, while ERT shows similair, though less clear, interfaces in the same area. Low resistivity segments are clearly visible in both ends of the profile.

The IP (Figure 56) data has a low chargeability layer in the top 2-3 m of the profile, increasing in depth in the southernmost 40 m and 70 m northernmost, reaching a depth of 15 m at its deepest.

The geophysical data from the field west of the release area consistently shows a horisontal feature at 2-3 m depth, dipping in the northern and southernmost parts.

Profiles 103 (Figure 57), 109 and 112 are acquired in the areas between landslide paths (Figure 54), with profile 112 covering parts of profile 103. The plots do show surface/near surface reflections, though there are also consistent reflections 5-12 m below the surface throughout all three plots. Profile 103 sees this reflector all but pierce the surface at 180 m profile length. Parallell to this area, the bedrock was observed to be at shallow depth in the channel. When correcting for topography, the subsurface structures seem to be at a low angle to the horisontal plane.
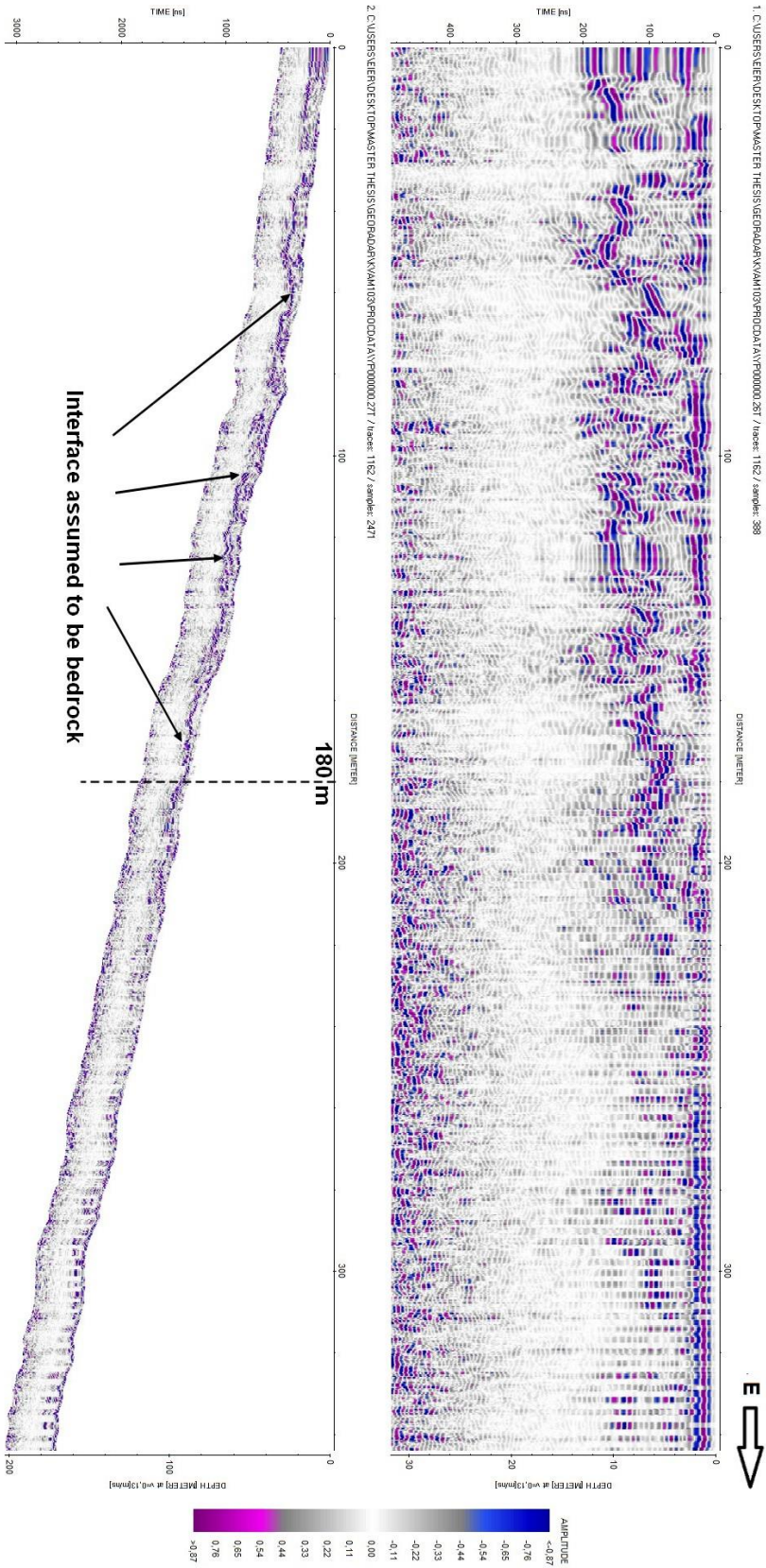
Figure 57: Profile 103. A reflector is clearly visible at around 10 meters below the surface, approaching the surface at 180 m.

Profiles 108, 111 and 112 are acquired perpendicular to the flow direction of the landslides (Figure 54), with profile 108 crossing two flowpaths, profile 111 crossing the release area of the Kvam site flow path, and profile 112 above the release area of the Kvam site and the neighboring release area. Profiles 110 and 108 show a reoccuring interface at depths of 4-10 m, and a second interface at approximately 25 m depth. Profile 110 also displays a greater depth to the interface directly above the release area of the landslide being surveyed.

In profile 111 there is an interface at 4-6 m depth, though no interface below the surface is visible in the parts crossing the release areas.
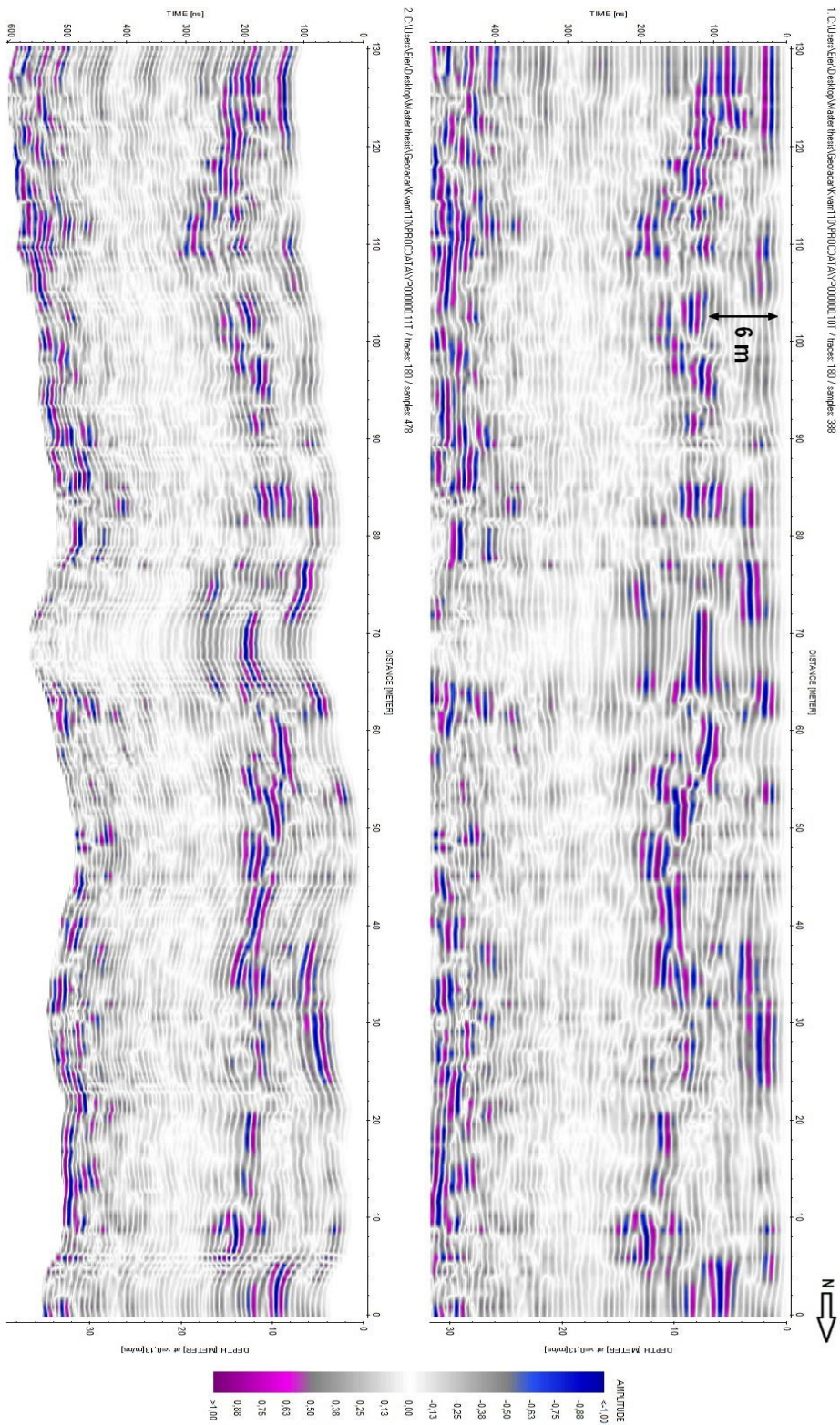
Figure 58: GPR profile 110, acquired few meters above the release area of the landslide being surveyed. Note the increased depth to interface at 110 m.

5.3 Runout simulations

This section lists the input parameters (friction coefficient (μ) and turbulence coefficient(ξ)) and the output parameters to which they were tuned (runout length and final volume). Note that of the latter two, final volume is the parameter with the largest uncertainty. In addition, maximum flow velocity is listed. A .txt file for each simulation with the input parameters and the output produced by DAN3D is found in Appendix 2. The flow path of all the simulations followed those observed in the field.

Table 7: The rheological parameters initially used in the runout simulations. Simulations 5 and 6 use the same friction coefficient as simulation 1.

Simulation	1	2	3	4	1 to 4	5	6
Parameter	μ	μ	μ	μ	ξ (m/s^2)	ξ (m/s^2)	ξ (m/s^2)
Norangsdalen-2	0.338	0.308	0.278	0.368	1000	500	1500
Årset	0.277	0.247	0.217	0.307	1000	500	1500
Kvam	0.329	0.299	0.269	0.359	1000	500	1500

The DEM used at Norangsdalen 2 is derived from merging a DEM interpolated from GPS-data collected after the event, and the contour FKB data. In the case of the latter, the upper contours preceded the event by more than five decades, while the lower parts were collected in 2015. At Årset, the DEM is based on data acquired after the event, while the DEM at Kvam is based on data preceding the event.

5.3.1 Norangsdalen 2

The percentage of deviation from the observations by each simulation is listed in Table 8. After the initial six simulations, a simulation with a turbulence coefficient intermediate to that of simulations 1 and 5 was chosen as the runout length of these runs displayed a good fit, while the volume varied. Simulation 5 produced very fractioned deposits. Thus, simulation 7 was run with $\mu = 0.338$, like in simulation 1 and 5, and $\xi = 700$ m/s^2. Maximum erosion depth was set to 2 m during all simulation runs.

Table 8: The percentage of difference in volume and length of the simulations to the observations at Norangsdalen 2. Maximum velocity of the run is also listed.

	Results	Diff volume (%)	Diff runout length (%)	Max velocity (m/s)
Norangsdalen-2	1 (μ=0.338, ξ=1000)	53.5	0.7	9.8
	2 (μ=0.308, ξ=1000)	82.9	1.9	10.2
	3 (μ=0.278, ξ=1000)	120.5	3.4	10.7
	4 (μ=0.368, ξ=1000)	25.7	-3.0	8.9
	5 (μ=0.338, ξ=500)	-3.9	-1.0	19.0
	6 (μ=0.338, ξ=1500)	74.4	0.7	10.7
	7 (μ=0.338, ξ=700)	41.5	0.7	12.6

All simulations reproduce a runout length differing less than 4 % from the observed length, and runs 1, 5, 6 and 7 lie within 1 %. All simulations, except simulation 5, returned larger volumes than estimated from field observations, though simulation 5 produced an irregular and fractured depositional area that does not conform to field observation, nor appear realistic. This simulation also produced the highest velocity. Final volume is observed to increase with decreasing frictional coefficient, and with increasing turbulence coefficient. The low turbulence coefficient in simulation 5 sees the velocity nearly double from that of simulation 1. The remaining simulations all had shapes closely resembling that of the field observations. Simulation 4, with $\mu = 0.368$ and $\xi = 1000$ m/s^2 appears to be the best fit.

Figure 59: The final depositional grid map of simulation 4, superimposed over an aerial photography of the study area (Norge i bilder, 2017). Note the deposition along the area observed to have levees. Deposition height color scale in meters.

5.3.2 Årset

The percentage of deviation from the observations by each simulation is listed in Table 9. In addition to the input parameters listed in Table 7, a seventh simulation (7) with $\mu = 0{,}15$ and ξ = 1000 m/s² was run. Maximum erosion depth was set to 2 m during all simulation runs.

Table 9: The percentage of difference in volume and length of the simulations to the observations at Årset. Maximum velocity of the run is also listed.

	Results	Diff volume (%)	Diff runout length (%)	Max velocity (m/s)
Årset	1 (μ=0.277, ξ=1000)	-29.8	-21.9	14.2
	2 (μ=0.247, ξ=1000)	-11.9	-20.9	15.7
	3 (μ=0.217, ξ=1000)	11.2	-19.3	16.4
	4 (μ=0.307, ξ=1000)	-44.9	-18.8	14.1
	5 (μ=0.277, ξ=500)	-34.6	-23.5	9.4
	6 (μ=0.277, ξ=1500)	-27.3	-23.1	16.7
	7 (μ=0.15, ξ=1000)	51.0	-12.1	17.0

All simulations, except simulation 7, are within 45 % of the estimated volume, though they produce considerably shorter runout lengths. They fail to reproduce a depositional geometry resembling that observed in the field. Simulation 7 was run because of these inabilities. While this run produces a final volume 51 % larger than estimated, it reproduces the geometry of the depositional area well, except for the sliver running down to the river. It is however apparent that the model behavior is affected by the modifications on the terrain done after the landslide. Simulation 7, with friction coefficient less than half of that initially estimated, does appear to be the simulation with the best fit.
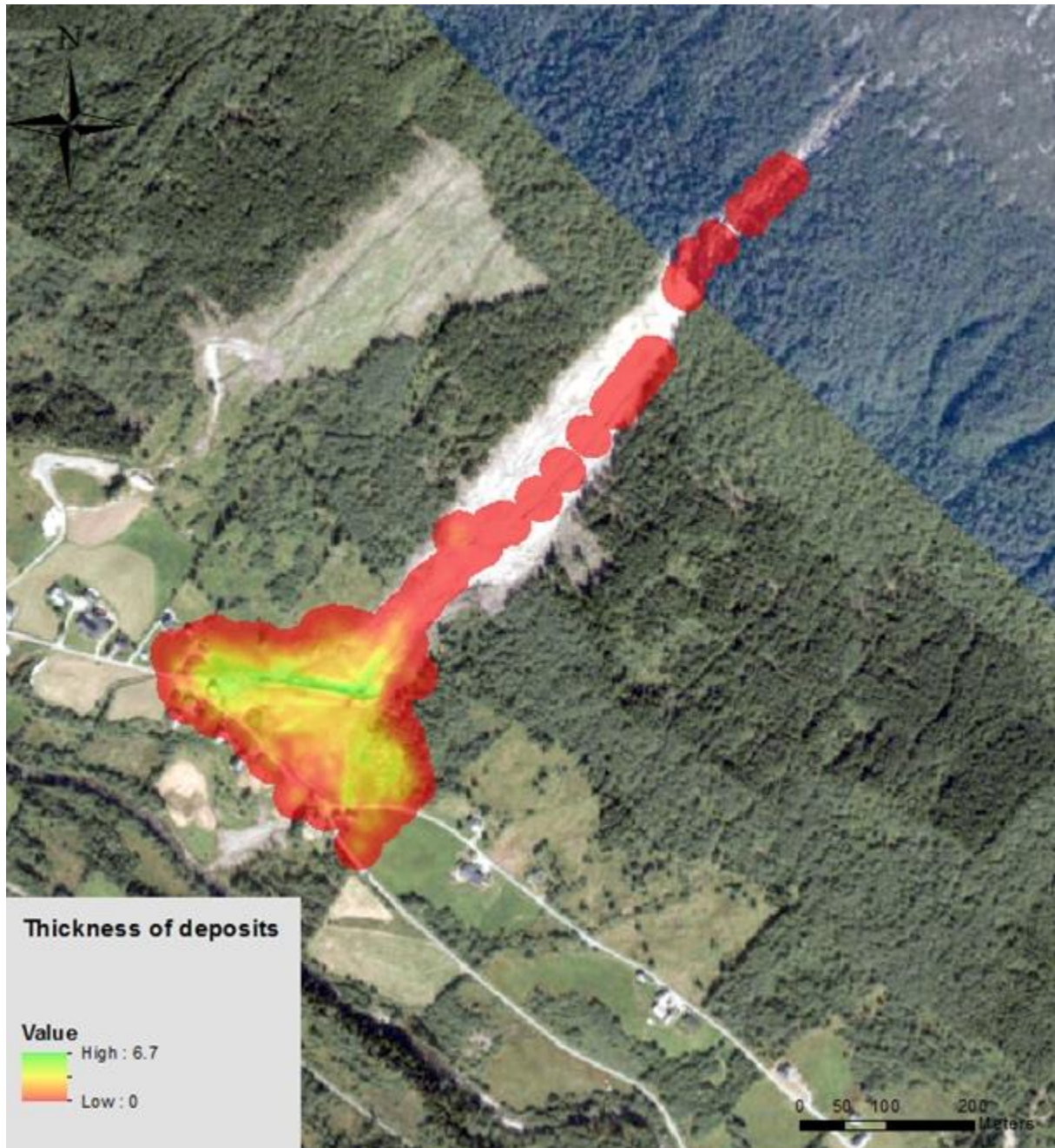
Figure 60: The final depositional grid map of simulation 7, superimposed on an aerial photography of the Årset site (Norge i bilder, 2017). The depositional area generally fits the field observations well, though the canal in the upper part has been artificially made and thus affects the results. Deposits color scale in meters.

5.3.3 Kvam

At Kvam, the final volume has only been estimated from the channel, and is thus more uncertain than at the other sites. Runout length is however limited naturally by the river, and allows less overestimation. This is the only site where geophysical methods were used, and provided the parameter maximum erosion depth, at 5 m, based on the maximum depth to bedrock.

Table 10: The percentage of difference in volume and length of the simulations to the observations at Kvam. Macimum velocity of the run is also listed.

	Results	Diff volume (%)	Diff runout length (%)	Max velocity (m/s)
Kvam	1 (μ=0.329, ξ=1000)	29.6	-0.4	15.7
	2 (μ=0.299, ξ=1000)	46.0	0.4	21.9
	3 (μ=0.269, ξ=1000)	59.9	1.8	20.1
	4 (μ=0.359, ξ=1000)	11.5	-0.5	13.6
	5 (μ=0.329, ξ=500)	20.5	-0.5	12.6
	6 (μ=0.329, ξ=1500)	34.9	-0.5	17.3

All models produce reasonable runout lengths and geometries, with some deposition occurring on the lower transport zone where slope angle is low. Final volume increases with decreasing friction coefficient, and increasing the turbulence coefficient sees the maximum velocity respond accordingly. Compared to earlier simulations with 2 m erosion depth at the same site, the volume increases approximately 20 %.
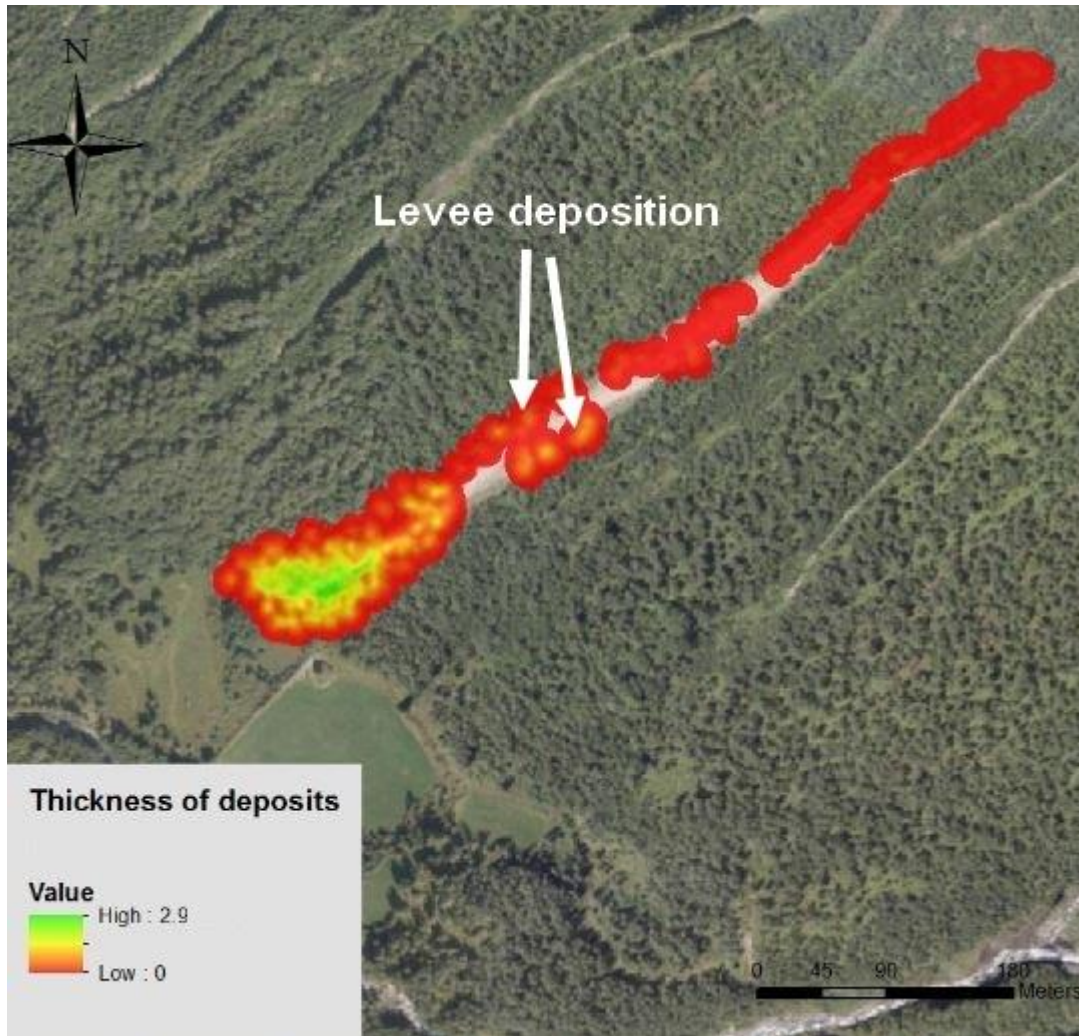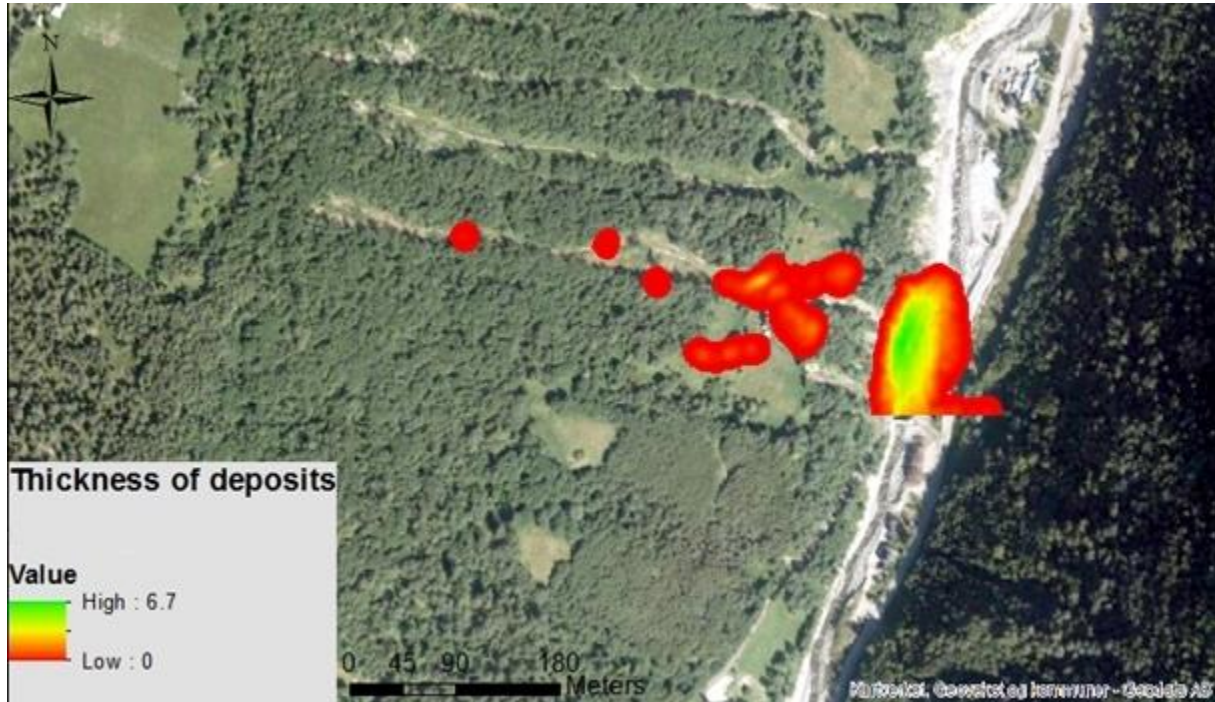
Figure 61: Final depositional grid map of simulation 3, superimposed on an aerial photography of the Kvam site (Norge i bilder, 2017). Depositional height scale in meter.

5.4 Weather at the selected sites

As the date of the landslide is known at Årset and Kvam, climate data is extracted and analyzed for these two sites. The findings from Årset will be taken into account when discussing the mechanisms involved in the two landslides in Norangsdalen, less than 40 km south-east.

Based on mean annual precipitation from www.senorge.no (2017), and equation 2.7 (section 2.6.4), the following critical water supply thresholds were calculated in accordance with Sandersen et al. (1996):

Table 11: Critical water supply within intervals of 12, 24, 48 and 72 hours for the Årset and Kvam sites. Mean annual precipitation is based on the gridded values in the release area of each site.

		Critical water supply (mm)		Mean annual precipitation (mm)	
Hours	Percentage critical	Årset	Kvam	Årset	Kvam
12	5.33	213.18	39.97	>4000	>750
24	8.08	323.12	60.59		
48	12.24	489.76	91.83		
72	15.62	624.66	117.12		

These thresholds are compared to gridded mean daily precipitation data from the sites, and hourly precipitation from the nearest station where such data is available. Thresholds for shorter timespans were not calculated, as the formula by Sandersen et al. (1996) are based on few observations below 12 hour. Mean annual precipitation at Norangsdalen 1 and 2 is estimated to 2000-3000 mm/year and 3000-4000 mm/year respectively. The data is acquired at www.senorge.no (2017).

5.4.1 Årset

The landslide in Årset occurred on November 15. 2013 at about 23:30. Gridded precipitation at Årset November 15. is 74 mm (Senorge, 2017). Increasing the time frame increases the gap between critical water supply and estimated values. Thus, the estimated daily precipitation at the site is close to one third of that needed to breach the threshold (Table 11). At nearby Ørsta-Volda airport the precipitation is listed as 99 mm during the same time period. In this area the gridded mean annual precipitation is minimum 2000 mm, giving a 24 hour critical water supply of 161.6 mm. Here too, the gap between critical water supply and observed values increases when expanding the time frame.

The closest station logging hourly precipitation is Emblem (Figure 13), 22 km east north-east of the Årset site, at 1 m.a.sl. The site registers an intense 12 hour period from 12 pm with a total precipitation of 86 mm, with small amounts of precipitation the preceding 12 hours.
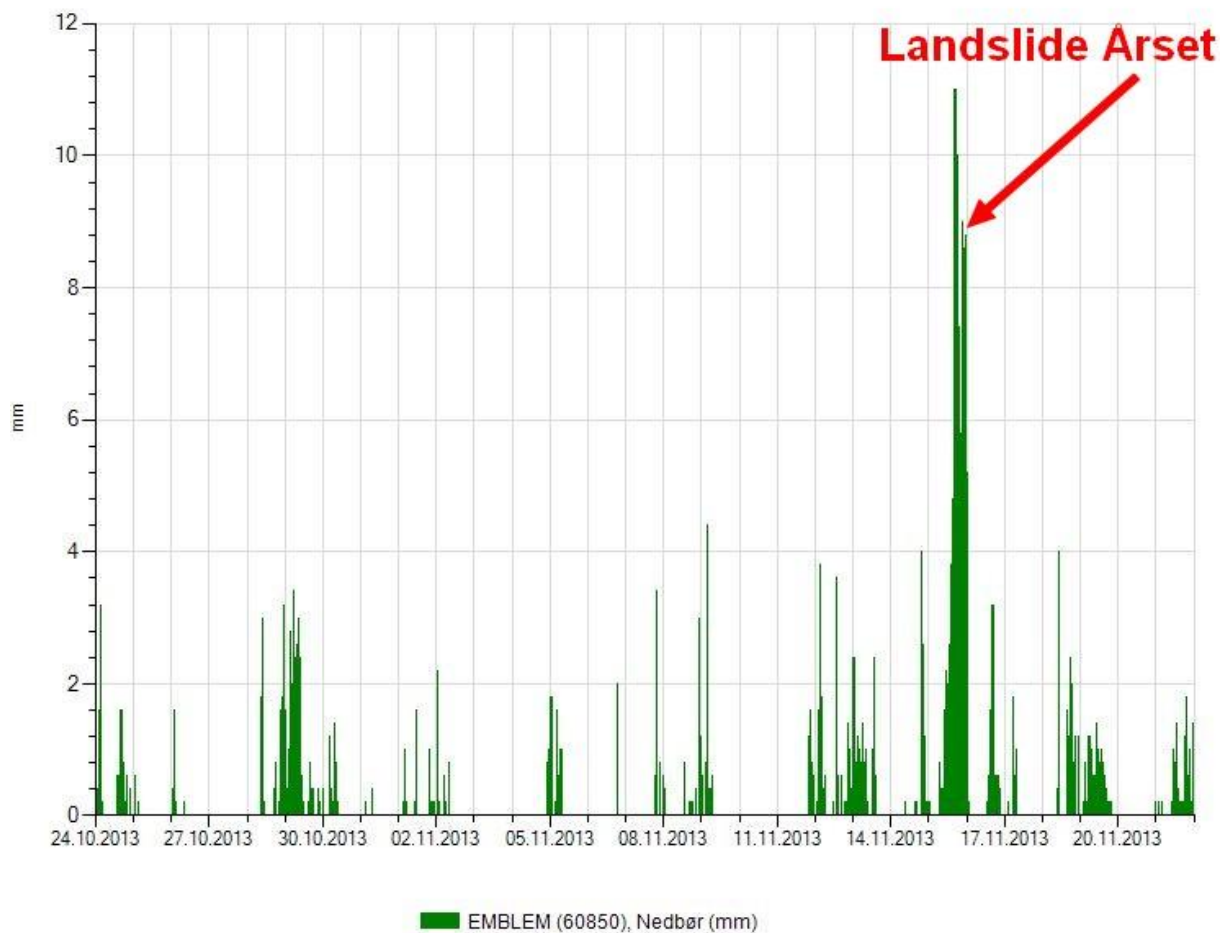
Figure 62: Hourly precipitation at Emblem station, 22 km from Årset (Senorge, 2017).

This weather station is located in an area with gridded mean annual precipitation of minimum 2000 mm (critical 12 hour water supply 107 mm), and at sea level. November 14. and 15. of 2013 saw heavy snow melting of 4 mm and 6 mm respectively around the mountain above the slope. Shortening the time span produces higher intensities.

At Hareid, 13 km north-west, winds up to 9 m/s were registered around the time of the event. The station is located at 130 m.a.sl.

The flood, landslide and snow avalanche site www.varsom.no (2017) lists the risk of landslides on the November 15. 2013 as yellow (2) on a scale from green (1) to red (4). The likelihood of a landslide occurring was thus assessed to be moderate.

114

5.4.2 Kvam

The landslide at Kvam occured in 2013, during the flooding on May 22. Gridded 24 hour precipitation on May 22. is 52.5 mm. Looking at the hourly precipitation from Skåbu station (Figure 63), 22 km south-west at 928 m.a.sl (Figure 14). a 24 hour precipitation of 47.3 mm and a 12 h precipitation of 27.6 mm are found (Senorge, 2017). This station has an equal gridded mean annual precipitation as the landslide site. Expanding the hours or days of either dataset increases the gap between the threshold and precipitation.
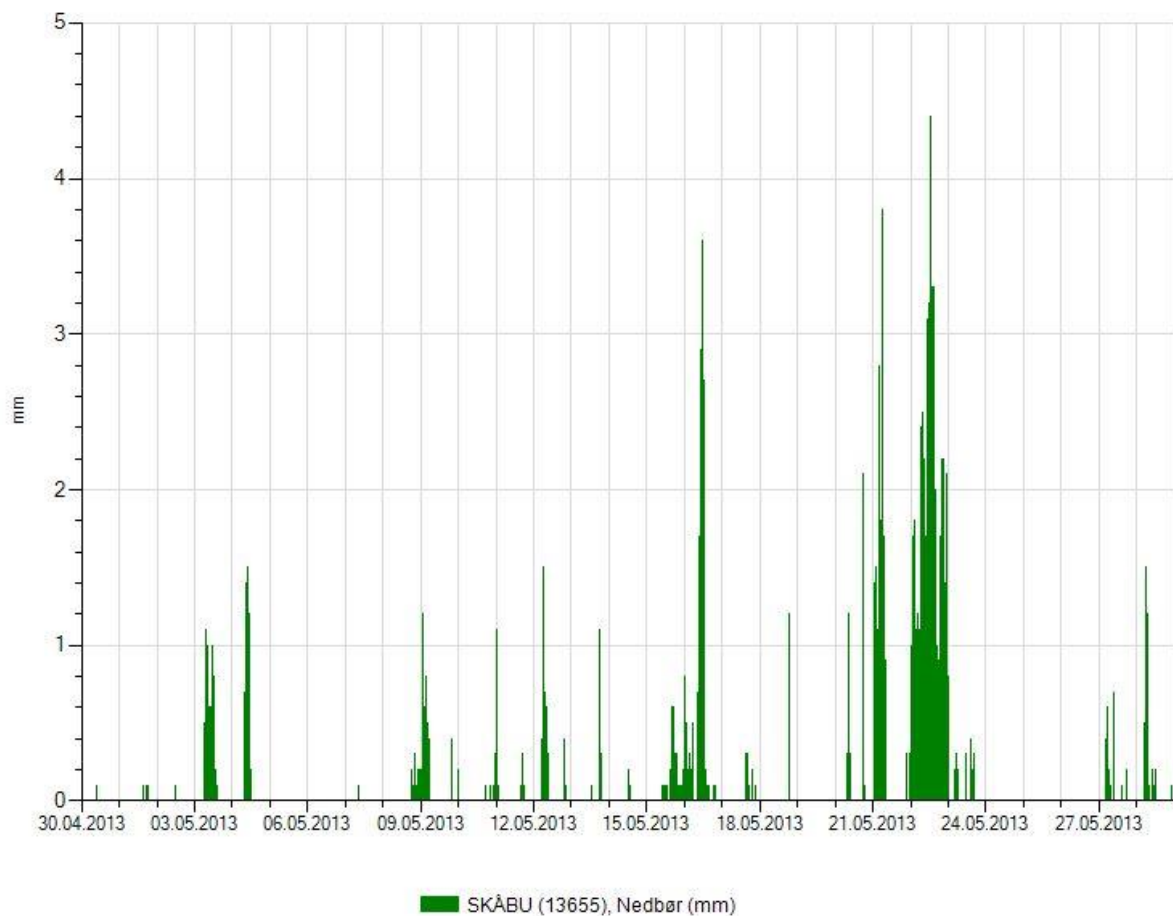
Figure 63: Hourly precipitation at Skåbu station, 22 km from the Kvam site (Senorge, 2017).

Frost is however registered in the ground throughout the release area and the field aboveboth on, and leading up to May 22.

www.varsom.no (2017) lists the risk of landslides on May 22. 2013 as red (4) on a scale from green (1) to red (4). Thus, the likelihood of landslides occurring in the general area was estimated to be very high.

5.5 The field work form

The field work form is found in Appendix 1. It is divided into a general part, a specific part for the release area, transport zone and area of deposition, and an appendix section. The first page is regarded as the bare minimum of information that should be provided in order to do statistics on landslides, such as runout length and elevation difference. This part also includes a schematic of a landslide and the parameters. The following two pages contain further general information, and room for a sketch. The following three parts provide checkboxes and parameters to be determined for each of the three abovementioned parts of the landslide, each with a descriptive schematic of the respective part. Note that for all sections, many of the parameters can be initially established using aerial photography, and verified or corrected in the field.

The appendix section contains checkboxes for the different kinds of appendices. The top two (pictures and map) are regarded as the most crucial ones.

A guide for the use of the field work form can also be found in Appendix 1, and section 6.9 contains a discussion regarding the usefulness of the form.

6 Discussion

In this section, results and observations will be used to characterize the landslides, their triggering and conditioning factors and similarities, as outlined in objective 2, section 1.

The ability of the runout simulations to reproduce the findings, based on the data gathered, will be evaluated, and factors affecting the precision discussed.

Furthermore, the results, and abovementioned discussions, will be used in the discussion about and determination of the usefulness of the field work form, as formulated in objective 1, section 1.

6.1 Grain size analysis

6.1.1 Norangsdalen 1

At Norangsdalen 1, it appears to be two distinct layers (Figure 50); one layer of landslide material covering the surface of the entire slope, and a finer layer (sample 7) stratigraphically below the former. This is supported by the field observations of a different looking layer, and the fact that the sample from this layer displayed a much finer grain size distribution than the four other samples. This layer was only observed in the lower half of the transport zone. The general area is covered in both landslide material and till, and the bottom layer is assumed to be comprised of the latter.

6.1.2 Norangsdalen 2

Throughout the upper transport zone (sample 3) and the release area (sample 1), the same material seems to be dominating, until deposition starts. High content of fines (Figure 51) and generally weathered bedrock, suggests that weathering of the bedrock and soil have altered the soil cover significantly. Mechanical weathering through frost action and root weathering seem the most likely mechanism and agents.

Deposits on the lobe (Samples 8 and 12) have a large content of fines as well, though smaller amounts of sand. As the depositional lobe is observed to have a steep front, with large clasts, this might suggest that the flowing masses formed a coarse front, as outlined in section 2.4.2, partially hindering the finer phases from escaping the depositional lobe.

6.1.3 Årset

As the uppermost layer at Årset consisted of a thin layer of peat and rocks, which were impractical to sample and easily identifiable, it was not sampled. The underlying soil layer was sampled (sample 9), and showed a similar distribution (Figure 52) to that found further downslope (sample 15). They are assumed to be fine tills, possibly containing weathering material from the overlying peat.

The coarser layer, sampled further downslope (sample 6), is assumed to be the same layer that acts as a sliding plane for the overlying layer, sampled upslope. Findings done by Sandøy et al. (2017) at the same site support this assumption. This layer is assumed to be coarse till.

The much higher content of fines in samples 9 and 15 might indicate a higher degree of weathering.

6.1.4 Kvam

At Kvam, the samples from each of the two release areas (samples 11 and 13) are close to identical up to the gravel fraction (Figure 53). This is assumed to be till, with a high content of fines. The ridge separating the release areas (sample 5) shows a distinct lower content of clay and silt. A possible explanation for the higher content of fines is that the release areas have had water running through them for a long time, weathering the material and amplifying the effect of freeze thaw processes. This is supported by the fact that there appears to be a drainage pattern from each of the release areas, visible in the FKB contour data, preceding the landslide event.

The sample collected in the lower transport zone (sample 14) is coarser than the ones collected in the release area, and had a larger number of well rounded large clasts. The simulations indicated some deposition in this area, and while aerial photography shows little deposition except for levees, this layer is thought to at least partially originate from slope processes.

6.2 Geophysical methods

Assuming the sub surface interface that is to some extent consistently identifiable in all the GPR profiles is the bedrock, there seems to be an increase in the depth to the bedrock from the field above the release areas to the release areas and the upper part of the transport zone.

As both methods indicate a dipping interface to the north and south of the field (Figure 55, Figure 56), the assumption of this interface being a dipping bedrock surface is given a high degree of confidence. The depth in these segments is however less certain. Looking at Table 5 in section 3.3.1, the radiowave velocity in water is much lower than in air. Assuming a higher degree of water saturation with increasing depth, this can cause an overestimation of the depth. The lower resistivity areas in the northern and southern parts of the ERT plot (Figure 56) also indicate higher water saturation, high content of fines and possibly conducting minerals. Again, looking at Table 5, silt and clay display a higher conductivity (inverse of resistivity) than do tills and gravel, and most materials experience higher conductivity when satured with water, though some tills might experience the opposite effect. Possible drainage patterns can be observed from the dipping segments (Figure 64). The possible increase in depth to bedrock above the release area observed in profile 110 (Figure 58) might be connected to drainage on the surface and in the subsurface leading water into the release areas. This drainage path might be connected to the dipping interfaces on the field above, though the data in the area separating the release area and the field up slope is insufficient to verify this.

Figure 64: Contour lines (1 m) and aerial photography (Norge i bilder, 2017), with the dipping, and possibly dipping, segments marked along the GPR profiles. To the right, the GPS track around the release area is plotted in purple.

GPS profiles logged perpendicular to the landslide track where the channel bed had eroded down to the bedrock shows a height difference of 2-5 m. The 2 m measurement was done parallell to the area where profile 103 (Figure 57) shows the interface close to the surface. The GPR profiles perpendicular to the flow direction all show interfaces shallower than 10 m. Most perpendicular profiles indicate a depth to interface of 5-6 m, and as the velocity is expected to decrease with depth, as disscussed above, the former is chosen as the depth to bedrock (maximum erosion depth) in the runout simulations.

The failure to identify any bedrock surface directly below the release areas is not fully understood. Further discussed in section 6.5.2, small or shallow features might not be identified by a low frequency antenna such as the one used. However, interfaces are identified on both sides of the release areas, and between them. The middle section is stretched out, probably as a result of the antenna remaining stationary, and the length is therefore not correct. Depth of the release areas should not be deep enough to mask the bedrock depth, given a depth of at least 4 m observed on profile 111.
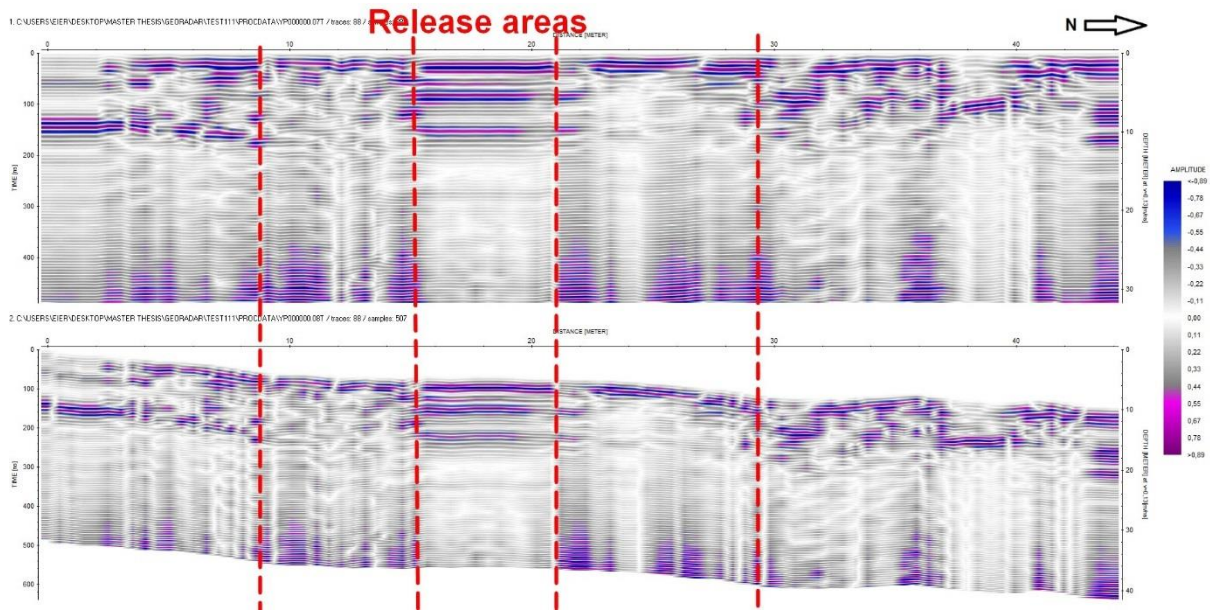
Figure 65: Profile 111, crossing the release areas and the ridge dividing them. Note that the interface assumed to be the bedrock surface is not observed in any of the release areas. The interface between the release areas have been stretched, probably due to the antenna shooting several traces while stationary, and the length is therefore not reliable.

It is possible that the phyllittic bedrock in these particular segments has been subjected to increased weathering by higher water supply, causing a weaker wave velocity interface. Looking at Table 5 in section 3.3.1, the higher content of silt and clay (Figure 53), and potentially higher degree of water saturation, would cause lower wave velocities and reduced signal because of high conductivity. Thus, the bedrock may indeed be at a greater depth, though the weathering of the rock might itself reduce signal and overestimate depth. A combination of the two seems most likely.

Around 560 m.a.sl. the bedrock can be observed at the surface and in cuts, but the GPR data from this altitude is missing.

6.3 Weather at the selected sites

6.3.1 Årset

Though intense precipitation was observed in the time leading up to the landslide, this was well below the thresholds estimated using Sandersens (1996) equation (Table 11). The

gridded values at the site are however lower than those registered at the nearby Ørsta-Volda airport and at Emblem, the latter registering hourly precipitation. The 12 hour precipitation at Emblem (Figure 62) is more than 80 % of what would be the 12 hour threshold for a slope with Emblem's mean annual precipitation (2000 mm). As Årset is estimated to receive higher amounts of precipitation, due to location and aspect of the slope, the gridded values are probably too low. There are also terrain features, such as the above lying ridge and taluses, likely to amplify the water input in the release area. This is also true for the snow melt in the area. Thus, considerably higher input is expected, and the precipitation intensity during lower time spans is probably larger. Also, the mean annual precipitation is based on gridded data, and might be significantly overestimated.

6.3.2 Kvam

Like at Årset, high precipitation is observed, though below the thresholds (Table 11). However, the gridded 24 hour precipitation is more than 86 % of the critical 24 hour water supply, and small inaccuracies might have a large effect. It is likely that considerably higher intensities were achieved during shorter time spans. This also means that any terrain features leading water into the release areas will have a crucial effect. Such features seem likely, given the observations in sections 6.1.4 and 6.2.

6.4 Runout simulations

6.4.1 Norangsdalen 2

The initial DEM used at this site had a resolution of 5 m, and failed to reproduce anything resembling field observations as the landslide quickly spread out across the slope. The DEM made using interpolated GPS data, merged with the low-resolution DEM, produced flow paths and depositional areas fitting field observations well. Differences in runout lengths were all less than 3.5 % (23 m) (Table 8).

Final volume was within 26 % of that observed at the best (simulation 4). Inaccuracies in measurements might partially explain this, as GPS coverage was lacking in the forested area around the depositional area. Also, only one material behavior was modelled, and the model does not consider the flowing masses partitioning into different phases when depositing. The

depositional lobe has probably settled since the event and some fines have been washed away by precipitation.

Outlined in section 3.4, one would expect the runout simulations to produce slightly higher final volume values than the volume estimated from the depositional area. However, the volume in the depositional area is much greater than what is expected to have been deposited further up slope, and the measurements of the depositional area are assumed to be significantly more accurate than estimates of the eroded volume through the flow path.

Also, finer phases of flowing material such as hyper concentrated flow, mentioned in section 2.4.4, might have progressed beyond the depositional lobe visible at the time of the survey. As such, one would expect the total volume of the landslide to be larger than what is visible more than a year later. Still, it seems likely that the coarse front, limiting the partitioning of the flowing masses into different phases as it is deposited, will be more accurately simulated by a single phase runout simulation than flows where coarse fronts are not present.

The high velocity of simulation 5 was unexpected, as increasing the turbulence coefficient increases the velocity in the other simulations. The most likely explanation is that the crudeness of the interpolated DEM leaves some sharp vertical falls, and that particles passing over these are rapidly accelerated. These features increase with distance from the center of the channel, which contains the highest amount of data-points for interpolation, and the initially slower material might overflow the channel more rapidly. Thus, simulation 5 displays an unrealistic velocity, assumed to originate from limitations of the interpolated DEM, and should be disregarded.

The simulations suggest a maximum velocity around 10 m/s to be most probable, well above the estimated minimum velocity of 7.3 m/s. And the high friction ($\mu = 0.368$, $\xi = 1000$) simulation produced the best fit. The parameters provided proved adequate to produce a simulated landslide closely resembling the field observations. This simulation illustrates the importance of a high-resolution DEM, and showed the GPS data to be particularly useful.

6.4.2 Årset

At Årset, the model struggled to reproduce the runout lengths observed in the field. An increased turbulence coefficient of 3 orders of magnitude, between simulations 5 and 6 (Table 9), had negligible effect (0.4 %) on runout length. Neither did it affect the final volume to a great degree. Reduction of the friction coefficient, in simulation 7, did however produce a geometry closely resembling that of the observed depositional area, while producing a final volume 51 % larger than that estimated.

However, the sliver running down to the river was not reproduced. This might in part be explained by the fact that the DEM is based on contour lines extracted after the landslide. Thus, large parts of the depositional area have been modified, and are located higher than previously, with less obvious terrain features to lead the masses. Also, a canal has been dug in the depositional area leading west. Figure 60 clearly illustrates this, as the deposit thickness is much higher in the canal and the area it terminates, than on the opposite side.

Like at Norangsdalen 2, it is likely that phases of finer material have been transported further and are not visible as a part of the depositional area at the time of the survey. Also, as outlined in section 3.4, the model is expected to produce a higher final volume than estimated through field measurements of the depositional area. Further, the masses are reported to have settled significantly during the days following the event (section 4.5.7). Thus the depositional area has been modified both naturally and artificially following the event, and like at Norangsdalen 2, is expected to have displayed a larger volume than at the time of surveying.

Given these considerations, simulation 7, with a friction coefficient of 0.15 gives the best fit, and the initially calculated friction coefficient of 0.277 is too high. While the data gathered in the field was sufficient to do the simulation and produce a geometrically good fit, the DEM provided causes the model to perform questionable in the depositional area. While a good fit is achieved, a higher friction coefficient might perform equally well with a better DEM. As the selection of DEM is not the focus of this thesis, and other high resolution DEMs from the area are unavailable, the simulation has demonstrated the data collected to be sufficient for performing runout simulations.

6.4.3 Kvam

The simulations from Kvam produced reasonable geometries (Figure 61) and runout lengths (Table 10). Runout length is, however, not regarded as a useful parameter to tune the input in this case, as it is limited primarily by the river. This site has the largest uncertainty in regards to volume, though the estimated volume agrees well with those simulated. The lowest discrepancy was 11.5 % which is among the best results of all the simulations done at all three sites. This suggests that the combination of aerial photography and GPS data delivered accurate data. Kvam was the only site in which geophysical methods were used, and the better mapping of the depth to bedrock might help explain the good accuracy. However, it seems reasonable that the accurate DEM, and the channelized nature of the landslide, are the main contributors to these results. The model also managed to reproduce the secondary channel, visible in Figure 47 and Figure 48.

The fact that a DEM from before the event accurately reproduced geometries similar to those observed, is indication of at least some degree of activity along the same path preceding the event being investigated.

The model results also indicate some deposition on the flatter surfaces of the lower transport zone. It was speculated on, during the field survey, whether material was deposited in this area, and though no visual evidence could confirm it, the simulations strengthen this theory.

In the runout simulations, some of the masses flow 60 m to the south of the main flow path (Figure 61), into the path of a landslide from 2011. Though some of the masses are expected to overflow the main channel, evidence of this new flow path was not observed in the field. This is interpreted as an artifact of the DEM being collected between the 2011 and 2013 flooding.

6.5   Assumptions and sources of error

6.5.1   Grain size analysis

Diameters determined by a sieve are likely to represent the intermediate axis of the particle, which might be significantly smaller than the equivalent volume spherical diameter, recorded

by the Coulter counter (W. R. Parker, 1984). This might explain the small values registered in the transition between Coulter and sieving data in some of the grain size distribution plots. This is to be expected when adding together sieving and Coulter data, particularly when the coarse fraction of the fine sample is small (M. S. Naoroz, pers.comm., 2017). Also, the minimum mesh size for the sieving and the upper limit grain size for the Coulter test were changed after sample 3. Thus, this and other effects of the conversion will affect the samples differently.

The handbook *Laboratorieundersøkelser* (Statens Vegvesen, 2014) lists the minimum sample size in order to be representative, by weight, in relation to the largest clast diameter (D) of each sample. Samples containing grains with a diameter $D_{max} = 16$ mm, ideally require a sample size of 2.6 kg. This was not practical sampling in the field, due to carrying capacity, or in the lab, due to time and equipment limitations. This might skew the results.

The image analysis used area to estimate percentage of coarse to fine grains. The volume and density will however vary.

When only taking few samples from each site, there is always a risk of the sample not being representative of that particular locality, though this was carefully considered while sampling.

6.5.2   Geophysical methods

As reflection acquisition was the method in use, subsurface velocity had to be estimated by using diffraction hyperbolas visible in the plot. Hyperbolas were not found in all plots, and the same approximation has been used on all profiles. No large variations in the soil cover were observed in the area surveyed by radar, and the (NGU) maps show no deviations from the thick till displayed in the area. The assumption is that the subsurface velocity is virtually equal throughout the study area. That is however probably not the case and any differences will affect the depth estimations.

During processing, it was found that the 50 MHz readings were registered with a constant offset, meaning that each individual trace was registered with an equal distance to one another, normalized within the limits of the profile length. This means that two traces, recorded at the exact same position, do not register as such. The most profound proof of this can be found in unrealistically horizontal structures. In the most obvious cases, these traces

have been deleted, but one should keep in mind that the horizontal position of terrain features and reflectors might be imprecise when interpreting the 50 MHz radar profiles. Further, the low accuracy of the attached GPS introduces some inaccuracies with regards to the precision of the correction topography and location of the profile.

The GPR data will have a vertical resolution of roughly $\frac{\lambda}{2}$ (s. Bazin, Pers. Comm. 2016. The wavelength (λ) can be estimated putting the frequency and estimated wave velocity into equation (3.3):

$$\lambda = \frac{v}{f} = \frac{0,13\frac{m}{ns}}{50\ MHz} = 2.6\ m$$
$$\frac{\lambda}{2} = 1.3\ m$$

This means that features smaller than 1.3 meter might be missed, and that the survey might fail to identify the bedrock if shallower than 1.3 meter.

In terms of the ERT and IP data, it is important to understand that the resistivities estimated through inversion are geometries and resistivities providing a sound explanation of the subsurface. Several combinations of resistivity and geometry might reproduce the same readings (Reynolds, 2011), and inversions should be treated with skepticism until verification and calibration by other means can be done.

Also, for all geophysical methods, boundaries and features in the subsurface will not be registered unless there is a difference in the physical property being measured. Looking at Table 5 and Table 6 the same soil or rock might have a range of parameter values, and there is often an overlap, that might conceal geological boundaries and features.

6.5.3 Runout simulations

The runout simulation results are fully dependent on the input topography files, and material property parameters. The level of accuracy of each vary between the sites and some points are particularly important sources of error:

1: At Norangsdalen 2, only 5 meter contour lines were available in the upper two thirds of the landslide area. GPS data preceding the event was interpolated. As such, the terrain was that of a channel and not fully representative of the terrain preceding the event. Also, the interpolated

DEM displays a lower accuracy with increased distance from the center of the channel, and appears with a stairwell structure given sufficient distance. The anomalous velocity of simulation 5 is believed to be a result of this (section 6.4.1).

2: The Kvam site landslide terminated into a river and the depositional area has been the site of reconstruction work, meaning that the depositional area itself could not be measured in the field. Also, the runout length is predominantly determined by the terrain at Kvam, and was therefore of limited use when tuning the input parameters.

3: At Årset, a lot of construction and rebuilding has been done, and masses have been removed from the depositional area. This makes the determination of the exact boundaries and height of the depositional area harder to determine, and the estimations more uncertain. Like at Norangsdalen 2, the DEM at Årset is based on data collected after the event, and thus is not fully representative of the terrain preceding the event. High resolution data preceding the event were not available.

4: Outlined in section 3.4, the final volume calculated by DAN3D includes masses deposited through the flow path, while the volume of the depositional area, measured in the field, does not.

All simulations had a final run-time of 500 seconds. While some particles would still be moving after this time, and total volume would grow, it is assumed that any such slow processes taking place after this time would not be simulated well by the initial input material, as material settles and water escapes. Allowing the model to run too long might in fact produce overestimations of the final volume, and 500 seconds was selected as it allowed sufficient time for the correct geometry to develop.

6.5.4 GPS data

The GPS has an optimal precision of 10 cm. For this to be achieved, a good link to the GSM (mobile phone) network and sufficient satellite coverage is needed. At Norangsdalen 1, the GSM coverage was poor, and precision suffered as a consequence. Measures have been met to compensate for this, but the deviances are clearly visible in the GPS data.

Where vegetation was dense, satellite coverage was of varying quality. In the depositional lobe of Norangsdalen 2 and vegetated areas of Kvam, precision might decrease significantly

128

as a consequence of this. Major outliers are in all cases clearly visible when the GPS data is plotted, and precision listed in the data file. Parameters estimated from GPS data should thus have a margin of error of 10 cm.

6.5.5 Weather data

The 24 hour weather data is derived from gridded values estimated for the sites at www.senorge.no (2017), and must be treated with some degree of skepticism as they are not verified by actual measurements. This is also true for the gridded mean annual precipitation data, where the lower value of the range has been used in the calculations of section 5.4 in order to produce conservative estimates.

On the other hand, the hourly data are logged at stations several kilometers from the sites and at different altitudes. Thus they might not be adequately representative of the conditions at the sites.

6.6 Conditioning factors and triggering mechanism

6.6.1 Norangsdalen 1

As there is no clearly defined release area, and the channel results from several events, the initiating mechanism at this site has the highest uncertainty. The presence of ledges in the mountainside above the channel, and the furrows leading down to the channel, strongly indicates that the events are triggered by high water supply. Accumulation, and subsequent melt, of snow on the ledges are likely contributors to this input. The fact that the slope is located in the rain-shade of the mountainside, facing east, is expected to limit the precipitation and snow melt, due to limited solar radiation. However, the convergent geometry of the mountainside is expected to funnel water into the channel. Events might also originate as slush flows (highly water saturated snow avalanches (Norem et al., 2012)), once wet snow accumulated on the ledges above the channel is mobilized during warmer and/or wetter periods.

The landslides were most probably triggered by high water input, and subsequent entrainment, the most probable source being a combination of snowmelt and precipitation. This is a well-documented cause of flooding in Western Norway during the winter (Tollan, 1977, Høeg et al., 2014).

6.6.2 Norangsdalen 2

At Norangsdalen 2, the soil cover in the release area is thin (0.25–0.5 m) and the bedrock surface oriented close to parallel to the slope. As outlined in section 2.6.2, thin layers of soil are more vulnerable to increased pore water pressure, and the parallel orientation of the bedrock provides less friction and facilitates water flow. Thus, this area is likely to be vulnerable to high water input. The area of exposed intact bedrock 10 meters upslope of the release area is likely to have supplied the release area with water, contributing to its failure.

The degree of weathering of the bedrock seems to have played a significant role as the bedrock in the release area is highly fractured. The dense vegetation has probably contributed to the fracturing through root anchoring in addition to frost action. Possibly, the fractured bedrock, in which the roots were anchored, constituted a weak layer itself, and high pore water pressure might have built in the cracks.

Located on a south-west facing slope, the area is expected to experience more precipitation and rapid snow melt than does Norangsdalen 1. High water input, primarily from precipitation, and a subsequent buildup of high pore water pressure in the interface between the soil and bedrock is assumed to be the triggering mechanism.

6.6.3 Årset

The convergent geometry of the slope, and the shape and direction of the above lying ridge are likely to funnel water towards the release area. In addition, the slope is facing south-west, and is likely to receive high water input. This is evident by the high estimated annual precipitation at this location, and the rapid melting due to high solar radiation. The increasingly thin vegetation from the release area and upwards means that less precipitation is intercepted, and there is less evapotranspiration. In addition, the less vegetated areas are likely to experience less water infiltrating into the soil (Sidle and Ochiai, 2006), thus increasing the overland-flow of water down slope.

The stratigraphy of soil layers appears to have been a crucial destabilizing factor at Årset. The bottom till layer, still intact in the release area, is overlain by a possibly more weathered till, high in fines. At the top, there is a thin (< 20 cm) layer of cobble and boulders covered in peat. Thus, the top layer is expected to have a high permeability and produce high loading on the layers below. The middle layer, however, is expected to have a lower permeability, relative to the coarser underlying till, due to the high amount of fines (Ameratunga et al., 2016). This would produce a situation where water input is rapidly infiltrated into the top layer, increasing the weight. Similarly, the bottom layer, with its higher permeability, might have been infiltrated more rapidly, from areas of exposed bedrock upstream, than the middle layer, building high pore water pressure and rising ground water table in the bottom layer and the transition to the middle layer. As the middle layer is less permeable and infiltration of water into this layer will be slow, pressure will build along this boundary, ultimately detaching the middle and upper layers. This is the preferred explanation of the triggering mechanism. Figure 66 illustrates a similar case to that described above, where a sliding plane develops along the boundary between saturated and unsaturated soils.
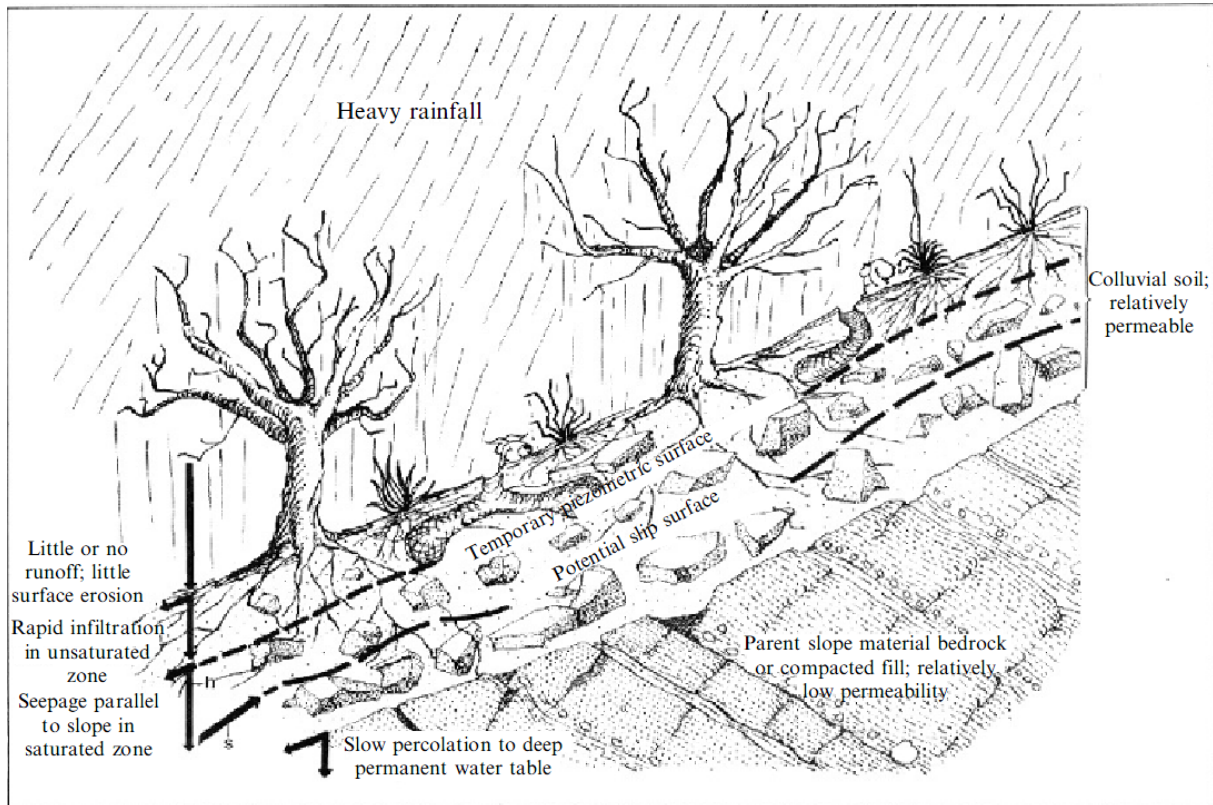
Figure 66: Illustration of how water infiltrates during intense precipitation, and slip surfaces develop once water pressure builds along the boundary between saturated and unsaturated layers (Savage, 2005).

On the other hand, an alternative explanation is possible. As outlined in section 2.6.4, the middle layer, in spite of its higher content of fines, might be more permeable due to more weathering of this layer than the more consolidated layer below. In this case, the middle layer will be saturated more rapidly than the bottom layer, pore water pressure will build in the middle layer and along the boundary to the bottom layer, and a sliding plane develop along this boundary. This is a frequent cause of slope failures in Norwegian circumstances (Bargel et al., 2011), Figure 9, section 2.6.4 shows an example of this case.

The release area is located at the top of the tree line, and is thinly vegetated. Little stabilizing effect is expected from root anchoring or moisture modification. On the contrary the vegetation might have transferred energy from the wind into the ground. Though this might have some destabilizing effect, it is regarded as a far less important factor than water input in this case.

Looking at the weather data, intense precipitation was observed in the hours leading up to the landslide. While precipitation never exceeded the critical water supply (Table 11), the 12

hours leading up to the event had precipitation within 80 % of that calculated as critical water supply, given the mean annual precipitation at that station. In the 48 hours leading up to the event, snowmelt values of 4 and 6 mm/day are registered.

Given the number of factors likely to amplify the effect of high water input, intense precipitation seems the most likely triggering factor.

6.6.4 Kvam

This area has been subject to numerous debris flows previously, most notably during the spring of 2011. Aerial photography preceding the event shows a slightly less vegetated strip in connection with the release area. The contour lines, also preceding the event, reproduced the flow path observed in the field when input to DAN3D, indicating a drainage pattern and erosion along the path. Ice and running water was observed during the field survey in October 2016.

GPR data suggests a bedrock depth of more than 4 m around the release area, and bedrock was not observed in the release areas themselves. ERT/IP and GPR data from the field above the release areas, and between the field and release areas, suggest sub surface drainage patterns leading from the field to the release areas. The results might also indicate these paths having a larger fraction of fines, possibly due to increased (surface and sub surface) water flow, and subsequent sediment transport and/or increased weathering in the wetter areas. This fits well with the grain size analysis, with both release areas displaying a significantly finer grain size distribution than the ridge separating them. The drainage patterns might originate from, and enhance, zones of weakness in the bedrock, and increased weathering in bedrock and soil is expected along this path. Swales on slopes are often the result of weathering of the bedrock along zones of weakness (Chatwin et al., 1994).

Given the high content of fines in the release areas (Figure 53), these areas are expected to have lower permeability than the ridge (Ameratunga et al., 2016).

On May 22. 2013 there was intense precipitation in the area, though not exceeding the critical water supply thresholds (Table 11). Given the considerations above, it seems likely that high water input has triggered the landslide. Buildup of pore water pressure, and subsequent failure, is assumed to be the triggering mechanism, seeing as there are well defined release areas. A similar mechanism to those outlined at Årset is possible. High pore water pressure

might have built in the boundary between the finer soil of the release area, and coarser surrounding soils. However, as outlined in section 2.6, soil layers of high thickness are less vulnerable to increased pore water pressure than thin soil layers. This might suggest that the slope had a low factor of safety preceding the event and/or large vertical differences in soil properties not observed during surveying.

It is also possible that running water has eroded parts of the release areas, or the channel, triggering the failure of the release areas. Thawing, and subsequent strength loss, might also have played an important role.

The order in which the landslides were initiated is unknown. The channel running from the upper release area, down to the lower one, might indicate that the lower release area failed first, and a subsequent retrogressive failure occurred in the right release area. Multiple retrogressive failures can be observed throughout the course of the landslide path.

6.7   Characteristics of each slide

6.7.1   Norangsdalen 1

Though the channel is expected to experience running water over prolonged periods, the length of the depositional area, with large particles and coarse levees, and its changing courses, support the initial theory that this is the result of debris flows (Hungr et al., 2013), as defined in section 2.2. There is damming in the channel and a number of channels running in the depositional area, indicating surging. Though some of the largest boulders are deposited on the levees at the mouth of the channel, the fronts throughout the length of the depositional area are steep and dominated by coarse clasts. It seems probable that numerous surges and/or events have flowed with coarse boulder fronts, and that the escape of fines has been limited by this, also during deposition.

The ledges above the channel might have accumulated some colluvium, though little debris transport is expected to have occurred above the channel. The most probable explanation is that a debris flow has formed through bulking, mentioned in section 2.6.4, in which the water incorporates sufficiently large masses throughout its path to evolve into a debris flow.

134

Deposition is caused by reduction of slope angle. Though the channel decreases depth, and opens towards the end, this is assumed to be caused by decreased bed erosion, resulting from decreased velocity.

6.7.2 Norangsdalen 2

The presence of a well defined sliding plane suggests that the landslide might have started out as a debris slide. Through the course of the upper transport zone, the masses seem to have flowed at relatively low velocities, flowing around particularly well anchored patches of vegetation.

From the second segment of the transport zone, velocity seems to have increased as the track widens, and following the large boulder (Figure 36), it is no longer forced around obstacles. The width of the transport zone appears to be partially caused by the forcing of the flow around the boulder. While channels have developed in this segment, the main track itself is regarded as the dominant feature.

As levees start building and a well defined depositional lobe with steep ($< 40°$) fronts laden with boulders develop, the landslide is thought to have assumed a flow-like behavior. The channel eroded on the lobe indicates one or more surges. Thus, the event might have involved all three stages mentioned in section 2.2, initiating as a debris slide, evolving into a debris avalanche and finally debris flow. While some debris avalanches also surge (Jakob and Hungr, 2005a), the steep boulder front of the depositional lobe indicates that debris flow(s) did develop (Hungr et al., 2013, Takahashi, 2007).

6.7.3 Årset

The landslide at Årset has a geometry characteristic to that of debris avalanches. It seem to have initiated as a debris slide, given the presence of a well defined sliding plane, gained momentum and eroded down to the bedrock. The presence of large boulders in the lower part of the depositional area indicates high energy.

Debris flows might have formed during the event, as well defined channels were visible the following day. Scarps observed in the side of the flow path might indicate retrogressive failures, and possibly surging, as these phenomena are often observed in debris avalanches as outlined in section 2.4.2.

In the depositional area, some degree of stratification can be observed as larger boulders are underlain by finer masses. It appears to be a coarse to fine depositional sequence longitudinally, though some of the largest boulders have been removed during the rebuilding and modification of the depositional area. The depositional front is mainly confined in connection with the road. This is because these areas have been leveled when the houses were built. On the southernmost part of the lobe, however, this is not the case, and masses have flowed to the field and river below. These masses appear finer than the ones observed further up, and seem to verify a coarse to fine stratification.

The main reason for the deposition is the decreasing slope angle, though the shape of the depositional area seems to have been strongly affected by the road and houses.

6.7.4   Kvam

The Kvam landslide followed swales in the slope, expected to have some running water relatively regularly. Though aerial photography shows no evidence of events of this magnitude occurring since 2004, it seems likely that debris flows and/or floods occur with some regularity, as the swales fill with sediments before being mobilized during extreme events.

Due to the well-defined channel, erosive force of the slide and the scarp of the release area, the landslide is defined as a debris flow. While flooding is likely to have occurred on the slope at some point in time, the release areas indicate the flow to have formed from a failing mass of saturated soil. Also, the erosive and destructive force, evidenced by channel erosion and damage to vegetation, supports the assumption of a debris flow (Pierson, 2004, Jakob and Hungr, 2005a). The presence of numerous smaller scarps, joining the main debris flow path, indicates surging due to retrogressive failures to have occurred.

The landslide terminated in the river at the base of the valley. Some deposition is expected to occur in the field, in which the lower transport zone runs, based on simulations, grain size analysis and observations. Thus the main stopping mechanism is the river, while slope angle is likely to have played a significant role in how large masses reached the river.

6.8 Differences and similarities between the sites

As mentioned in section 4.2, Kvam is located in a continental subarctic climate, while the other three are in a marine west coast climate. This is illustrated by the season in which the debris flow at Kvam and debris avalanche at Årset occurred. All the landslides are however expected to be triggered by intense precipitation, though snowmelt and/or slush flows might have an equal significance at Norangsdalen 1.

The topography of the terrain surrounding the release areas have played a vital role in all cases. All three sites in Western Norway are located beneath ridges, mountaintops and slopes believed to funnel water into the release areas. At Kvam, the terrain and bedrock topography are believed to have a similar effect, though to a lesser extent. North-east of the release area at Norangsdalen 2, an unvegetated patch is believed to have drained water into the release area, while patches of fragmented rocks probably did the same at Årset.

The exposed bedrock, and thin soil cover, in the release area at Norangsdalen 2 probably played a vital role in acting as a sliding plane, and the buildup of pore water pressure. Similarly, at Årset, a vertical transition between soil layers formed a sliding plane.

Lack of vegetation is believed to be a contributing factor at Norangsdalen 1 and Årset. At Norangsdalen 2, the roots appear to have been anchored primarily in the thin soil cover and weak rocks, providing little stabilizing effect once the soil failed. Kvam stands out, as the release area, and the surroundings, were densely vegetated.

Norangsdalen 1 and 2 displayed deposits with steep fronts dominated by boulders, indication of debris flows with well-developed boulder fronts, as outlined in section 2.4. The debris avalanche at Årset shows a coarse to fine depositional sequence.

Norangsdalen 2 has an H/L ratio of 0.62, while the other sites have H/L values between 0.47 and 0.5. The relatively short runout length, compared to Norangsdalen 1 and Kvam, might in part be explained by the fact that the latter two have a higher degree of channelization. Also, the surface over which the masses were deposited is dominated by large blocks and dense vegetation, inducing high friction. At the Årset site, on the other hand, the masses were deposited over relatively flat surfaces with little vegetation, partly explaining the runout length in spite of the limited channelization.

6.9 Field work form usefulness

The field work form, and the methodology used, proved sufficient in providing the data needed for runout simulations and the characterization of the individual debris flow/debris avalanche (purposes A and B, section 1). In that regard, objective 1 (section 1), is fulfilled, and regarded as a success per the criteria outlined in the introduction.

In its current form, checkboxes and short fields keep the reporting in the form simple, leaving further elaboration and investigative methods to appendices. Herein lie both the strength and weakness of this form. A more in-depth form, taking a larger number of eventualities into account, might be impractical and cumbersome to use. Still, leaving too much to appendices and personal notes provides more room for personal interpretations and various reporting depending on the individual expert. A balance between the two has been sought through testing in both ends of the spectrum, and the current field work form is a solution believed to be a suitable middle ground.

Velocity estimation, though a parameter in the field work form, proved difficult. This is mainly due to the morphology of the debris flows and debris avalanche themselves, as superelevation and runup was rarely observed, due to the few bends and lack of runup to do velocity estimations on. The time between the events and the survey enhances this problem, as depositional areas have been leveled and modified. Thus, this is regarded as a consequence of the sites selected rather than a shortcoming of the field work form itself. Where superelevation was observed (Norangsdalen 2) velocity estimation was done.

Regarding appended data, GPS data improved the accuracy of measurements, and proved crucial in the creation of a DEM at one site. The soil samples, though of limited use in the runout simulations, were useful in establishing parameters important to understand the occurrence of debris flows. Similarly to the soil samples, geophysical methods only provided one input to the runout simulations, and are not deemed necessary for similar simulations. However, in simulations on the initiation of debris flows, depth to bedrock is an important parameter, and the data will be useful for other researchers involved in the Klima 2050 project.

7 Suggestions for further work and improvements

As the field work form is developed using the four site characterizations and DAN3D as feedback for its usefulness, further use is likely to introduce new dilemmas and avenues to explore. The robustness of the velocity estimations in particular was not tested much and any follow-up work should select sites at which measurement of superelevation and runup is more viable.

As the DEM interpolated from GPS-data improved simulation results significantly, standardizing a method for the acquisition, and interpolation, of GPS-data for this purpose could prove useful for future studies, where high resolution DEMs are not available.

Developing a script to extract the volume in the depositional area of the DAN3D output would be helpful in improving comparability between the simulated final volume and the volume estimated in the depositional area in the field. Alternatively, future studies should provide better estimates of the volume of masses deposited along the flow path, prior to the depositional area.

Though outside the scope of this thesis, a standard upper cutoff for the grain size analysis should be established in order to improve transferability of data between investigations of sites. For the purpose of this thesis, the grains sizes above 16 mm (plotted as < 32 mm in section 5.1) introduce a higher degree of uncertainty, and this is suggested as an upper cutoff for future work.

Expert feedback has been provided by Frode Sandersen, Anders Solheim and José Mauricio Cepeda. Accumulation of feedback from a broader range of users is certain to provide further suggestions for improvements. Similarly, testing the form against other programs than DAN3D might also produce further improvements.

A probing rod or similar devices might have proved useful in finding the depth to bedrock in the release areas of Årset and Kvam, and in the calibration of the radargrams. It is recommended that such tools are considered in future work.

8 Conclusions and closing remarks

The landslide designated Norangsdalen 1 has been defined as a series of debris flows, developed through bulking caused by high water input, and possibly slush flows. The ability of the mountainside above to accumulate masses and funnel water into the channel is believed to have been decisive in the forming of the debris flows.

The landslide designated Norangsdalen 2 has been defined as a debris flow, involving more than one surge, while it might have initiated and/or behaved as a debris slide and/or debris avalanche during earlier stages. The thin, weathered, soil cover and the weathered bedrock are probably the most important conditioning factors, precipitation being the most likely triggering factor.

The Årset landslide has been defined as a debris avalanche, triggered by intense precipitation, possibly involving one or more debris flows. Buildup of pore water pressure in the bottom layer and the transition to the less permeable layer above is believed to be the triggering mechanism.

The landslide at Kvam has been defined as a debris flow, triggered by intense precipitation and flooding. Surface and subsurface drainage patterns seem to dictate the location and geometry of the debris flow, and recurring events are expected.

Data collected using the field work form has been used in the characterization of the four sites. Three sites were successfully simulated in DAN3D producing geometries close to those observed in the field, and best fit volumes at all sites within 12 % of the estimates. As such, the field work form has fulfilled the success criteria outlined for the thesis.

References

AAHEIM, A., BLIKRA, L. H., JAEDICKE, C., SLETTEN, K., SOLHEIM, A., SORTEBERG, A. & STALSBERG, K. 2008. Resultater og anbefalinger fra geoextreme. *In:* GEOEXTREME (ed.).

AAHEIM, A., ROMSTAD, B. & SÆLEN, H. 2010. Assessment of risks for adaptation to climate change: the case of land-slides. *Mitigation and Adaptation Strategies for Global Change,* 15**,** 763-778.

AMERATUNGA, J., SIVAKUGAN, N., DAS, B. M. & SPRINGERLINK 2016. *Correlations of Soil and Rock Properties in Geotechnical Engineering*, Springer India : Imprint: Springer.

ANSCHÜTZ, H., LYSDAHL, A. & ANFINNSEN, S. 2017. GEOPHYSICAL FIELDWORK IN KVAM. Høgskoleringen 7 b, POBox 4760 Sluppen, N-7465 Trondheim: SINTEF Building and Infrastructure.

BARGEL, T. H., FERGUS, Å. T., DEVOLI, G., ORVEDAL, K., PEEREBOOM, I., ØYDVIN, E. K., STALSBERG, K., SLETTEN, K., FISCHER, L., RUBENSDOTTER, L. & EILERTSEN, R. 2011. Delrapport jordskred og flomskred. *In:* BARGEL, T. H. (ed.) *Rapport nr 16/2011.* Oslo: Norges vassdrags- og energidirektorat.

BARKER, D. H. 1986. Enchancement of slope stability by vegetation. Tunbridge Wells, Kent: Comtec Ltd. .

BECKMAN COULTER INC. 2011. *LS 13 320 Laser Diffraction Particle Analyzer,* 250 S. Kraemer Blvd. Brea, CA 92821, Beckman Coulter Inc.

BELL, F. G. 1998. *Environmental geology : principles and practice,* Malden, Mass, Blackwell Science.

BELL, F. G. 2002. The geotechnical properties of some till deposits occurring along the coastal areas of eastern England. *Engineering Geology,* 63**,** 49-68.

BERTOLO, P. & WIECZOREK, G. F. 2005. Calibration of numerical models for small debris flows in Yosemite Valley, California, USA. *Nat. Hazards Earth Syst. Sci.,* 5**,** 993-1001.

BREIEN, H., HØYDAL, Ø. A. & SANDERSEN, F. 2013. Forslag til kriterier for vernskog mot skred. Ullevåll Stadioon, 0806 Oslo: NGI.

CANNON, S. H. & GARTNER, J. E. 2005. Wildfire-related debris flow from a hazard perspective. *Debris-flow Hazards and Related Phenomena.* Berlin, Heidelberg: Praxis Publishing Ltd.

CAROLINE, A. S., WAYNE, S. R. & KEVIN, W. E. 2012. NIH Image to ImageJ: 25 years of image analysis. *Nature Methods,* 9**,** 671.

CHATWIN, S. C., HOWES, D. E., SCHWAB, J. W. & SWANSTON, D. N. 1994. *A Guide for Management of Landslide-prone Terrain in the Pacific Northwest*, Research Program, Ministry of Forests.

COSTA, J. E. 1984. Physical Geomorphology of Debris Flows. *In:* COSTA, J. E. & FLEISHER, P. J. (eds.) *Developments and Applications of Geomorphology.* Berlin, Heidelberg: Springer Berlin Heidelberg.

COSTA, J. E. & SCHUSTER, R. L. 1988. FORMATION AND FAILURE OF NATURAL DAMS. *Bulletin of the Geological Society of America,* 100**,** 1054-1068.

CROZIER, M. J. & GLADE, T. 2005. Landslide hazard and risk: Issues, concepts and approach. *Landslide hazard and risk.* Chichester: Wiley.

CRUDEN, D. M. & VARNES, D. J. 1996. Landslide types and processes. *Special Report - National Research Council, Transportation Research Board,* 247**,** 36-75.

DAHL, M.-P., GAUER, P., KALSNES, B., MORTENSEN, L., JENSEN, N. & VEIHE, A. 2013. Numerical runout simulation of debris avalanches in the Faroe Islands, North Atlantic Ocean. *Journal of the International Consortium on Landslides,* 10**,** 623-631.

DAHL, M.-P. J. 2011. *Risk management tools for flow-type landslides in the Faroe Islands, North Atlantic Ocean.* Ph.D., Roskilde Universitet.

DANIELS, D. J. 2004. *Ground penetrating radar,* London, Institution of Electrical Engineers.

DAVIES, T. R. H. 1986. Large debris flows: A macro-viscous phenomenon. *Acta Mechanica,* 63**,** 161-178.

DE BLASIO, F. V. 2011. *Introduction to the Physics of Landslides,* Dordrecht, Springer.

DELMAS, M., CALVET, M. & GUNNELL, Y. 2009. Variability of Quaternary glacial erosion rates – A global perspective with special reference to the Eastern Pyrenees. *Quaternary Science Reviews,* 28**,** 484-498.

DEVOLI, G., JENSEN, O. A., KRISTENSEN, L. J., LARSEN, J. O., RUSTAD, B. K., VERHAGE, A. & VIKLUND, M. 2015a. Terminologi for naturfare. *In:* KRISTENSEN, L. L. (ed.). Oslo: Norges vassdrags- og energidirektorat.

DEVOLI, G., KLEIVANE, I., SUND, M., ORTHE, N.-K., EKKER, R., JOHNSEN, E. & COLLEUILLE, H. 2015b. *Landslide early warning system and web tools for real-time scenarios and for distribution of warning messages in Norway*.

DIREKTORATET FOR BYGGKVALITET 2016. Byggteknisk forskrift (TEK 10). *In:* MODERNISERINGSDEPARTEMENTET, K.-O. (ed.). Direktoratet for byggkvalitet.

DIREKTORATET FOR SAMFUNNSSIKKERHET OG BEREDSKAP 2013. Evaluering av myndighetenes forebyggingsarbeid og håndtering av flommen i mai 2013.

ESRI. 2017. *ArcMap* [Online]. Available: http://desktop.arcgis.com/en/arcmap/ [Accessed 23. May 2017].

EVANS, S. G. & BENT, A. L. 2004. The Las Colinas landslide, Santa Tecla: A highly destructive flowslide triggered by the January 13, 2001, El Salvador earthquake. *Geological Society of America Special Papers,* 375**,** 25-38.

FERGUS, T., HØYDAL, Ø. A., JOHNSRUD, T.-E., SANDERSEN, F. & SCHANCHE, S. 2011. Skogsveger og skredfare - veileder. Available: http://www.skogkurs.no/userfiles/files/skogsveier/l_smasseskred_veileder_A4_14071 1.pdf.

FINLAYSON, B. 1981. Field measurements of soil creep. *Earth Surface Processes and Landforms,* 6**,** 35-48.

GAN, Y. 2017. *Geotomo Software* [Online]. Available: http://www.geotomosoft.com/index.php [Accessed 6. February 2017].

GAO, Y., GE, H. & XU, W. 2014. Control Effect of Vegetation on Debris Flows: A Case Study in Batang County, Southwest China. *In:* SASSA, K., CANUTI, P. & YIN, Y. (eds.) *Landslide Science for a Safer Geoenvironment: Volume 3: Targeted Landslides.* Cham: Springer International Publishing.

GEERTSEMA, M., VAN HEES, M., CHIARLE, M. & HAYEK, J. 2014. Debris Flow on a Seasonally Frozen Rupture Surface at Moose Lake, British Columbia. *In:* SHAN, W., GUO, Y., WANG, F., MARUI, H. & STROM, A. (eds.) *Landslides in Cold Regions in the Context of Climate Change.* Cham: Springer International Publishing.

GLADE, T. 2005. Linking debris-flow hazard assessments with geomorphology. *Geomorphology,* 66**,** 189-213.

GOLDEN SOFTWARE LLC. 2017. *Surfer* [Online]. Available: http://www.goldensoftware.com/products/surfer [Accessed 10. May 2017].

GUADAGNO, F. M. & REVELLINO, P. 2005. Debris avanalches and debris flows of the Campania Region (southern Italy). *Debris-flow Hazards and Related Phenomena.* Berlin, Heidelberg: Praxis Publishing Ltd.

GUZZETTI, F., PERUCCACCI, S., ROSSI, M. & STARK, C. 2008. The rainfall intensity–duration control of shallow landslides and debris flows: an update. *Journal of the International Consortium on Landslides,* 5**,** 3-17.

HANSSEN-BAUER, I. 2015. Klima i Norge 2100 : kunnskapsgrunnlag for klimatilpasning oppdatert 2015. Oslo: Norsk klimaservicesenter.

HANSSEN-BAUER, I., FØRLAND, E. J., HADDELAND, I., HISDAL, H., MAYER, S., NESJE, A., NILSEN, J. E. Ø., SANDVEN, S., SANDØ, A. B., SORTEBERG, A. & ÅDLANDSVIK, B. 2015. Klima i Norge 2100 : kunnskapsgrunnlag for klimatilpasning oppdatert 2015. Oslo: Norsk klimaservicesenter.

HIGHLAND, L. 2004. Landslide Types and Processes. *In:* U.S. GEOLOGICAL SURVEY (ed.) *U.S. Geological Survey,*.

HIGHLAND, L. & BOBROWSKY, P. T. 2008. *The landslide handbook : a guide to understanding landslides,* Reston, Va., U.S. Geological Survey.

HILLESTAD, K. 2013. Jordskred og flomskred. *In:* ENERGIDIREKTORAT, N. V. O. (ed.). NVE.

HUEBL, J. & FIEBIGER, G. 2005. Debris-flow mitigation measures. *Debris-flow Hazards and Related Phenomena.* Berlin, Heidelberg: Praxis Publishing Ltd.

HUERTA, D. A. & RUIZ-SUÁREZ, J. C. 2004. Vibration-Induced Granular Segregation: A Phenomenon Driven by Three Mechanisms. *Physical Review Letters,* 92**,** 114301.

HUMLUM, O. 2017. Små regnbyger river ned fjellsider. *In:* VOGT, Y. (ed.). Apollon; Forskningsmagasinet: Universitetet i Oslo.

HUNGR, O. 2010. Dynamic analysis of landslides in three dimensions. Beta 2 ed. 4195 Almondel Rd., West Vancouever, B.C., Canada, V7V 3L6.

HUNGR, O., LEROUEIL, S. & PICARELLI, L. 2013. The Varnes classification of landslide types, an update. *Landslides,* 11**,** 167-194.

HØEG, K., LIED, K., KARLSRUD, K., GREGORY, T. & NORGES GEOTEKNISKE, I. 2014. *Skred : skredfare og sikringstiltak : praktiske erfaringer og teoretiske prinsipper,* Oslo, NGI Universitetsforl.

INTERNATIONAL ORGANIZATION FOR STANDARDIZATION 2002. ISO 14688-1: Geotechnical investigation and testing. *Identification and classification of soil.* International Organization for Standardization.

INTERNATIONAL SOCIETY FOR SOIL MECHANICS AND GEOTECHNICAL ENGINEERING. 2004. *Glossary of Risk Assessment Terms* [Online]. Available: http://140.112.12.21/issmge/2004Glossary_Draft1.pdf [Accessed 24. March 2017].

IVERSON, R. M. 1997. The physics of debris flows. *Reviews of Geophysics,* 35**,** 245-296.

IVERSON, R. M. 2005. Mechanical definition of debris flow. *Debris-flow Hazards and Related Phenomena.* Berlin, Heidelberg: Praxis Publishing Ltd.

JAEDICKE, C., SOLHEIM, A., BLIKRA, L. H., STALSBERG, K., SORTEBERG, A., AAHEIM, A., KRONHOLM, K., VIKHAMAR-SCHULER, D., ISAKSEN, K., SLETTEN, K., KRISTENSEN, K., BARSTAD, I., MELCHIORRE, C., HØYDAL, Ø. A. & MESTL, H. 2008. Spatial and temporal variations of Norwegian geohazards in a changing climate, the GeoExtreme Project. *Nat. Hazards Earth Syst. Sci.,* 8**,** 893-904.

JAKOB, M. 2005a. Debris-flow hazard analysis. *Debris-flow Hazards and Related Phenomena.* Berlin, Heidelberg: Praxis Publishing Ltd.

JAKOB, M. 2005b. A size classification for debris flows. *Engineering Geology,* 79**,** 151-161.

JAKOB, M. & HUNGR, O. 2005a. Classification and terminology. *Debris-flow Hazards and Related Phenomena.* Berlin, Heidelberg: Praxis Publishing Ltd.

JAKOB, M. & HUNGR, O. 2005b. *Debris-flow Hazards and Related Phenomena,* Berlin, Heidelberg, Praxis Publishing Ltd.

JOHANNES, S., IGNACIO, A.-C., ERWIN, F., VERENA, K., MARK, L., TOBIAS, P., STEPHAN, P., CURTIS, R., STEPHAN, S., BENJAMIN, S., JEAN-YVES, T., DANIEL JAMES, W., VOLKER, H., KEVIN, E., PAVEL, T. & ALBERT, C. 2012. Fiji: an open-source platform for biological-image analysis. *Nature Methods,* 9**,** 676.

KARTVERKET. 2016. *FKB - Felles kartdatabase* [Online]. Available: http://www.kartverket.no/data/kartdata/Vektorkart/FKB/ [Accessed 11.04 2017].

KARTVERKET. 2017. *Norgeskart.no* [Online]. Available: http://www.norgeskart.no/?_ga=2.102526273.150481016.1495702975-1433620982.1477641448#!?project=seeiendom&layers=1002,1014&zoom=9&lat=6930366.37&lon=56466.03 [Accessed 21. April 2017].

KLIMA 2050. 2017. *Klima 2050 - What we do* [Online]. Available: http://www.klima2050.no/what-we-do/ [Accessed 7. April 2017].

KRONHOLM, K., NES, S. & VIAK, A. 2015. Skredfarekartlegging i Ørsta kommune. Middelthunsgate 29 Postboks 5091 Majorstua 0301 OSLO: NVE.

KÖPPEN, W. & GEIGER, R. 1936. *Handbuch der Klimatologie : 1,* Berlin, Verlag von Gebryder Borntraeger.

LAMBECK, K., BOSCHI, E. & SABADINI, R. 1991. *Glacial isostasy, sea-level and mantle rheology,* Dordrecht, Kluwer.

LEE, C. & CHEN, H. 2003. A dynamic model for rainfall-induced landslides on natural slopes. 51**,** 269-288.

LEIBMAN, M., KHOMUTOV, A. & KIZYAKOV, A. 2014. Cryogenic Landslides in the Arctic Plains of Russia: Classification, Mechanisms, and Landforms. *In:* SASSA, K., CANUTI, P. & YIN, Y. (eds.) *Landslide Science for a Safer Geoenvironment: Volume 3: Targeted Landslides.* Cham: Springer International Publishing.

MAJOR, J. J. & IVERSON, R. M. 1999. Debris-flow deposition: Effects of pore-fluid pressure and friction concentrated at flow margins. *Bulletin of the Geological Society of America,* 111**,** 1424-1434.

MCDOUGALL, S. 2006. A new continuum dynamic model for the analysis of extremely rapid landslide motion across complex 3D terrain. The University of British Columbia.

MEGAHAN, W. F. 1983. Hydrologic effects of clearcutting and wildfire on steep granitic slopes in Idaho. *Water Resources Research,* 19**,** 811-819.

METEOROLOGISK INSTITUTT. 2017. *Köppens klimaklassifikasjon* [Online]. Available: https://metlex.met.no/wiki/K%C3%B6ppens_klimaklassifikasjon [Accessed 6. March 2017].

MEYER, N. K., DYRRDAL, A. V., FRAUENFELDER, R., ETZELMULLER, B. & NADIM, F. 2012. Hydrometeorological threshold conditions for debris flow initiation in Norway.

MILJØDIREKTORATET. 2016. *Hva er allemannsretten?* [Online]. Miljødirektoratet. Available: http://www.miljodirektoratet.no/no/Tema/Friluftsliv/Allemannsretten/Hva-er-allemannsretten/ [Accessed 16. february 2017].

MISSOURI STATE UNIVERSITY 2008. Standard Operating Procedure for: LS 13 320 Laser Diffraction Particle Size Analyzer Operation. Missouri State University.

NEEB, P.-R. 1992. *Byggeråstoffer : kartlegging, undersøkelse og bruk,* Trondheim, Tapir.

NGU. 2017a. *Berggrunnskart* [Online]. Available: http://geo.ngu.no/kart/berggrunn_mobil/ [Accessed 21. February 2017].

NGU. 2017b. *Løsmassekart* [Online]. Available: http://geo.ngu.no/kart/losmasse/ [Accessed 21. February 2017].

NICHOLS, G. 2009. *Sedimentology and stratigraphy,* Chichester, Wiley-Blackwell.

NOAA-USGS DEBRIS FLOW TASK FORCE. 2005. *NOAA-USGS Debris-Flow warning system--final report,* Reston, Va., U.S. Geological Survey.

NOREM, H. 2011. Veger og snøskred : håndbok om sikring mot snøskred : høringsutgave. Oslo: Vegdirektoratet.

NOREM, H., SANDERSEN, F. & VEGDIREKTORATET. TRAFIKKSIKKERHET, M.-O. T. 2012. Flom- og sørpeskred: Høringsutgave av veileder. *Debris flows and slush avalanches : draft version of manual.* Oslo: Statens vegvesen.

NORGE I BILDER. 2017. *Norge i bilder* [Online]. Available: https://www.norgeibilder.no/ [Accessed 24. February 2017].

NRK. 2013. *Trodde ikke dette kunne skje oss* [Online]. Available: https://www.nrk.no/mr/_-trodde-ikke-dette-kunne-skje-oss-1.11361407 [Accessed 27. April 2017].

NRK. 2015. *Årsetdalen ramma av skred igjen* [Online]. Available: https://www.nrk.no/mr/arsetdalen-ramma-av-skred-igjen-1.12676228 [Accessed 27. April 2017].

OLJE- OG ENERGIDEPARTEMENTET 2012. Hvordan leve med farene - om flom og skred. *In:* ENERGIDEPARTEMENTET, O.-O. (ed.). Postterminalen 5892 Bergen: Fagbokforlaget.

OLSEN, L., FREDIN, O. & OLESEN, O. 2013. *Quaternary geology of Norway,* Trondheim, Geological Survey of Norway.

OLSEN, M. H. H., AGATHE A., MYRABØ, S., VIRÉHN, P. & GLAD, P. A. 2015. Flom- og skredhendelser i Gudbrandsdalen. *In:* OLSEN, M. H. (ed.).

PESCAROLI, G. A., D 2015. A definition of cascading disasters and cascading effects: Going beyond the "toppling dominos" metaphor. *Planet@Risk.* Davos: Global Risk Forum GRF Davos.

PIERSON, C. T. 2004. U.S. GEOLOGICAL SURVEY — REDUCING RISK FROM VOLCANO HAZARDS Distinguishing between Debris Flows and Floods from Field Evidence in Small Watersheds. U.S. Geological Survey Fact Sheet.

PIERSON, T. C. 1995. Flow characteristics of large eruption-triggered debris flows at snow-clad volcanoes: constraints for debris-flow models. *Journal of Volcanology and Geothermal Research,* 66**,** 283-294.

PIERSON, T. C. 2005. Hyperconcentrated flow - transitional process between water flow and debris flow. *Debris-flow Hazards and Related Phenomena.* Berlin, Heidelberg: Praxis Publishing Ltd.

PROCHASKA, A. B., SANTI, P. M., HIGGINS, J. D. & CANNON, S. H. 2008. A study of methods to estimate debris flow velocity. *Landslides,* 5**,** 431-444.

REVELLINO, P., HUNGR, O., GUADAGNO, F. M. & EVANS, S. G. 2004. Velocity and runout simulation of destructive debris flows and debris avalanches in pyroclastic deposits, Campania region, Italy. *Environmental Geology,* 45**,** 295-311.

REYNOLDS, J. M. 2011. *An introduction to applied and environmental geophysics,* Chichester, Wiley-Blackwell.

SANDERSEN, F., BAKKEHOI, S., HESTNES, E. & LIED, K. 1996. The influence of meteorological factors on the initiation of debris flows, rockfalls, rockslides and rockmass.

SANDMEIER, K.-J. 2017. *Sandmeier geophysical research* [Online]. Available: http://www.sandmeier-geo.de/index.html [Accessed 6. February 2017].

SANDØY, G., RUBENSDOTTER, L. & DEVOLI, G. 2017. Trekantformede jordskred – Studie av fem skredhendelser i Norge. Available: http://www.ngu.no/upload/Publikasjoner/Rapporter/2017/2017_017.pdf.

SAVAGE, W. B., R. 2005. Instability of steep slopes. *Debris-flow Hazards and Related Phenomena.* Berlin, Heidelberg: Praxis Publishing Ltd.

SCHANCHE, S. 2014. Sikkerhet mot skred i bratt terreng *In:* SCHANCHE, S. (ed.). Oslo: Norges vassdrags- og energidirektorat

SCHEIDL, C., RICKENMANN, D. & MCARDELL, B. W. 2013. Runout Prediction of Debris Flows and Similar Mass Movements. *In:* MARGOTTINI, C., CANUTI, P. & SASSA, K. (eds.) *Landslide Science and Practice: Volume 3: Spatial Analysis and Modelling.* Berlin, Heidelberg: Springer Berlin Heidelberg.

SENORGE. 2017. *senorge.no* [Online]. Available: http://www.senorge.no/index.html?p=klima [Accessed 16. March 2017].

SIDLE, R. C. & OCHIAI, H. 2006. Landslides : processes, prediction, and land use. *Landslides.* Washington, DC: American Geophysical Union.

SIEDLER, C. E. 2013. Samfunnsøkonomiske kostnader av Gudbrandsdalsflommen 2013. NVE.

SKREDNETT. 2016. *Skrednett* [Online]. Available: https://www.nve.no/flaum-og-skred/skrednett/ [Accessed 27. May 2016].

SKREDNETT. 2017. *Skrednett* [Online]. Available: https://www.nve.no/flaum-og-skred/skrednett/ [Accessed 19. May 2017].

SLETTAN, O. V. & SMITS, J. 2013. *Full storm : naturkatastrofer og ekstremvær i Norge,* Oslo, Gyldendal.

SORTEBERG, A. & KVAMSTØ, N. G. 2008. Hvor mye vil nedbøren øke i et varmere klima? *Klima***,** 36-38.

STATENS VEGVESEN 2014. Laboratorieundersøkelser : [håndbok R210]. Oslo: Statens vegvesen.

STATENS VEGVESEN REGION, Ø. 2012. Rapport om skadeflommen i pinsehelga 2011 : Hedmark og Oppland. Lillehammer: Statens vegvesen. Region øst.

STINI, J. 1910. *Die muren; versuch einer monographie mit besonderer berücksichtigung der verhältnisse in den Tiroler Alpen,* Innsbruck,, Verlag der Wagner'schen universitäts-buchhandlung.

SUNNMØRSPOSTEN. 2013. *40 evakuert etter jordras* [Online]. Available: http://www.smp.no/nyheter/soere/article8636817.ece [Accessed 8. March 2017].

TAKAHASHI, T. 2007. *Debris Flow: Mechanics, Prediction and Countermeasures*, Taylor & Francis.

THE WORLD BANK 2010. *Natural Hazards, UnNatural Disasters : The Economics of Effective Prevention,* Washington, World Bank Publications.

TOLLAN, A. 1977. *Vann : en naturressurs,* Oslo, Universitetsforlaget.

VANDINE, D. F. 1996. *Debris flow control structures for forest engineering,* 31 Bastion Square Victoria, BC v8W3E7, Ministry of forests research program.

VARNES, D. J. 1974. Slope movement types and processes. *TRB special report*.

VARSOM. 2017. *Varsom.no* [Online]. Available: http://www.varsom.no/en/flood-and-landslide-warning-service/ [Accessed].

W. R. PARKER, D. J. J. K. 1984. Transfer processes in cohesive sediment systems.

WARD, S. 2001. Landslide tsunami. *Journal of Geophysical Research. B,* 106**,** 11201-11215.

WIECZOREK, G. F. & GLADE, T. 2005. Climatic factors influencing occurence of debris flow. *Debris-flow Hazards and Related Phenomena.* Berlin, Heidelberg: Praxis Publishing Ltd.

ZHANG, Y. 2015. *Stability and Run-out Analysis of Earthquake-induced Landslides*.

ZIEMER, R. R. The role of vegetation in the stability of forested slopes. Proceedings of the International Union of Forestry Research Organizations, XVII World Congress, 1981 Kyotom Japan. 297-308.

Appendix 1: Field work form and field work form guide

General	
Surveyor:	**Date:**
Institution:	**E-mail:**
Name of the locality:	**County/municipality:**
Coordinates (UTM-zone:): **E** **N**	**Date of event(s):**
Type of transport zone	☐ **Channelized**	☐ **Open slope**
Slope angle (β):	
Slope aspect (degrees):	
Elevation difference between release area and depositional area (H):	
Total runout length (L):	

Landslide material:
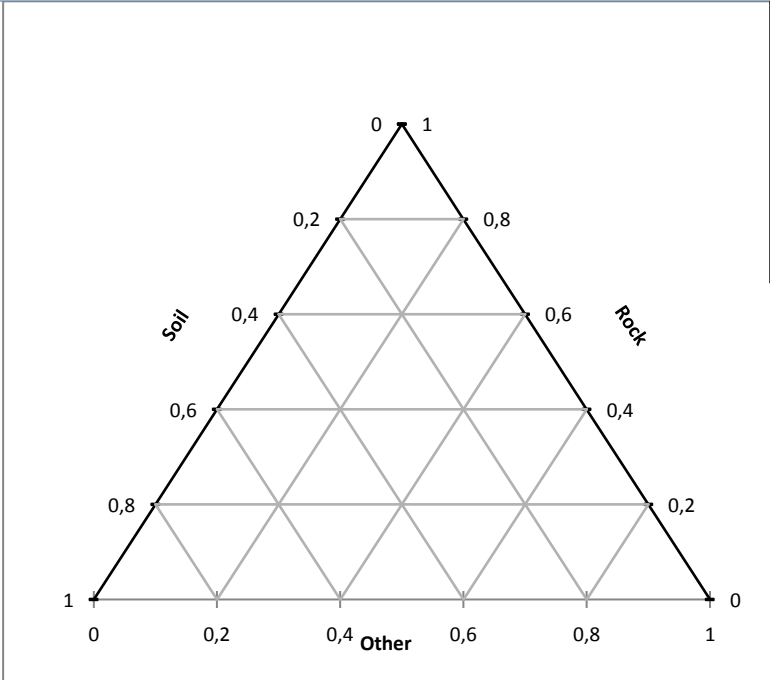
Soil: Inorganic clasts/particles < 60 mm
Rock: Inorganic clasts > 60 mm
Other: Not covered by the definitions above (such as vegetation).

Comment landslide material:

Vegetation:
Release area:
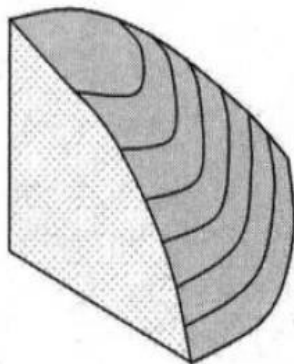- ☐ **(Bushes and trees)**
- ☐ **(Grass, moss and heather)**

Transport zone:
- ☐ **(Bushes and trees)**
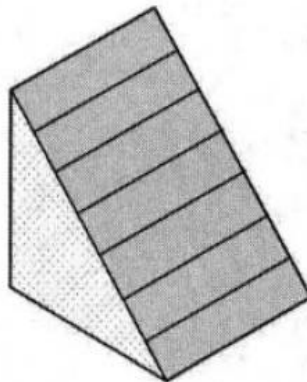- ☐ **(Grass, moss and heather)**

Depositional area:
- ☐ **(Bushes and trees)**
- ☐ **(Grass, moss and heather)**

Divergent ☐   Straight ☐   Convergent ☐
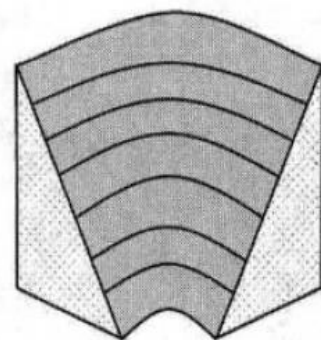
Exposed bedrock (optionally m.a.sl.):
- ☐ **Release area**
- ☐ **Transport zone**
- ☐ **Depositional area**

148

Preliminary dimensions of release area (area and average depth):	
Preliminary dimensions of depositional area (area and average height):	
Most probable triggering factor: ☐ **Precipitation/Runoff** ☐ **Snow avalanche, rockfall or other landslides.** ☐ **Human activity** ☐ **Other**	
Comment triggering factor:	

Sketch of the landslide (sketch 1):

Release area

Largest slope angle (degrees):	**Shape:**
Length (m):	☐ Stream (erosion)
Width (m):	☐ Well defined upper scarp
Depth (m):	☐ Sliding plane
Volume (m³):	☐ Multiple release areas
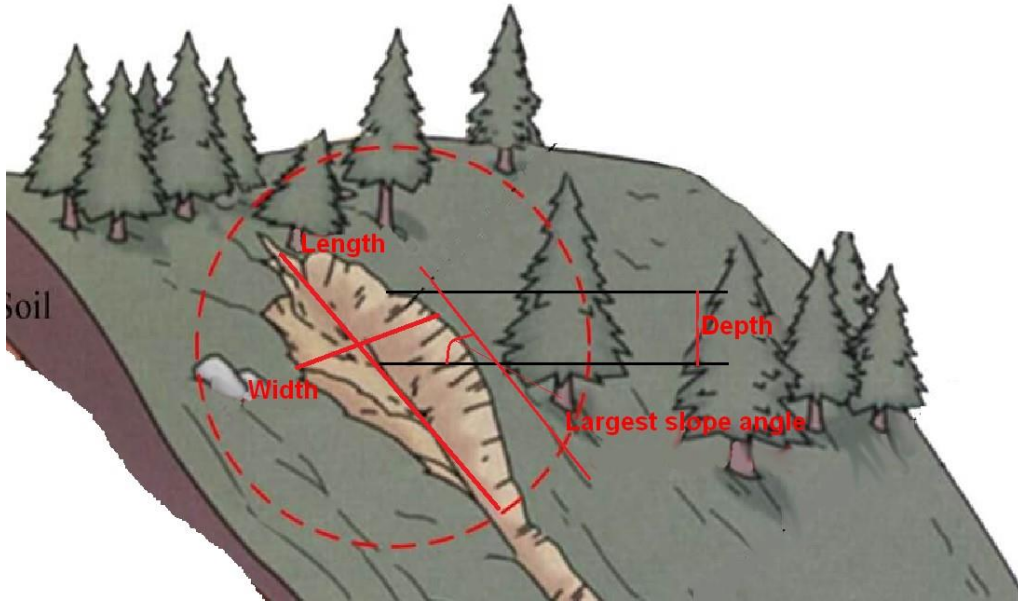
Soil cover in the release area (assign number from highest to lowest if multiple present):

- ☐ Till
- ☐ Landslide material
- ☐ Residual soil
- ☐ Glaciofluvial
- ☐ Marine
- ☐ Fluvial

Strike and dip-orientation of the bedrock (if observed):

Indicators of local pore water pressure:

- ☐ Dry
- ☐ Moist
- ☐ Running water
- ☐ Spurt of water

Comment local pore water pressure:

Comment release area:

Transport zone					
Number of paths:					
Through what kind of material does the transport zone run:					
☐ **Till**					
☐ **Landslide material**					
☐ **Residual soil**					
☐ **Glaciofluvial**					
☐ **Marine**					
☐ **Fluvial**					
Longitudinal segments of the transport zone	**1**	**2**	**3**	**4**	**5**
Length (m):					
Elevation difference (m):					
Width (m):					
Depth (m):					
Height of levees (m):					
Slope angle (degrees):					
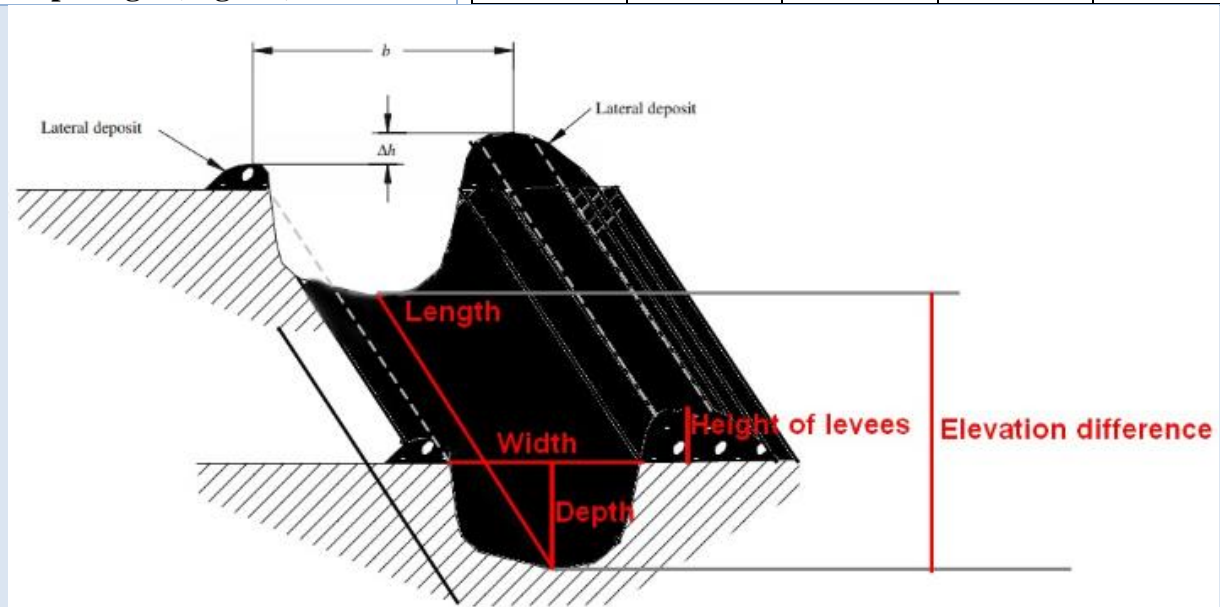
Mechanism of erosion (undercutting and bed destabilization in %):

Parameters for velocity measured in a bend (UTM coordinates   E   N):
Δh:
b:
r_c (r_c is the radii in an imaginary circle fitting the bend. Not measured in the field):

Comment transport zone:

Depositional area

Description of the surface(s) over which the flowing material is deposited:

Length (m):	**Rough grain size distribution (%):** **Boulder (> 200 mm):** **Cobble (200-60 mm):**
Max depth (m): **Avgerage depth (m):**	**Gravel to sand (60-0.063 mm):** **Silt to clay (< 0.063 mm):** **Organic:**

Max width (m):
 	
Average width (m):
	Grading longidutinally:
	  ☐ **Normal**
	  ☐ **Reverse**
	  ☐ **None**

Area (m²): **Volume (m³):**	
Slope angle at the start of the depositional area (degrees):	
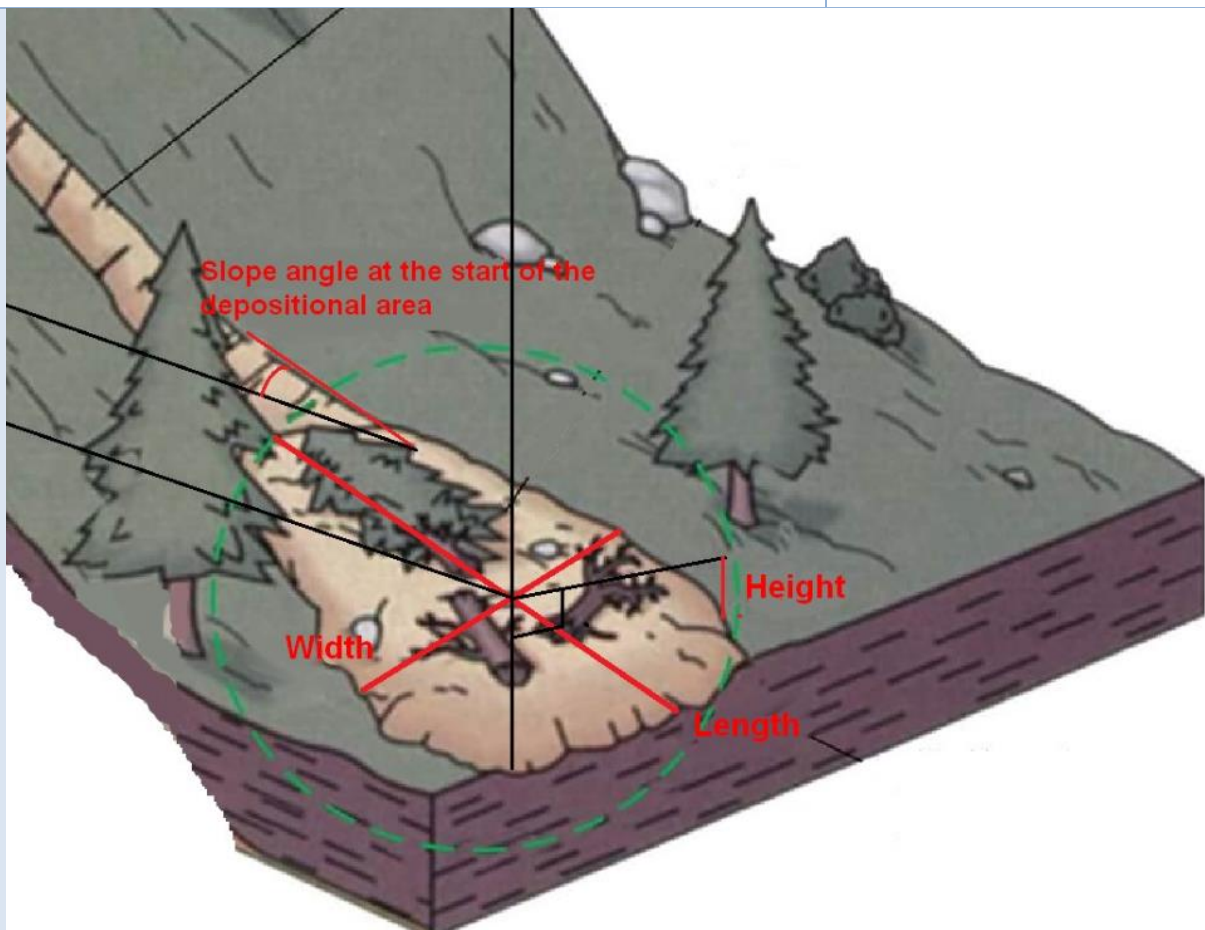
Deposition on obstacle (UTM coordinates   E   N): h:

Stopping mechanism (rank by number if numerous, 1 = most important):
- ☐ **Decreased slope angle**
- ☐ **Impediments**
- ☐ **Spreading/decreased channelization**
- ☐ **Other**

Comment stopping mechanism:

Indications of multiple surges:
- ☐ **Channels on the depositional lobe**
- ☐ **Multiple vertical depositional sequences**
- ☐ **Multiple depositional lobes**
- ☐ **Other:**

Comment depositional area:

Appendices
Samples and measurements should be marked on map, sketches or with coordinates.

☐ Pictures

☐ Map

☐ Soils samples

☐ Profiles

☐ GPS measurements

☐ Geophysical data
Comments geophysical data:

☐ Hydrologic measurements
Comment hydrologic measurements:

☐ Other
Comment other:

This field work form has been developed in order to make a standardized method for characterizing and describing shallow landslides. The investigations should be relatively easy, while providing sufficient data for runout simulations and give better understanding of such events, in addition to do statistical analysis on parameters gathered at several sites. This document contains a description of each section of the field work form, some methods and preparations. The form is divided into a general section, containing the most basic parameters, and three sub-sections, one for each part of the land slide (release area, transport zone and depositional area).

Additional data can be appended depending on the level of detail of the investigations. As such, the form has three levels of detail: 1) A basic level, containing only the general section. 2) The complete field work form, with all three sections. 3) The complete field work form, with additional data appended.

Preparations:

Some work should be done prior to the field survey, to improve accuracy and efficiency of the field investigations. Bedrock and sediment maps (available at ngu.no/en/topic/applications) should be examined and used in the field, and inventory maps (available at atlas.nve.no) should be investigated. If detailed orthophotos of the site are available, one should attempt to measure as many of the parameters as possible and map the site before field investigations, and verify or correct these in the field. High resolution maps (> 1:5000) should be brought for the field investigations. In addition, the following equipment is useful:

Shovel
GPS
Compass (preferably with clinometer)
Measuring tape (or laser)
Meterstick
Camera
Notebook and pencil
Container or bag for soil samples

General:

Date of the events are important in order to do statistical analysis on regional patterns, and determine the weather conditions on the date of the event. If multiple known events, all should be noted.
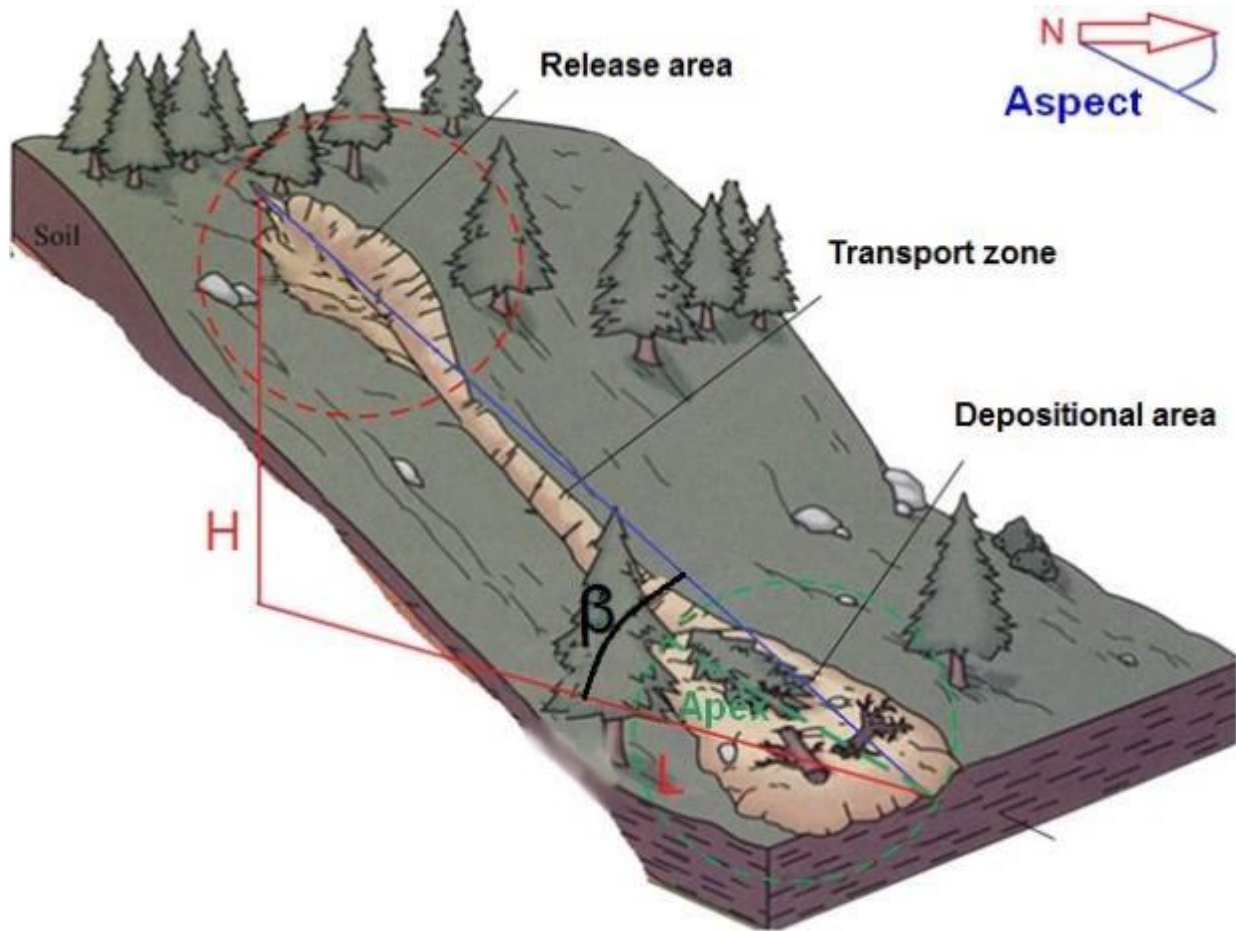
Figure 67: Overview of the landslide and the different zones.

Coordinates should be written in UTM format, and a description of the point noted. The aspect of the slope is the direction, in degrees, towards which the slope faces. The slope angle (β) is the angle between the upper boundary of the release area and the lower boundary of the depositional area, and an imaginary horizontal plane. The elevation difference (H) is measured between the two aforementioned points, and the runout length (L) is the horizontal distance between the two points. The slope angle can easily be calculated after a short reconnaissance with GPS, map study or by use of a clinometer.

The classification of the landslide material is meant to be a quick estimate of the distribution of soil, rock and other materials, where soil is defined as inorganic grains smaller than 60 mm, rock as clasts larger than 60 mm. If the depositional lobe displays different materials, this can be marked with unique symbols on the triangle plot, and explained in the comment field. For vegetation, the type assumed to cover each area prior to the event is checked off.
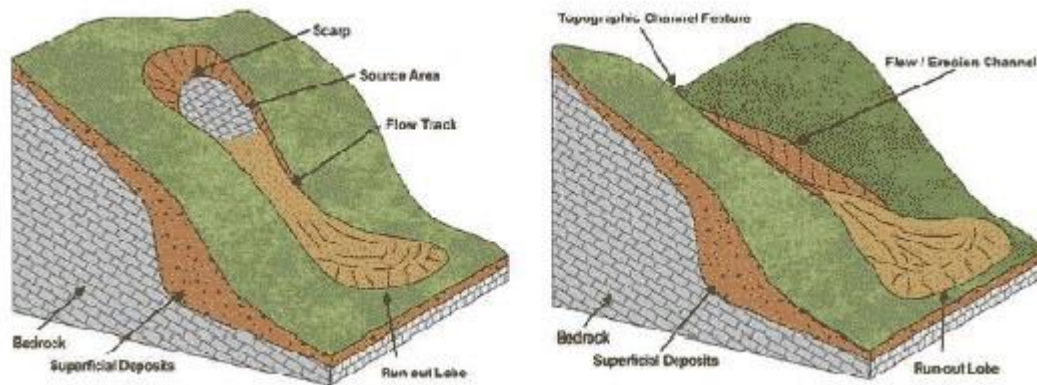
Figure 68: Schematic overview of an open slope event (left) and a channelized event (right) (Sassa et al., 2014).

In establishing whether the terrain geometry in and around the release area is convergent, divergent or straight (in accordance with the figure in the field work form), a topographic map will be useful. If there is exposed bedrock, the box indicating which part of the landslide area bedrock is observed should be checked, and if possible the elevation at which the observations were made should be noted. If more accurate measurements are not made, the dimensions can be estimated from aerial photography, but depth should not be reported unless other information is available to confirm it.

Sketch 1 should be a rough overview, primarily used to organize samples, data and photographies. Alternatively, high resolution maps can be used.

Release area:

Schematically, the length of the release area is defined as the longest axis along the flow/slide direction and the width perpendicular to this. As irregular shapes do occur, this might not always be the ideal axis measured, and area can be reported instead. The highest degree of accuracy is achieved with a GPS track, or high resolution terrain models, of the release area. The depth should be measured at several points to find an average. If a well defined release area is not visible, this field is left blank. The shape of the release area should be noted, and if there are multiple release areas, multiple versions of this section should be used. The soil cover in the release area is categorized as till, residual soil, glaciofluvial deposits, marine deposits or fluvial deposits. If multiple layers are present this can be noted with a number next to the soil cover type, and explained in the comment field. If bedrock is exposed in the release area, strike and dip should be measured, and any indicators of local pore water pressure should be noted.

Transport zone:

The soil in which the transport zone is eroded, or flowing/sliding over, is defined the same way as in the release area. In addition, the length, elevation difference between upper and lower part, width and depth of channel or transport zone are measured. Levees are measured if present. If there are significant differences along the transport zone, it can be useful to divide the transport zone into segments. Slope angle for each zone can be calculated later. If there are numerous paths or channels, this should be noted, and several versions of this section should be used, one for each path/channel. Whether undercutting of the banks or bed

160

destabilization is the dominating erosion and entrainment mechanism should be determined. A rough estimate of the importance of each should be made.

In order to calculate velocities, the height difference between the inner and outer deposits on a channel bend can be used, in accordance with the forced vortex equation: $U=\sqrt{((g\Delta h r_c)/b)}$, where g is the gravitational acceleration, Δh the height difference between the inner and outer deposits, r_c is the radius of an imaginary circle fitting the bend and b is the channel width.
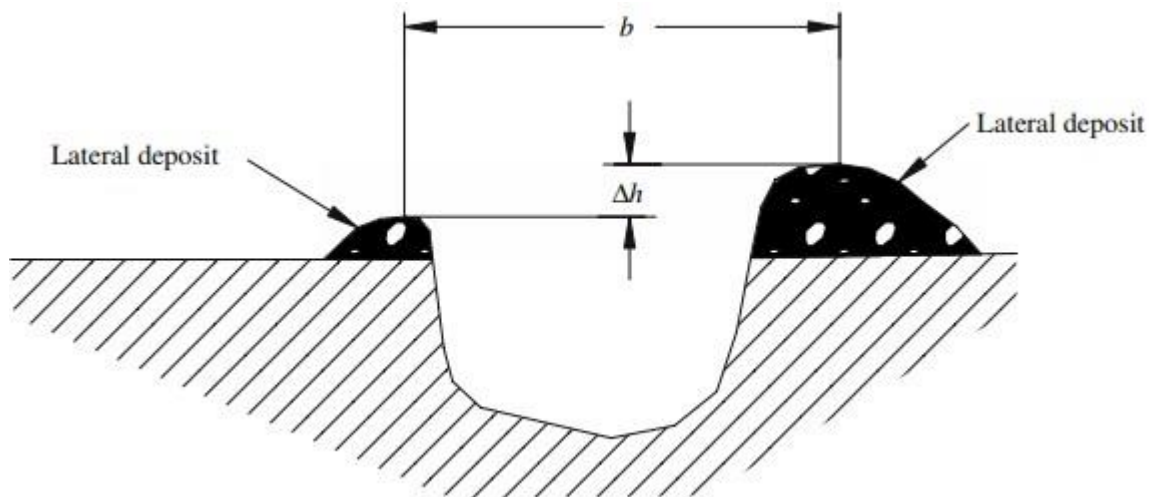

Figure 69: Parameters used in velocity estimations in a bend (Prochaska et al., 2008).

Depositional area:

The depositional area is defined from the point where deposition is, and continues to be, larger than erosion, velocity decreases and/or where a well-defined depositional lobe is visible. The lower boundary is set at a clear front, or obstacle limiting the deposits (such as rivers or ridges). One should therefore be aware that finer phases of the landslide material might not be visible or included in the final volume estimations. Length and width are measured similarly to at the release area, and deposit height should be measured in several places to allow for a representative average. The axis along which length and width are measured should be noted, and if the shape is particularly irregular, estimated area can be reported instead. As the intention of these measurements is to estimate the total volume of the final deposits, the best accuracy can be achieved by logging a GPS track around, and profiles over, the depositional area.

A rough grain size distribution is reported, differentiating boulder (> 200 mm), cobble (200-60 mm), gravel to sand (60-0.063 mm), silt and clay (< 0.063 mm) and organic material. Longitudinal grading is defined as normal (coarse to fine), reverse (fine to coarse) or none. The sample site should be photographed, and noted on sketch, map or with a GPS grid.

If masses are deposited on impediments, the height difference between the highest deposits and the lowest should be measured in order to do velocity estimations. The method uses the energy balance equation: $U = \sqrt{2gh}$, where g is the gravitational acceleration, and h the aforementioned height difference.
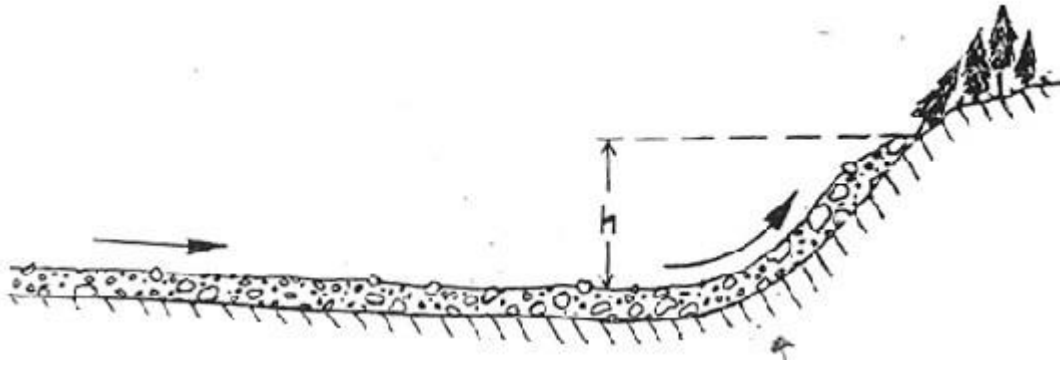
Figure 70: Parameter used in velocity estimations from deposition on impediments.

Important stopping mechanisms should be checked off and if multiple are likely, a number should be assigned in accordance with assumed importance (1 = most important). If indications of multiple surges are present this is noted as well.

PROCHASKA, A. B., SANTI, P. M., HIGGINS, J. D. & CANNON, S. H. 2008. A study of methods to estimate debris flow velocity. *Landslides,* 5**,** 431-444.
SASSA, K., YIN, Y. & CANUTI, P. 2014. *Landslide Science for a Safer Geoenvironment : Volume 3: Targeted Landslides,* Cham, Springer International Publishing.

162